

NASA
Technical
Paper
3365

November 1993

An Experimental Investigation of a Mach 3.0 High-Speed Civil Transport at Supersonic Speeds

Gloria Hernandez,
Peter F. Covell, and
Marvin E. McGraw, Jr.

N94-24311

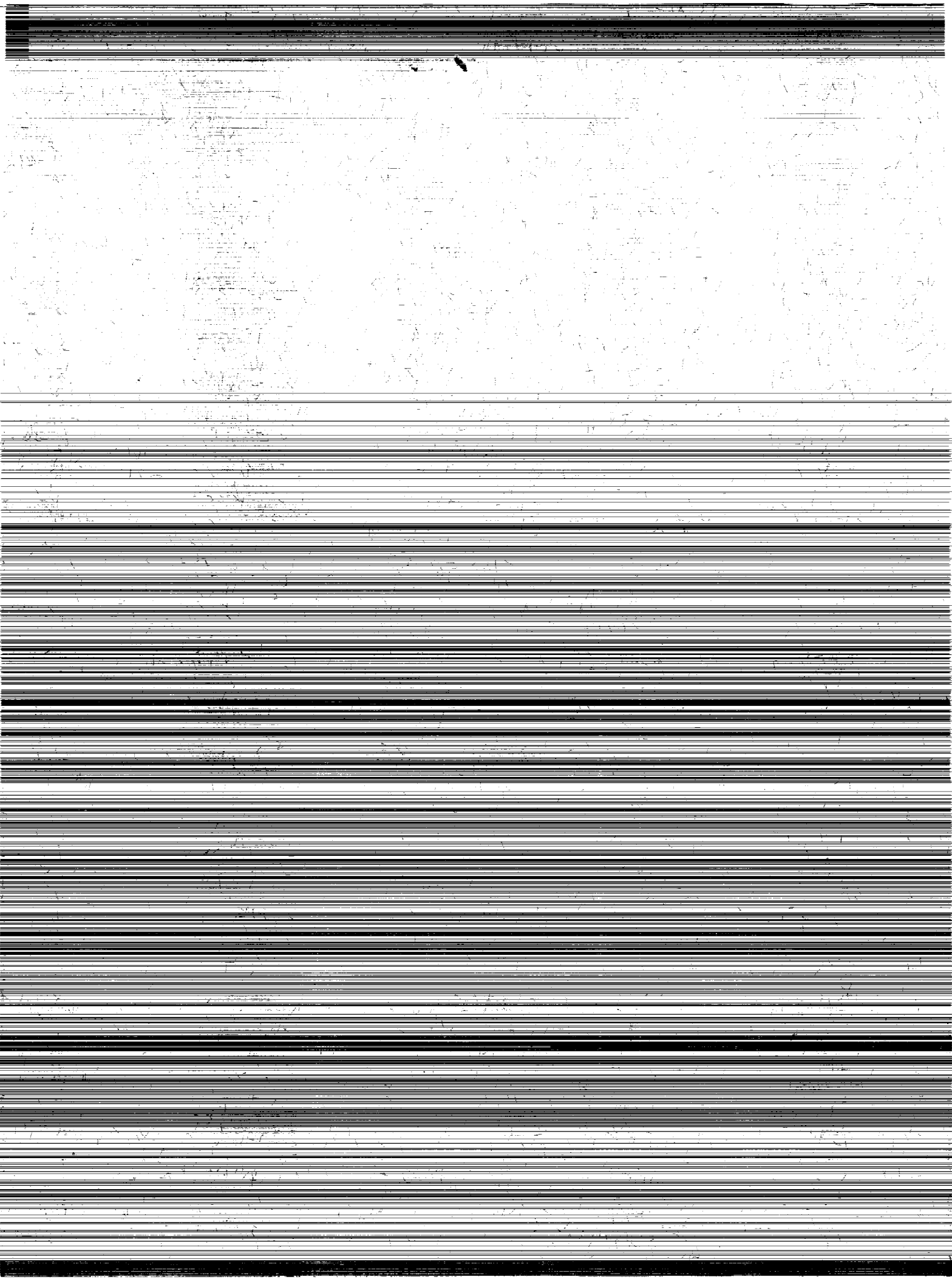
Unclass

H1/02 0204173

(NASA-TP-3365) AN EXPERIMENTAL
INVESTIGATION OF A MACH 3.0
HIGH-SPEED CIVIL TRANSPORT AT
SUPERSONIC SPEEDS (NASA) 94 p

IN-02
MF INCLOSED
204173
P-94

NASA



**NASA
Technical
Paper
3365**

1993

**An Experimental Investigation
of a Mach 3.0 High-Speed Civil
Transport at Supersonic Speeds**

Gloria Hernandez
and Peter F. Covell
*Langley Research Center
Hampton, Virginia*

Marvin E. McGraw, Jr.
*Lockheed Engineering & Sciences Company
Hampton, Virginia*



National Aeronautics and
Space Administration
Office of Management
Scientific and Technical
Information Program

Contents

Summary	1
Introduction	1
Symbols	1
HSCT Concept Description	2
Model Description and Test Techniques	3
Results and Discussion	3
Extrapolation to Full Scale	5
Concluding Remarks	6
Tables	7
Figures	12
Appendix A	42
Appendix B	48
Appendix C	55
Appendix D	60
Appendix E	89
References	90

Summary

An experimental study has been conducted to determine the aerodynamic characteristics of a proposed high-speed civil transport. This configuration was designed to cruise at Mach 3.0 and sized to carry 250 passengers for 6500 n.mi. The configuration consists of a highly blended wing body and features a blunt parabolic nose planform, a highly swept inboard wing panel, a moderately swept outboard wing panel, and a curved wingtip. Wind tunnel tests were conducted in the Langley Unitary Plan Wind Tunnel on a 0.0098-scale model.

Force, moment, and pressure data were obtained for Mach numbers ranging from 1.6 to 3.6 and at angles of attack ranging from -4° to 10° . Extensive flow visualization studies (vapor screen and oil flow) were obtained in the experimental program. Both linear and advanced computational fluid dynamics (CFD) theoretical comparisons are shown to assess the ability to predict forces, moments, and pressures on configurations of this type. In addition, an extrapolation of the wind tunnel data, based on empirical principles, to full-scale conditions is compared with the theoretical aerodynamic predictions.

Experimental results of the investigation showed that the maximum values of lift-to-drag ratio for the configuration varied from about 7 at the lower Mach numbers to about 6 at the higher Mach numbers. An unstable break in pitching moment began at a lift coefficient of approximately 0.1 at Mach 1.6 and occurred at a decreasing lift coefficient with increasing Mach number. Typical effects occurred with the addition of nacelles, which include an increase in lift, an increase in drag, and a decrease in lift-to-drag ratio.

Linear theory accurately predicted the drag polar characteristics and the drag increment resulting from the addition of nacelles; however, the magnitudes are offset throughout the lift and Mach number range examined. The stability of the configuration was not accurately predicted with the first-order methods. Euler and Navier-Stokes results, shown only for the cruise condition, showed very good agreement with the experimental data for lift, drag, and pitching moment (Euler only).

Preliminary aerodynamic predictions were optimistic for the full-scale configuration. Extrapolating wind tunnel data to full-scale conditions showed linear theory underpredicted the drag due to lift. Applying a recently published empirical method to adjust the linear theory prediction resulted in an excellent agreement with the wind tunnel results,

particularly at and below the design cruise lift coefficient.

Introduction

The supersonic aerodynamic characteristics of commercial supersonic transport (SST) concepts have been studied by NASA since the early 1960's. Several concepts were studied during the focused SST research program that ran from 1960 to 1971. Some of these concepts are documented in references 1-4. From 1971 to 1981 NASA concentrated on solving identified problems of supersonic cruise flight with the support of the U.S. aerospace industry (refs. 5 and 6). In 1987 a study by the Office of Science and Technology Policy (OSTP), Executive Office of the President (ref. 7), identified the technology developments necessary to support a long-range supersonic transport as one of three high-payoff national goals. It was recommended that the U.S. aerospace industry and NASA determine the most attractive technical concepts and necessary technology developments for future long-range high-speed civil transports (HSCT's).

In response to the OSTP recommendations, NASA has conducted technology integration studies and experimental validation testing focused on investigating long-range HSCT economic feasibility and technology requirements. The first phase of the current HSCT study program involved an examination of the factors influencing the choice of design Mach number and range. Analytical design studies conducted by NASA Langley Research Center have defined a highly blended Mach 3.0 cruise configuration sized to carry 250 passengers for 6500 n.mi. These studies employed the linear potential flow theory for the preliminary design and analysis to define the basic aerodynamic concept (ref. 8).

The primary objectives of the present study were to experimentally determine the basic supersonic aerodynamic characteristics of the HSCT configuration described in reference 8 as well as to investigate nacelle effects and to assess theoretical prediction methods. The experimental wind tunnel investigations were conducted in both test sections of the Langley Unitary Plan Wind Tunnel (UPWT).

Symbols

A_{nb}	nacelle base area
A_{wi}	nacelle internal wetted area
C_A	axial-force coefficient, $\frac{\text{Axial force}}{qS}$
C_D	drag coefficient, $\frac{\text{Drag}}{qS}$
$C_{D,c}$	chamber drag coefficient

$C_{D,i}$	nacelle internal drag coefficient, $\frac{\text{Internal drag}}{qS}$
$C_{D,\min}$	minimum drag coefficient
$C_{D,nb}$	nacelle base drag coefficient
C_f	compressible skin friction coefficient
C_{fi}	incompressible skin friction coefficient
C_f/C_{fi}	compressible flow factor
C_L	lift coefficient, $\frac{\text{Lift}}{qS}$
C_m	pitching-moment coefficient, $\frac{\text{Pitching moment}}{qS\bar{c}}$
$C_{m,0}$	pitching-moment coefficient at $C_L = 0$
C_N	normal-force coefficient, $\frac{\text{Normal force}}{qS}$
C_p	pressure coefficient (cp in appendix E)
$C_{p,nb}$	nacelle base pressure coefficient
\bar{c}	wing reference chord, 15.66 in.
g	acceleration due to gravity
L/D	lift-to-drag ratio
M	free-stream Mach number
m/m_∞	theoretical mass flow ratio
q	free-stream dynamic pressure, lb/ft ²
R	Reynolds number, per ft
S	wing reference area, 1.235 ft ²
S_i	inlet capture area, 0.6355 in ²
x	longitudinal distance from nose of model, in.
x_{le}	longitudinal leading-edge distance from nose, in.
x_{te}	longitudinal trailing-edge distance from nose, in.
y	spanwise distance from centerline, in.
α	angle of attack, deg
$\Delta C_D/\Delta C_L^2$	drag-due-to-lift factor
$\Delta C_L/\Delta \alpha$	lift-curve slope at $\alpha = 0$

$\Delta C_m/\Delta C_L$ longitudinal stability level at
 $C_L = 0$

ε duct angularity, 0.9°

η dimensionless semispan location,
(eta in appendix E)

HSCT Concept Description

The configuration originated from a Mach 3.0 cruise transport conceptual study conducted by NASA (ref. 8). As shown in figure 1, the configuration employs a blended wing-body, a blunt parabolic nose planform, a highly swept inboard wing panel, and a moderately swept outboard wing panel with curved wingtips. The planform was selected to minimize induced drag and wave drag due to lift while maintaining adequate low-speed performance characteristics. The compound-leading-edge planform was designed to minimize the aerodynamic center shift from takeoff to supersonic cruise speeds, and the lifting forewing can provide large favorable flap-trimming pitching moments. Nose planform blunting was employed to reduce maximum sonic boom overpressure and to produce high initial upwash in which the remainder of the wing might fly for improved drag due to lift.

The inboard wing panel has a leading-edge sweep of 79°, which produces a subsonic normal Mach number at the Mach 3.0 cruise condition. Because of the subsonic leading-edge normal Mach number, relatively blunt leading edges were possible without a substantial zero-lift wave drag penalty. A subsonic leading edge and leading-edge bluntness result in an insensitivity of leading-edge camber to supersonic cruise speed and of airfoil section performance to wing camber. These two features allow for a fixed wing geometry without leading-edge devices, which in turn provides for a simpler and lighter inboard wing panel.

The outboard wing panel is swept 53° with curved wingtips. At low speeds and high angles of attack, flow separation on a straight wingtip, leading to a stalled flow over the outboard wing, is common and tends to produce a severe pitch-up. However, this problem is relieved through controlled vortex separation by curving the wingtip planform (ref. 9). Other investigators have found (refs. 10 and 11) that wings with curved tips also have substantially better induced drag characteristics. High-lift devices, as incorporated into the conceptual design, were not modeled for this test, since these devices were designed for performance enhancement at subsonic speeds. Table I contains an analytic description of

the wing planform geometry. Coordinates for the wing airfoil sections can be found in reference 12.

The original concept employed six engines mounted in two nacelles on the wing lower surface adjacent to the fuselage. The nozzles were set at a 5° downward deflection so that the gross thrust vector develops not only a lift vector component but some induced circulation on the wing upper surface as well. Subsequent unpublished analysis indicated that four engines mounted in two nacelles on the wing lower surface would provide for a more economically viable aircraft; thus, the test nacelles were sized for two engines per side and modified to provide constant-area flow-through with no turning from inlet to nozzle exit. The nacelle exterior mold lines characteristic of a 5° downward deflection located close to the wing trailing edge were retained.

Model Description and Test Techniques

The wind tunnel model is a 0.0098-scale model of the conceptual design (fig. 2). The afterbody was truncated in order to permit a standard balance/sting support arrangement. The model was fitted with 59 pressure orifices, arranged in 4 rows spanwise and 2 rows chordwise. The orifices are located on the upper and lower wing surfaces as shown in figure 3 and defined in table II. A photograph of the model installed in the Langley UPWT is shown in figure 4. The basic dimensions for the nacelle geometry are included in table I.

The tests were conducted in the high Mach number and low Mach number test sections of the UPWT, a variable-pressure, continuous-flow facility (ref. 13). The Mach numbers ranged from 1.6 to 3.6 (Mach 1.6 and 2.0 were conducted in test section I; Mach 2.4, 2.8, 3.0, 3.2, and 3.6 were conducted in test section II) through an angle-of-attack range from -4° to 10°. A unit Reynolds number of 2×10^6 per ft and a stagnation temperature of 125° F were held constant throughout the test. The tunnel dew point was held sufficiently low to prevent any significant condensation.

Transition strips of carborundum grit were located 0.4 in. aft, measured streamwise, of the leading edge of all wing surfaces. Transition strips were also located on the outer and inner surfaces aft of the engine nacelle leading edge. One size grit was selected for all the Mach numbers tested in test section I (no. 60) and another size for test section II (no. 45). The grit size was selected to approximately match the height of the laminar boundary layer at 0.4 in. aft of the leading edge at Mach 2.0 and Mach 3.6. The size and location were selected to ensure fully turbulent

boundary-layer flow over most of the model at all test conditions according to the methods discussed in references 14-16.

An internally mounted, six-component, strain-gauge balance was used to measure model forces and moments. Surface pressure measurements were obtained using electronically scanned pressure (ESP) transducers, referenced to a vacuum. The aerodynamic coefficient accuracy based on uncertainties of the key parameters used to determine the coefficients and the approximate overall accuracy of the ESP system including calibration accuracy are presented in table III.

Corrections to the model angles of attack were made for both tunnel airflow angularity and deflection of the model and sting support due to the aerodynamic load. Chamber-pressure measurements obtained from four orifices located within the fuselage cavity were used to adjust the drag coefficient to a condition of free-stream static pressure at the model base. Two of the orifices were located immediately behind the balance on opposite sides of the sting and two were located approximately 1 in. from the base of the model, again on opposite sides of the sting. The correction used was based on the average reading from the four orifices. Estimates of nacelle internal drag and nacelle base drag were subtracted from the total drag. The nacelle internal drag was calculated using the following equation:

$$C_{D,i} = C_{fi}(C_f/C_{fi})(A_{wi}/S) \cos(\alpha + \epsilon) + 2(S_i/S)(m/m_\infty) \sin^2(\alpha + \epsilon)$$

where the first term on the right is the internal skin-friction drag calculated by using the Sommer-Short T' method from reference 17 and the second term is an estimate of the drag component produced as the flow ahead of the nacelle is turned through the angles α and ϵ as used in reference 18. A sketch illustrating the angle ϵ is included in table I. The nacelle base pressure was measured and used to calculate the nacelle base drag ($C_{D,nb} = -1(C_{p,nb})(A_{nb}/S)$). Typical drag corrections are plotted in figure 5. The complete correction list is presented in table IV and appendix A.

Results and Discussion

The linear method (ref. 19) utilized here is based on standard supersonic potential flow theory (with attainable leading-edge thrust included) for the inviscid lift-dependent characteristics, far field wave drag (supersonic area rule) for inviscid zero-lift wave drag, and the Sommer-Short T' reference temperature method (ref. 17) for skin friction

drag. The present linear theory does not accept non-circular nacelles; therefore, circular nacelles with an equivalent area distribution as the nacelles on the conceptual model were modeled to obtain the linear theory results.

Experimental data and linear theory estimates for the longitudinal aerodynamic characteristics are shown graphically in figures 6–12 for the range of Mach number examined. The results at the cruise Mach number, $M = 3.0$, will be discussed first followed by a discussion of the aerodynamic trends above and below the design Mach number. A complete listing of the force and moment data obtained from this test with nacelles on and off is presented in appendix A.

Shown in figures 6(a) and 6(b) are the experimental wind tunnel results at cruise, $M = 3.0$, compared with the linear theory estimates. Figure 6(a) shows that at all angles of attack there is a positive increment in lift coefficient due to nacelle presence. Because these nacelle-induced lift effects occur aft of the moment reference center, a negative increment in zero-lift pitching moment results, as does a slightly stabilizing pitch-curve slope increment. An additional contribution to the negative $C_{m,0}$ increment is due to the nacelle axial force or drag that occurs below the moment reference center. The configuration has a negative static margin at $C_L = 0$ and experiences pitch-up at about $C_L = 0.05$. Linear theory accurately predicts the incremental changes in the lift due to the nacelles. Typical for linear theory, it does not predict the pitch-up because of the lack of vortex modeling. Results from an Euler solution that more accurately predicts the pitching moment and the stability trends of the configuration will be shown later. The experimental drag characteristics presented in figure 6(b) show a zero-lift drag penalty due to the addition of nacelles. However, due to the favorable nacelle-interference lift characteristic discussed above, the drag due to lift decreases for the nacelles-on case when compared with the nacelles-off case. The addition of the nacelles results in a sizable reduction (0.5 lift-to-drag ratio) in $(L/D)_{\max}$. Further optimization studies are needed to assess drag increment due to nacelle addition, since very small amounts of drag are so costly on HSCT's.

The addition of nacelles causes a larger increase in lift at the lower Mach numbers than at the higher Mach numbers, as can be seen in figures 6–12, although the drag increments due to the nacelles remain approximately the same at $C_L = 0$ for the complete Mach number range. A break in the stability level occurs at the lower Mach numbers. This break becomes milder and occurs at lower lift as

Mach number increases to about 2.8. Experimental $(L/D)_{\max}$ values decrease as Mach number increases, from about 7 at the lower Mach numbers to about 6 at the higher Mach numbers. A summary of the experimental lift-curve slope, minimum drag, stability level at $C_L = 0$, and drag due to lift for the complete Mach number range is shown in figures 13–16. Typical effects of supersonic Mach number variation occur as Mach number increases, lift-curve slope and minimum drag decrease, and pitch-curve slope and drag due to lift increase.

Higher order theoretical prediction of the aerodynamic characteristics (Euler and Navier-Stokes) are compared with the experimental data in figure 17. The Euler results shown in figures 17 and 18 were obtained using the method reported in reference 20. This method uses an implicit marching technique tailored to supersonic free-stream flow. The marching is performed on a spherical coordinate system centered on the configuration apex with steps taken in the radial direction. The solution is obtained at a given marching step by using a node-centered, hybrid finite-volume, central difference scheme with explicit artificial viscosity. Computational grids are automatically generated within the code at each marching step.

The Navier-Stokes results shown in figures 17 and 18 were obtained using the method reported in reference 21. In this method, the full Navier-Stokes equations are simplified by making a thin-layer assumption that includes the viscous terms only in the direction normal to solid surfaces. Turbulence is accounted for with eddy viscosity obtained from the Baldwin-Lomax algebraic turbulence model. The thin-layer, Reynolds-averaged, Navier-Stokes equations are discretized by a finite-volume method with spatial derivatives expressed as central differences. Steady-state solutions are obtained using a five-stage Runge-Kutta scheme for iterating in pseudotime. Previous analyses of this configuration by the above methods have been reported in references 21–23. The Navier-Stokes and Euler results shown here were obtained from references 21 and 22, respectively.

Shown in figure 17 are the comparisons of the theoretical and experimental longitudinal aerodynamic characteristics at $M = 3.0$ without nacelles. It is shown that linear theory accurately predicts lift. The Euler and Navier-Stokes solutions accurately predict both lift and drag for the complete C_L range.

This configuration was originally designed using linear theory to be neutrally stable at $M = 3.0$; however, the wind tunnel results show that it has about a 4-percent pitch-up ($\Delta C_m / \Delta C_L$) at this Mach

number (see fig. 14). The Euler solution accurately predicts the stability trends of the configuration, although the absolute pitching-moment values are underpredicted. Navier-Stokes solutions for C_m were not available for comparison.

To further compare the theoretical results with the experimental data, figure 18 shows the surface pressure distributions at two spanwise locations, $x = 15.6$ and $x = 20.7$, at $\alpha = 5^\circ$ along with the three theoretical solutions at $M = 3.0$. The Navier-Stokes solution predicted the mild expansion at the leading edge. The Euler and Navier-Stokes solutions both accurately predicted the vortex-induced suction pressure peak near $\eta = 0.50$. This vortex can be seen in the vapor screen and oil flow photographs at the same conditions in figure 19. The oil flow photograph also shows the separation at the trailing edge, illustrated by the oil accumulation. The vapor screen photographs are compared with the Navier-Stokes vortex system in figure 20. Additional vapor screen and oil flow photographs are presented in appendixes B and C, respectively. A complete set of pressure plots are shown in appendix D and the tabulated pressure coefficients are presented in appendix E on microfiche. (See back cover of report.)

Extrapolation to Full Scale

The extrapolation of wind tunnel drag data to full-scale conditions includes corrections for both drag due to lift and zero-lift drag. The zero-lift drag corrections can be further subdivided into four categories: (1) the skin-friction-coefficient correction for Reynolds number, (2) drag contribution due to full-scale surface roughness, (3) drag-coefficient correction due to geometry differences between the model and the full-scale airplane, and (4) grit drag necessary to fix the boundary-layer transition in the wind tunnel.

Zero-lift drag coefficient increments applied to the wind tunnel data are shown in table V. The largest increment is the skin-friction-coefficient correction necessary to account for the boundary-layer properties at the wind tunnel Reynolds number. The skin-friction coefficient for the wind tunnel model was calculated using the Sommer and Short T' method (ref. 17) at the test condition unit Reynolds number with the following assumptions: a fully turbulent boundary layer; a surface emittance of 0.8; and a surface sand grain roughness, for polished metal, of 2×10^{-5} in. Friction drag of the full-scale configuration was calculated using the same method for an altitude of 65 000 ft with the following assumptions: a fully turbulent boundary layer; a U.S. 1962 standard atmosphere; a surface emittance of 0.8; and

a surface sand grain roughness, for carefully applied smooth matte paint, of 2.5×10^{-4} in. The drag increment due to full-scale surface roughness and miscellaneous surface defects was assumed to be 6 percent of the airplane skin-friction drag across the supersonic Mach number range (ref. 24). A geometry-related drag increment was necessary because of model truncation and a model thickness increase of 0.020 in. due to manufacturing constraints. This geometry-related drag increment included both zero-lift wave drag (ref. 25) and skin friction drag (ref. 17) and was applied to the wind tunnel data because of the changes in the volume and wetted area of the model. The last zero-lift drag increment to be applied to the wind tunnel data was a grit drag correction estimated in accordance with reference 14. An empirically derived drag-due-to-lift increment, calculated by the method of reference 26, was also applied to the wind tunnel data to account for Reynolds number effects on the attainable leading-edge thrust. Although this increment is not large enough to significantly influence the extrapolated results, it was included for completeness.

Because of possible nacelle geometry modeling errors and the relatively large nacelle base area, all drag corrections presented are for the nacelle-off wind tunnel data. A trim drag increment was not assessed because of the tailless design, in which the center of gravity would be controlled by fuel transfer to effect longitudinal trim. As illustrated in figure 21, applying these drag increments to the nacelle-off wind tunnel data results in an extrapolated full-scale $(L/D)_{\max}$ of 7.9 compared with 6.3 for the wind tunnel test at Mach 3.0. Also shown are the value of C_L at cruise and the maneuver load factor limit of 2.5g for a transport category aircraft.

From the aerodynamic characteristics of the full-scale configuration, as described in reference 8, linear theory predicted $(L/D)_{\max} = 9.4$ at the reference altitude of 40 000 ft. For a direct comparison with the extrapolated wind tunnel data, the predicted drag polars were modified to the cruise altitude of 65 000 ft and the increments due to nacelles and vectored thrust were removed. Figure 22 presents a comparison of the extrapolated wind tunnel data with the predicted aerodynamic characteristics of the full-scale configuration without nacelles. The predicted value of $(L/D)_{\max}$ of 8.6 is shown to be higher than the extrapolated wind tunnel data, with better agreement at the lower lift coefficients.

Figure 22 indicates that linear theory tends to underpredict the drag due to lift. This discrepancy is due to overpredicted upwash and suction on the wing along with some nonlinear effects. The application

of a recently published empirical method (ref. 27) to adjust the linear theory drag-due-to-lift prediction to account for these discrepancies is shown in figure 23. As can be seen, the value of $(L/D)_{\max}$ of 8.0 from empirically corrected linear theory agrees better with the experimental data. Employing these empirical corrections during the design process would allow for reduced camber and twist, thus producing a lighter wing structure as well as lower drag due to lift at the cruise lift coefficient.

Concluding Remarks

An investigation was conducted to determine the supersonic aerodynamic characteristics of the proposed NASA Langley Mach 3.0 high-speed civil transport configuration. Testing was performed in the Langley Unitary Plan Wind Tunnel at a Mach number range between 1.6 and 3.6. Forces, moment, and pressure data were obtained. The aerodynamic effects from the presence of nacelles were also investigated. Theoretical analysis using linear theory, Euler, and Navier-Stokes methods were compared with experimental results. Extrapolation of the wind tunnel data to full-scale conditions was performed and compared with the preliminary predictions from a linear method.

Experimental results show that maximum lift-to-drag ratio results varied from about 7 at the lower Mach numbers to about 6 at the higher Mach numbers. An unstable break in the pitching moment occurred at a lift coefficient of about 0.1 at Mach 1.6. The break became milder and occurred at lower lift as

Mach number increased to about 2.8. Typical effects due to engine nacelle addition were found to be an increase in lift, an increase in drag, and a decrease in lift-to-drag ratio.

Euler and Navier-Stokes results at Mach 3 showed very good agreement with the experimental data for lift, drag, pitching moment (Euler only), and surface pressures. The lift-curve slope and drag polars predicted with the linear method originally used to design the configuration were generally in good agreement with the experimental results over the Mach number range tested. However, the stability characteristics (trend and level) of the configuration were not accurately predicted using linear theory. Although the higher order methods were better for predicting all the characteristics, the linear methods used herein should continue to serve as a valuable aid in the preliminary design stages of high-speed vehicles.

Preliminary aerodynamic predictions were optimistic for the full-scale configuration. Extrapolating wind tunnel data to full-scale conditions showed linear theory underpredicted the drag due to lift. Applying a recently published empirical method to adjust the linear theory prediction resulted in an excellent agreement with the wind tunnel results, particularly at and below the design cruise lift coefficient.

NASA Langley Research Center
Hampton, VA 23681-0001
August 20, 1993

Table I. Configuration Geometry

Wing:

Theoretical area (reference), ft ²	1.235
Span, in.	18.19
Mean aerodynamic chord, in.	15.66
Moment reference center, in.	19.33

Leading-edge equations:

$0 < y < 1.13$	$x_{le} = 0.29y^2$
$1.13 \leq y < 4.13$	$x_{le} = 5.43y - 3.06$
$4.13 \leq y < 4.83$	$x_{le} = 1.90y + 11.53$
$4.83 \leq y < 7.28$	$x_{le} = 4/3y + 14.26$
$7.28 \leq y < 9.06$	$x_{le} = -10.33\sqrt{9.10 - y} + 28.80$

Trailing-edge equations:

$0 \leq y < 2.42$	$x_{te} = 25.27$
$2.42 \leq y < 4.23$	$x_{te} = 0.457y + 24.16$
$4.23 \leq y < 6.40$	$x_{te} = 0.52y + 23.89$
$6.40 \leq y < 7.28$	$x_{te} = 0.57y + 23.56$
$7.28 \leq y < 9.10$	$x_{te} = 0.79y + 21.99$

Nacelles:

Length, in.	5.52
Inlet capture area (each), in ²	0.6355
Base area (each), in ²	0.5326
Longitudinal distance from original nose of model to lip of nacelle, in.	20.88
Lateral distance from centerline of model to centerline of nacelle lip, in.	± 2.11
Vertical distance from model reference line to nacelle centerline, in.	1.81
Wetted area, in ²	15.45
Duct misalignment angle, ϵ , deg	0.9

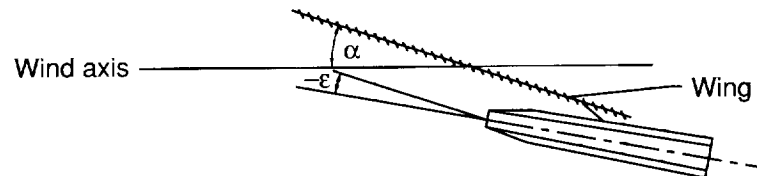


Table II. Pressure Orifice Locations

x	y
8.88 ↓	0.00
	0.35
	0.71
	1.06
	1.41
	1.76
	2.11
15.62 ↓	0.00
	0.35
	0.71
	1.06
	1.41
	1.76
	2.11
	2.47
	2.82
	3.17
	3.30
20.67 ↓	0.00
	0.35
	0.71
	1.06
	1.41
	1.76
	2.11
	2.47
	2.82
	3.17
	3.52
	3.87
	4.23
	4.58

x	y
*20.67 ↓	-1.41
	-1.76
	-2.11
	-2.47
	-2.82
*23.00 ↓	-0.40
	-0.60
	-0.80
	-1.00
	-1.20
	-3.00
	-3.20
	-3.40
	-3.60
	-3.80
	-4.00
8.88 10.56 12.25 13.93 15.62 17.30 18.99 20.67 ↓	2.11
23.00 23.47 23.95 24.42 24.89 25.37 ↓	6.04

*Lower surface.

Table III. Accuracy¹

(a) Aerodynamic coefficient accuracy

M	C_N	C_A	C_m	C_L	C_D
1.6	± 0.0010	± 0.00014	± 0.00009	± 0.0010	± 0.00025
2.0	± 0.0012	± 0.00016	± 0.00011	± 0.0012	± 0.00024
2.4	± 0.0013	± 0.00018	± 0.00012	± 0.0013	± 0.00024
2.8	± 0.0014	± 0.00019	± 0.00014	± 0.0014	± 0.00025
3.0	± 0.0014	± 0.00020	± 0.00015	± 0.0014	± 0.00025
3.2	± 0.0015	± 0.00021	± 0.00015	± 0.0015	± 0.00026
3.6	± 0.0017	± 0.00023	± 0.00017	± 0.0017	± 0.00027

(b) Overall accuracy of ESP system,
including calibration accuracy

M	q	C_p
1.6	454.8	± 0.0066
2.0	448.5	± 0.0066
2.4	419.1	± 0.0072
2.8	378.8	± 0.0097
3.0	357.2	± 0.0084
3.2	335.6	± 0.0089
3.6	293.7	± 0.0102

¹A limited analysis was performed to estimate the absolute uncertainty of the aerodynamic coefficient values. The coefficient uncertainties were based on uncertainties of the key parameters used to determine the coefficients. These parameters are the balance loads, Mach number, total pressure, balance chamber pressure (for the axial force and drag coefficient), and angle of attack. The method of reference 28 was used to calculate the uncertainty values shown in table III(a). The coefficient uncertainties were determined at typical cruise angle of attack conditions ($\alpha \approx 2^\circ$). The repeatability of the data is estimated to be within half the absolute uncertainty.

Table IV. Nacelle Base Drag and Internal Flow Corrections

(a) Nacelle base drag correction

M	$C_{D,nb}$
1.6	0.0017
2.0	.0013
2.4	.0009
2.8	.0007
3.0	.0006
3.2	.0005
3.6	.0004

(b) Nacelle internal flow drag correction

α	$C_{D,i}$ at—						
	Mach 1.6	Mach 2.0	Mach 2.4	Mach 2.8	Mach 3.0	Mach 3.2	Mach 3.6
0.00	0.0004	0.0004	0.0004	0.0003	0.0003	0.0003	0.0003
1.00	.0004	.0004	.0004	.0004	.0003	.0003	.0003
2.00	.0005	.0004	.0004	.0004	.0004	.0004	.0003
3.00	.0005	.0005	.0004	.0004	.0004	.0004	.0004
4.00	.0005	.0005	.0005	.0005	.0005	.0004	.0004
6.00	.0007	.0006	.0006	.0006	.0006	.0006	.0006
8.00	.0008	.0008	.0008	.0008	.0008	.0008	.0008
10.00	.0010	.0011	.0011	.0011	.0011	.0011	.0012

Table V. Zero-Lift Drag Coefficient Increments
Applied to Wind Tunnel Data

		Drag increment
1. Skin friction drag:		
Model	0.00555	
Full scale	<u>0.00260</u>	
		−0.00295
2. Roughness drag		0.00018
3. Geometry-related drag:		
Wave drag:		
Model	0.00172	
Full scale	<u>0.00171</u>	
	0.00001	
Skin friction drag ¹ :		
Model	0.00525	
Full scale	<u>0.00555</u>	
	<u>0.00030</u>	
		0.00029
4. Grit drag		<u>−0.00026</u>
Total		<u>−0.00274</u>

¹At tunnel Reynolds number.



Figure 1. Artist's illustration of the NASA HSCT concept.

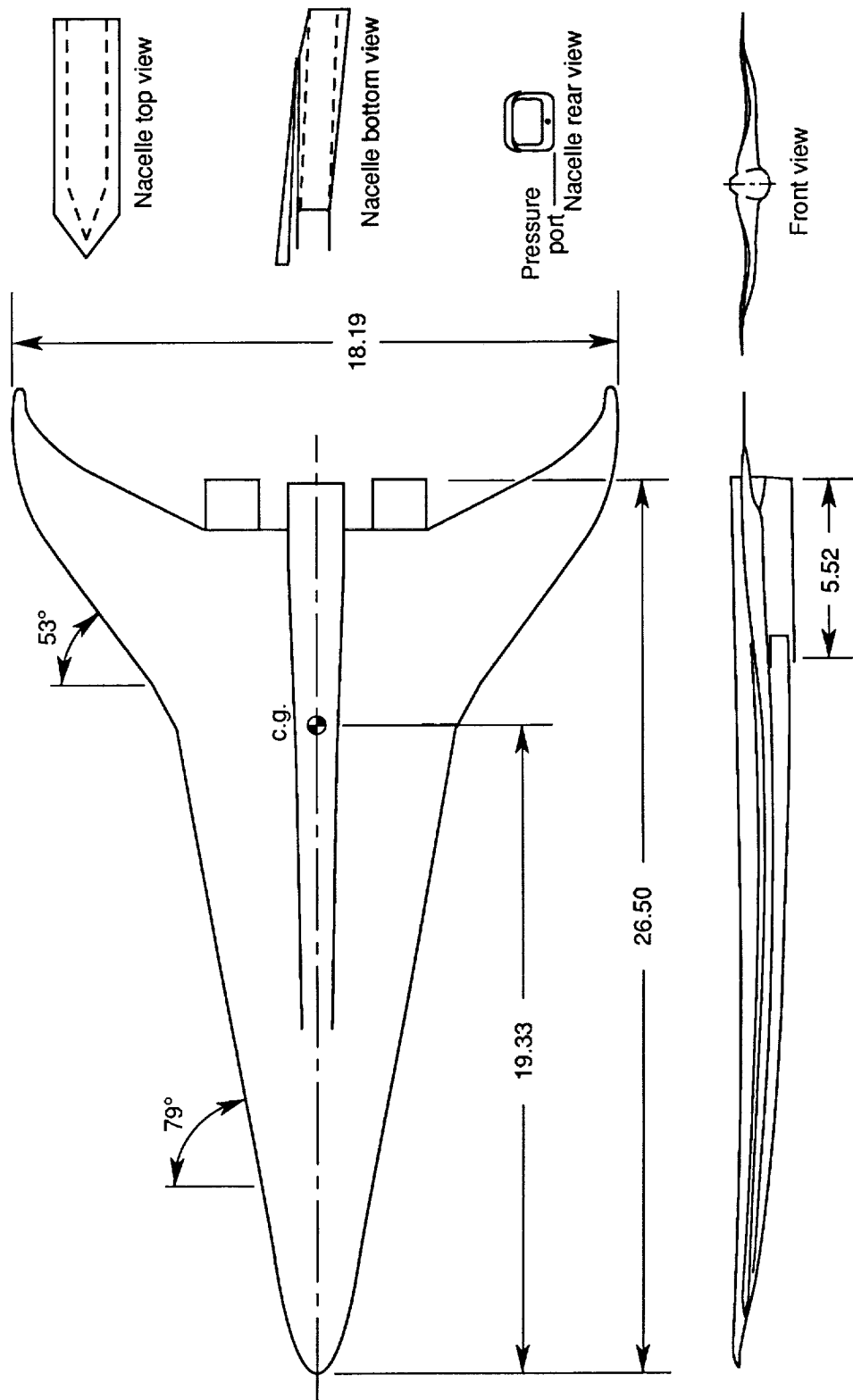


Figure 2. Planform drawing of the wind tunnel model and nacelle. Units are in inches.

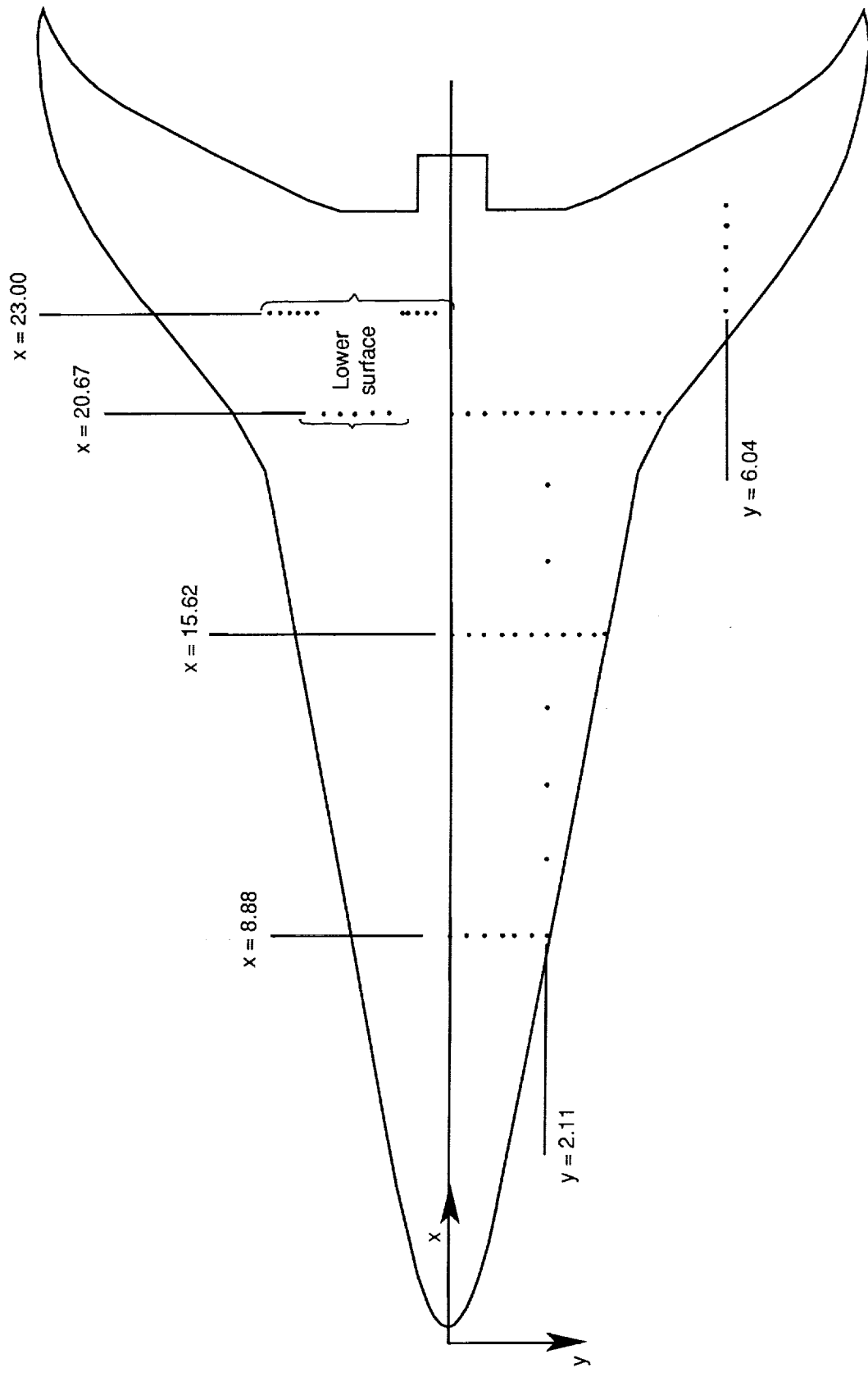
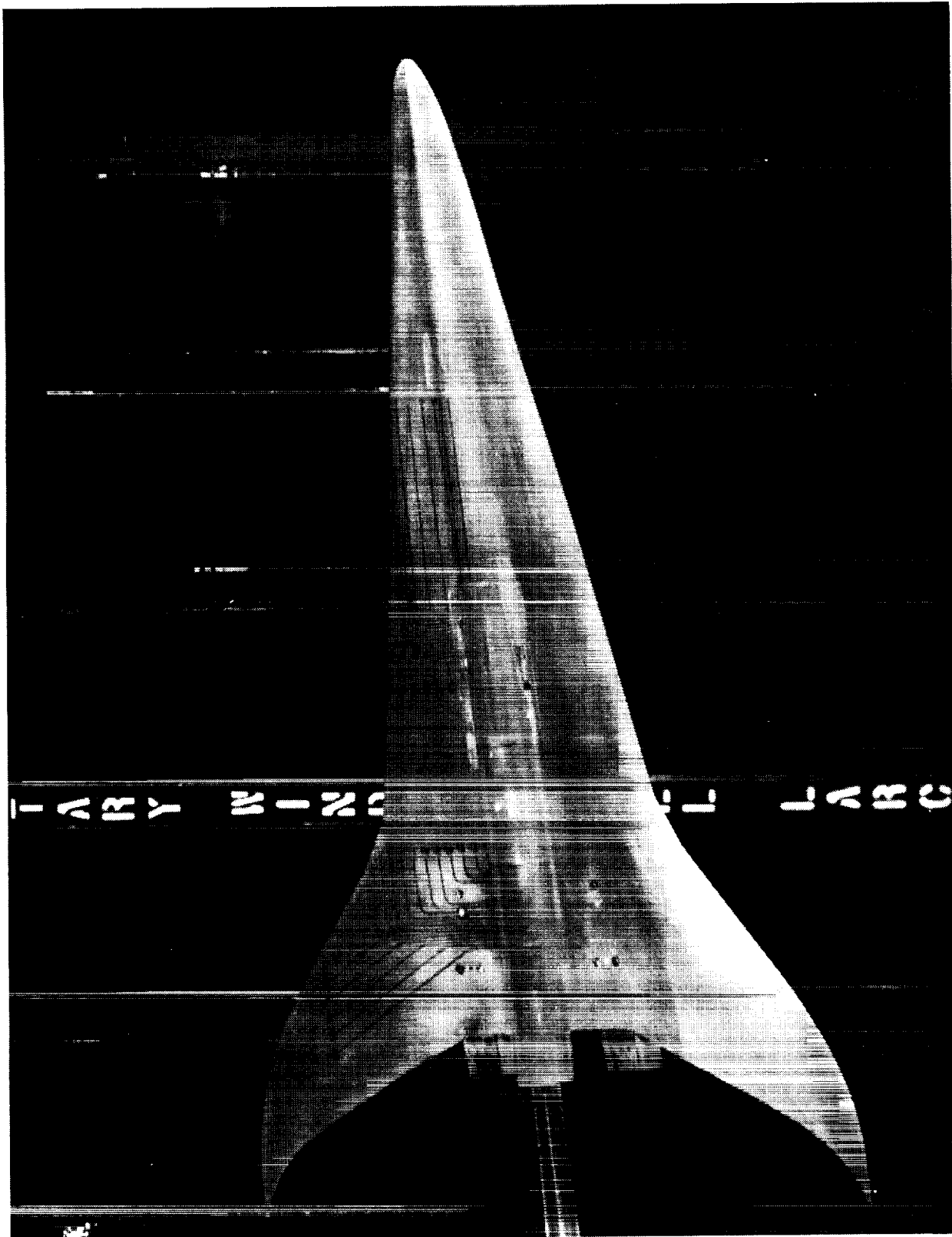


Figure 3. Pressure orifice locations.



L-90-8459

Figure 4. HSCT wind tunnel model installed in the UPWT.

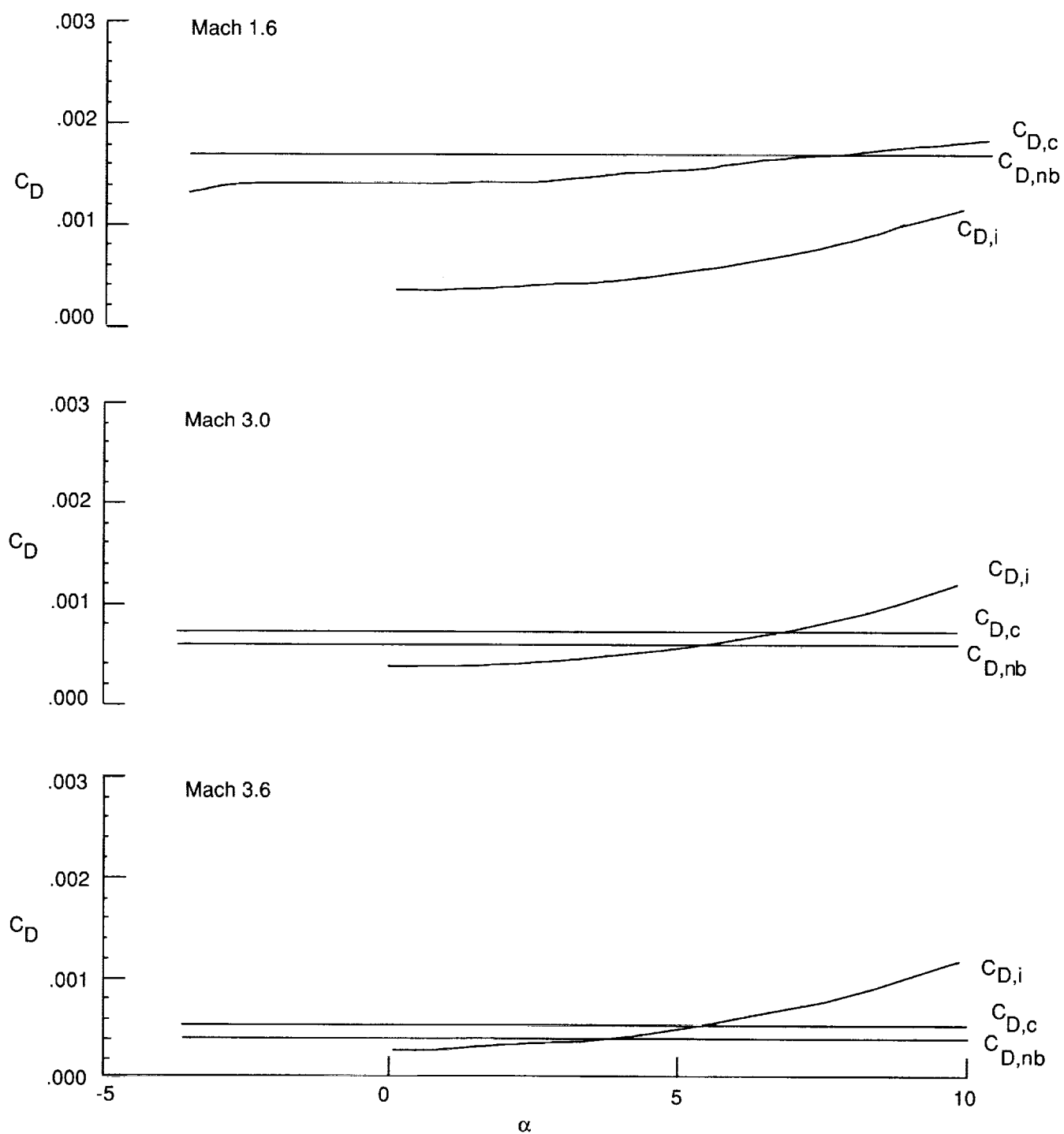
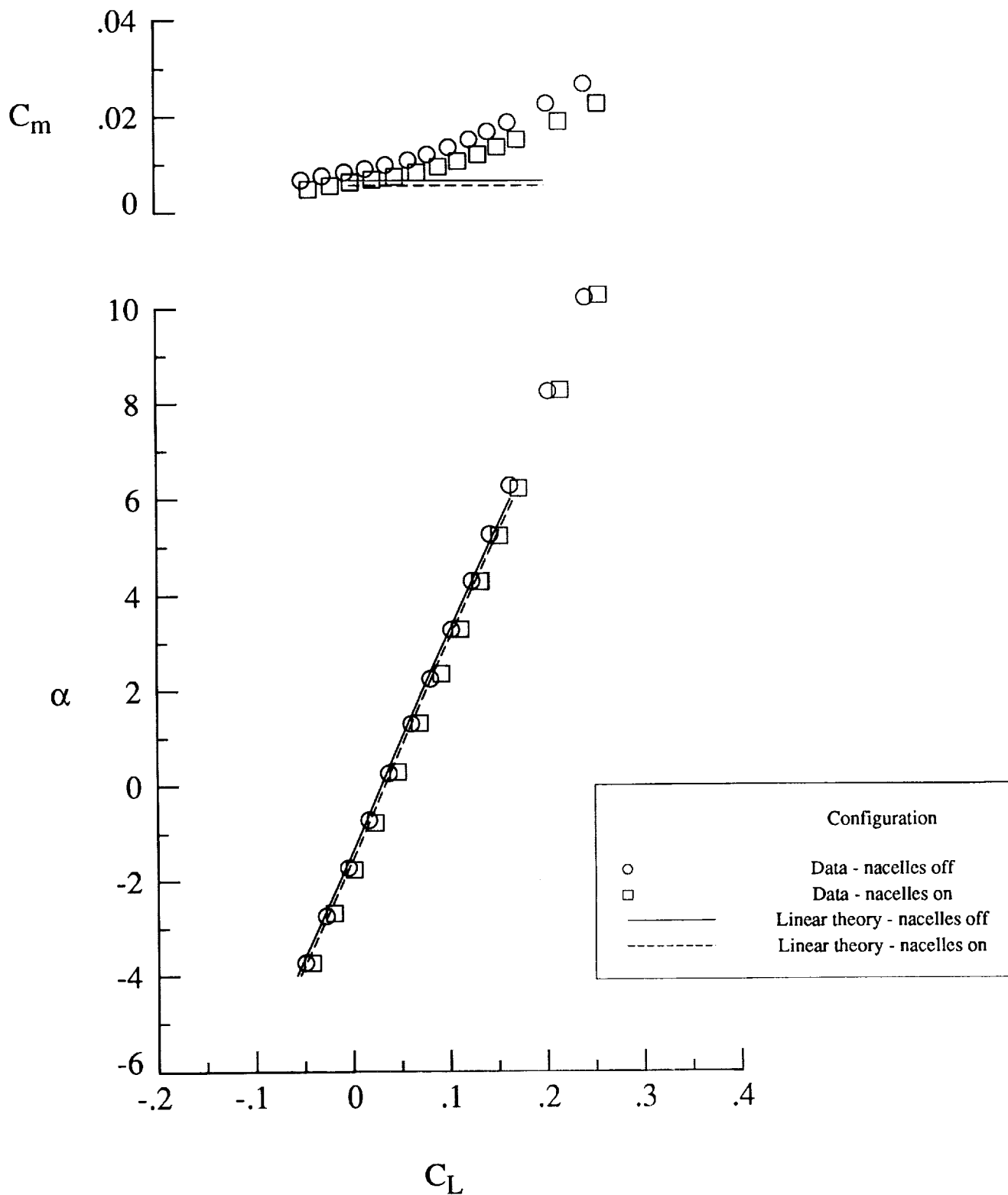
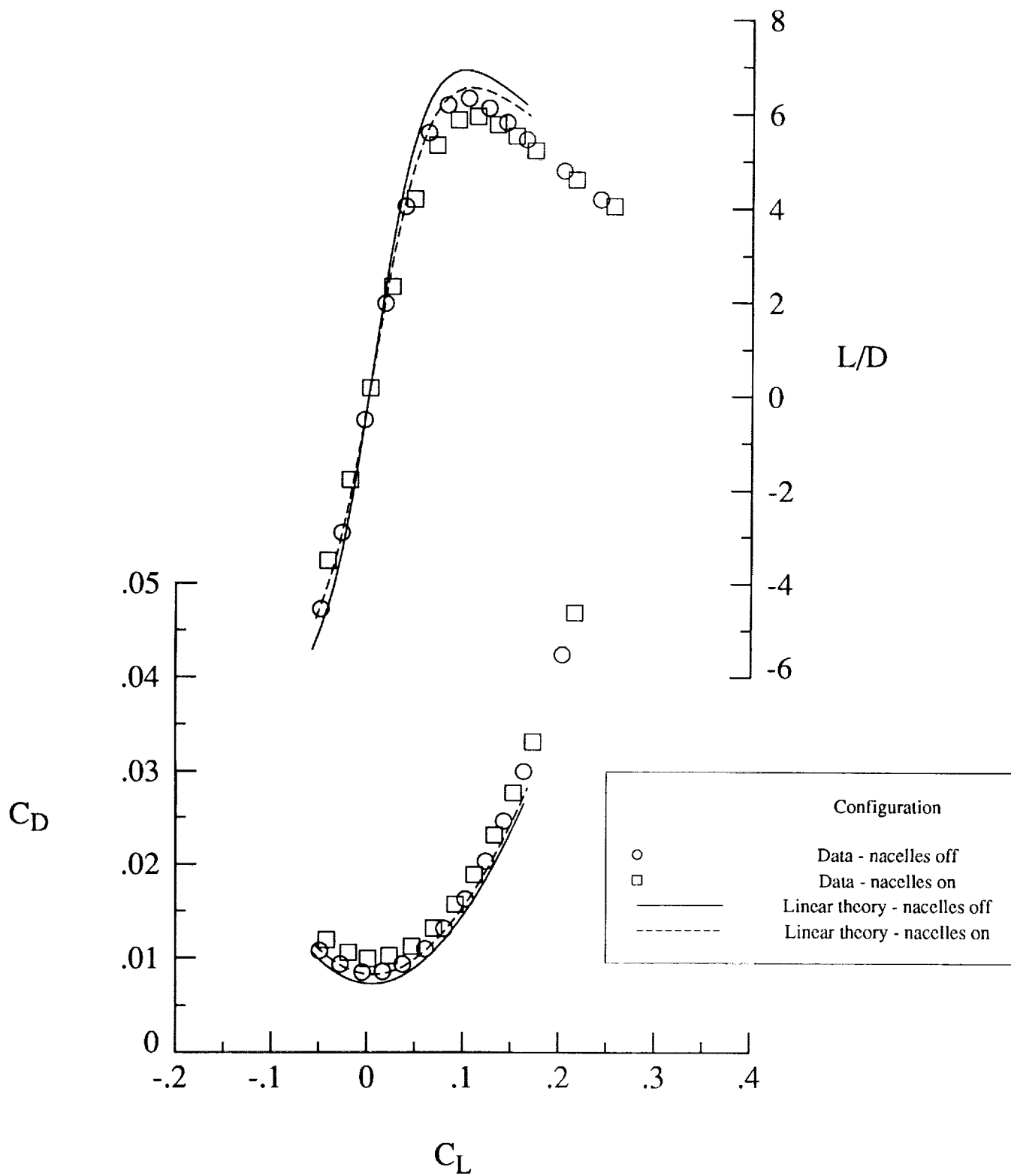


Figure 5. Typical chamber, nacelle internal flow, and nacelle base drag corrections.



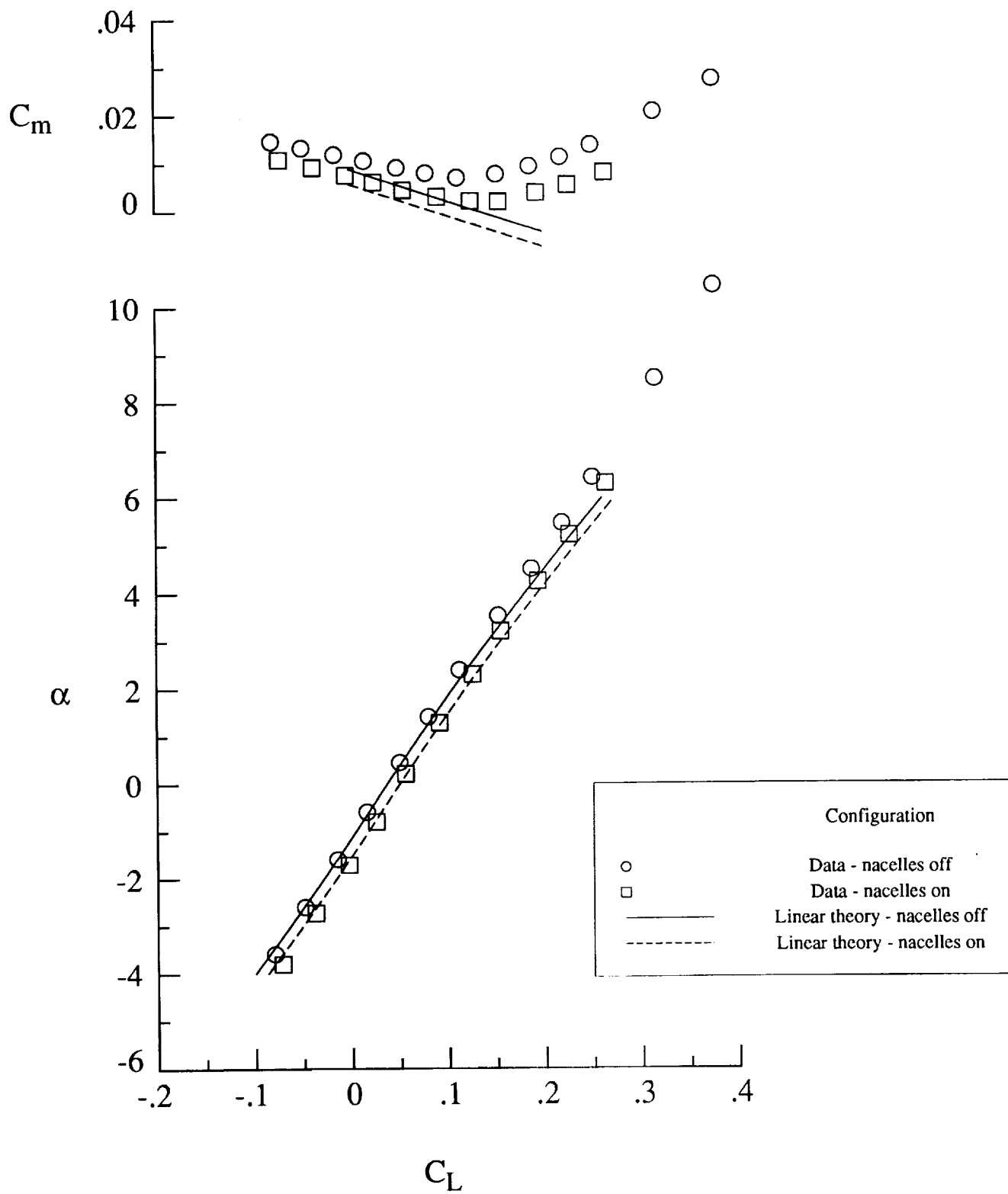
(a) Longitudinal aerodynamic characteristics.

Figure 6. Wind tunnel results and linear theory predictions. $M = 3.0$.



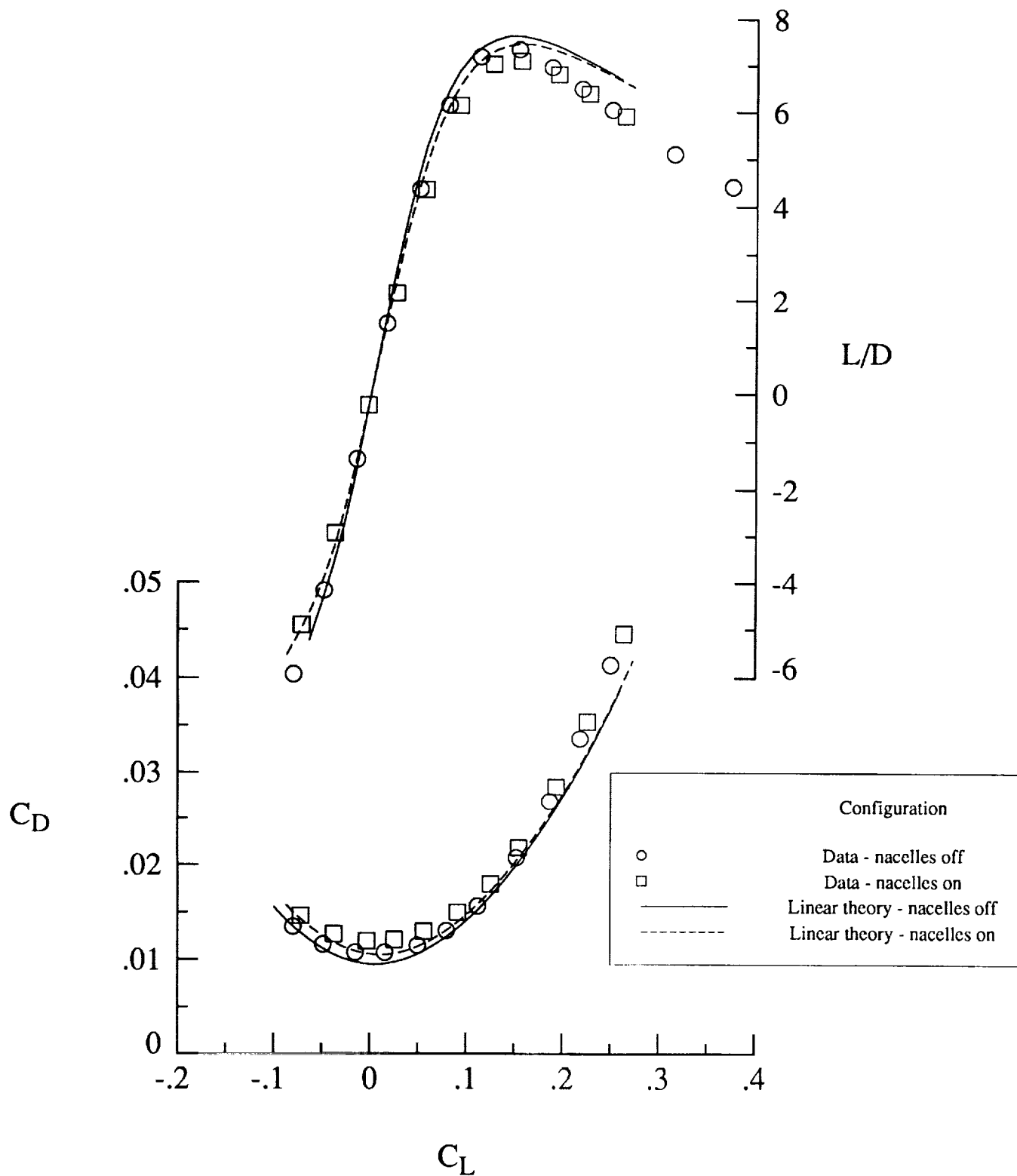
(b) Drag polar and L/D plots.

Figure 6. Concluded.



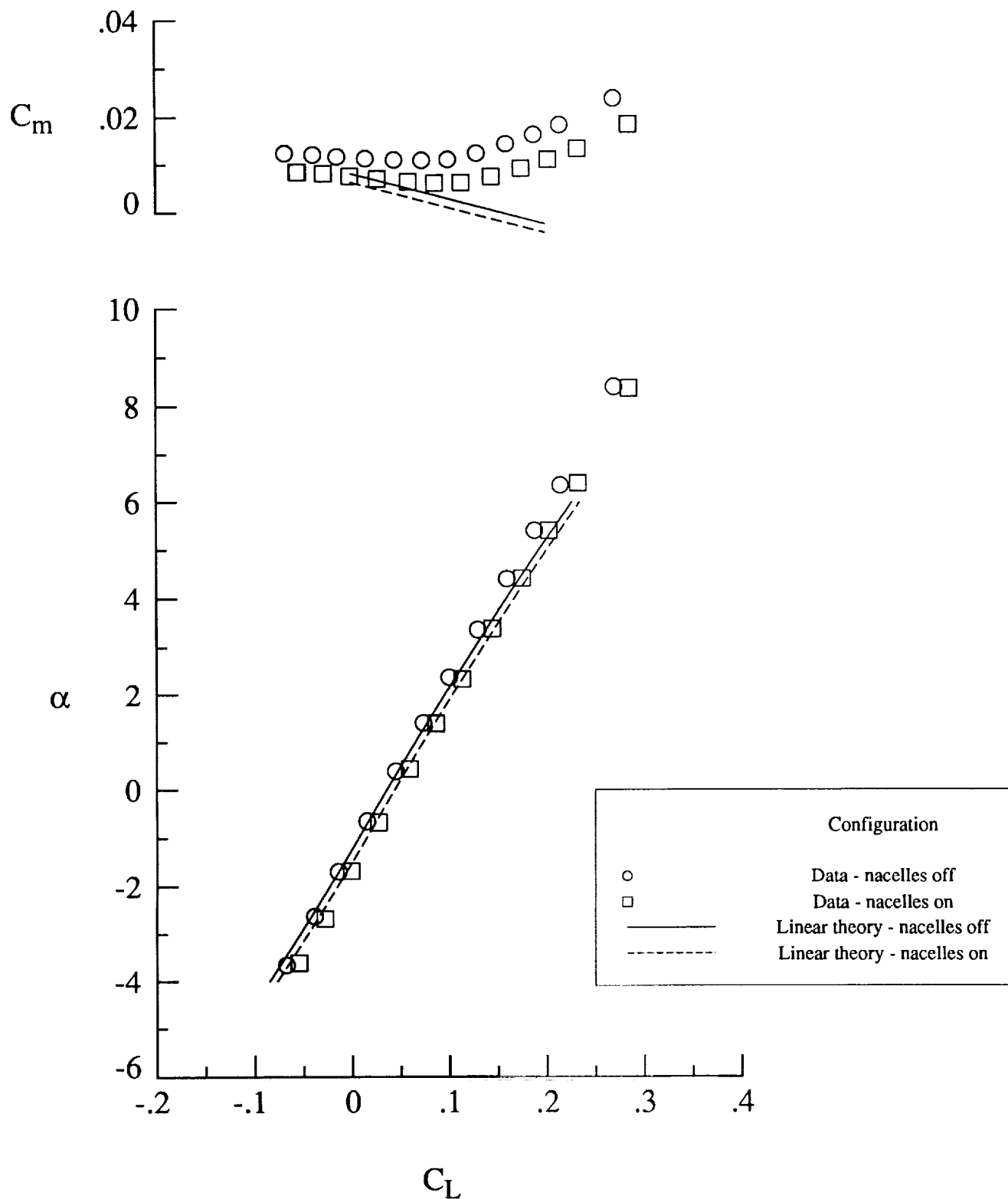
(a) Longitudinal aerodynamic characteristics.

Figure 7. Wind tunnel results and linear theory predictions. $M = 1.6$.



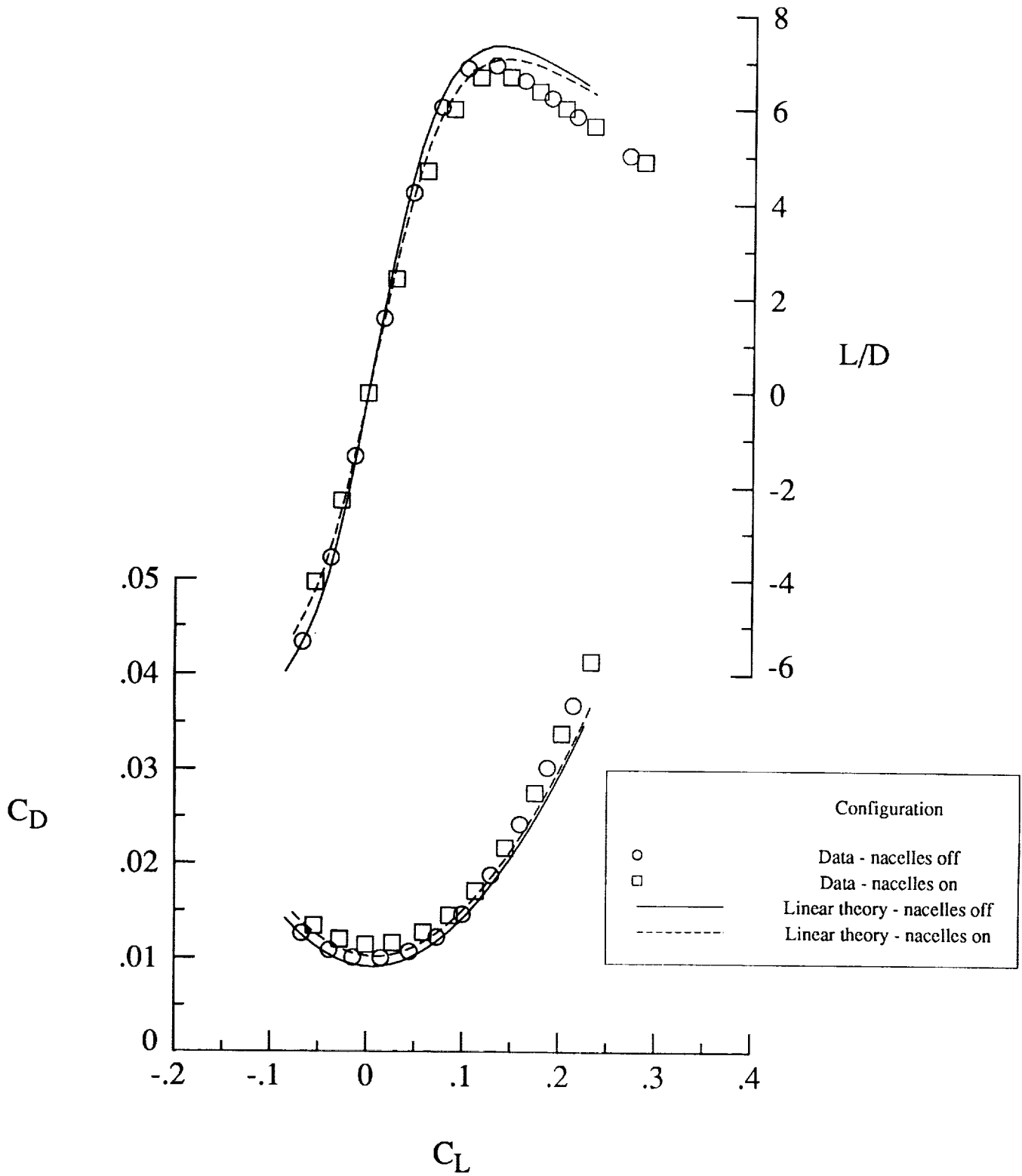
(b) Drag polar and L/D plots.

Figure 7. Concluded.



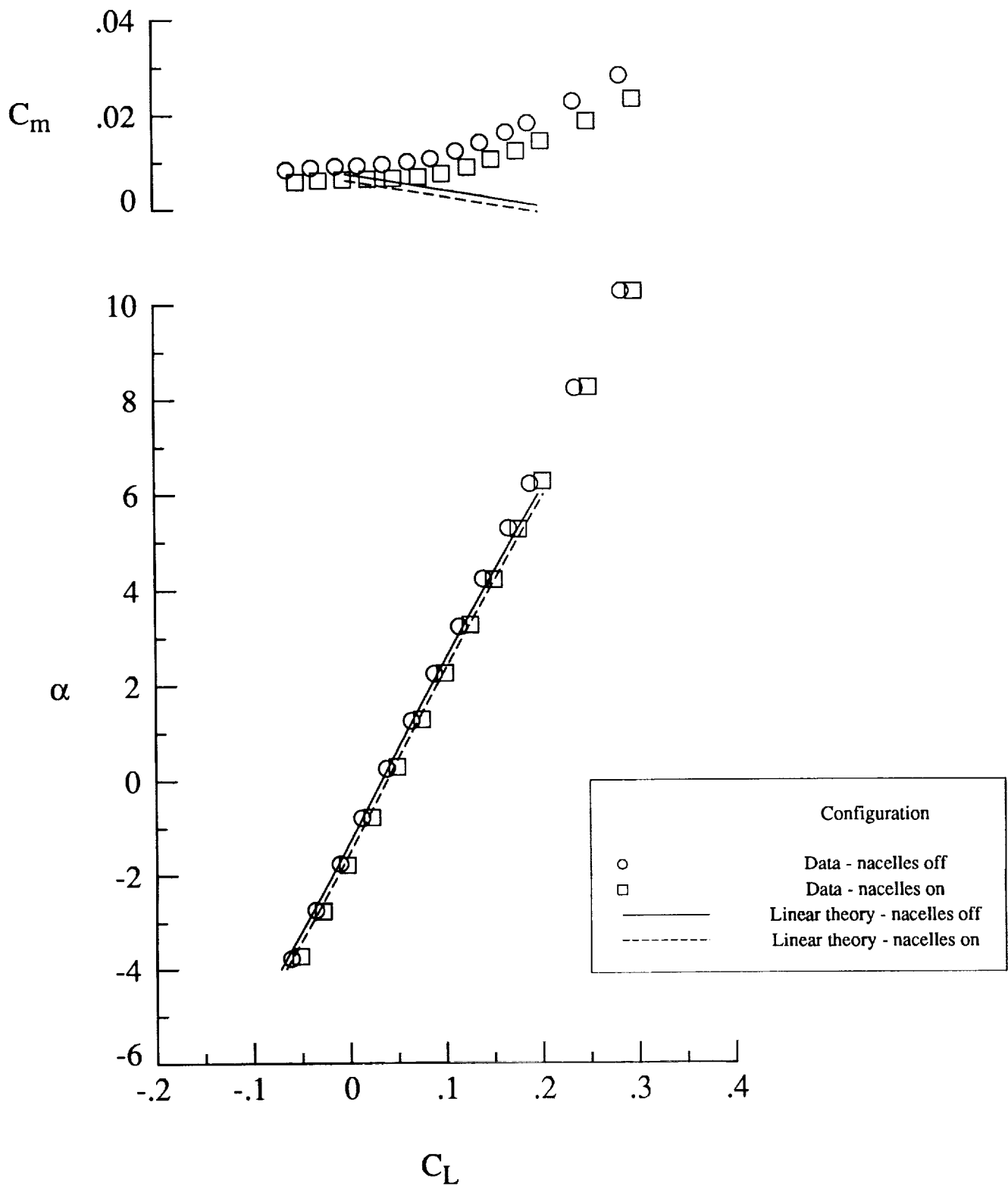
(a) Longitudinal aerodynamic characteristics.

Figure 8. Wind tunnel results and linear theory predictions. $M = 2.0$.



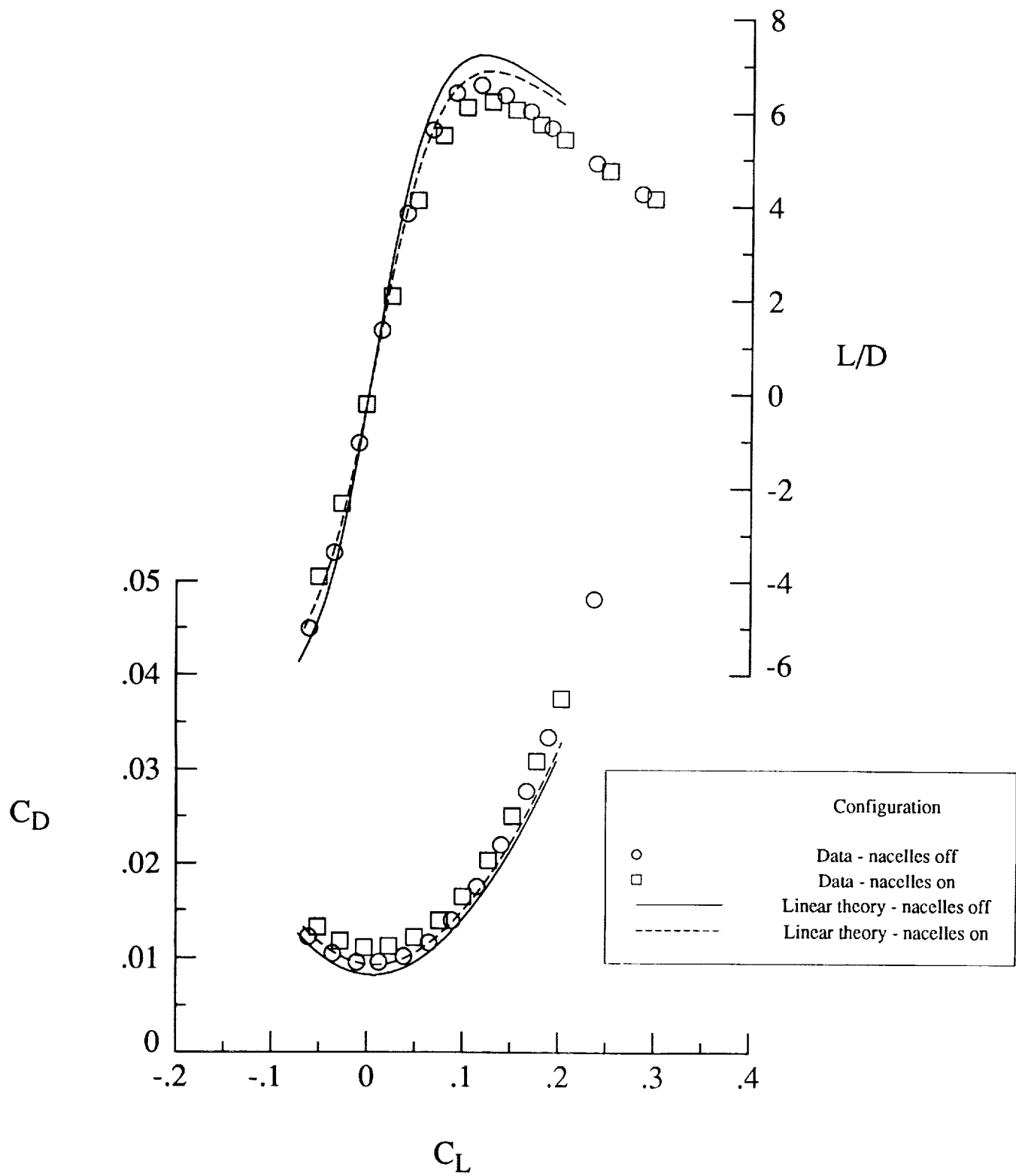
(b) Drag polar and L/D plots.

Figure 8. Concluded.



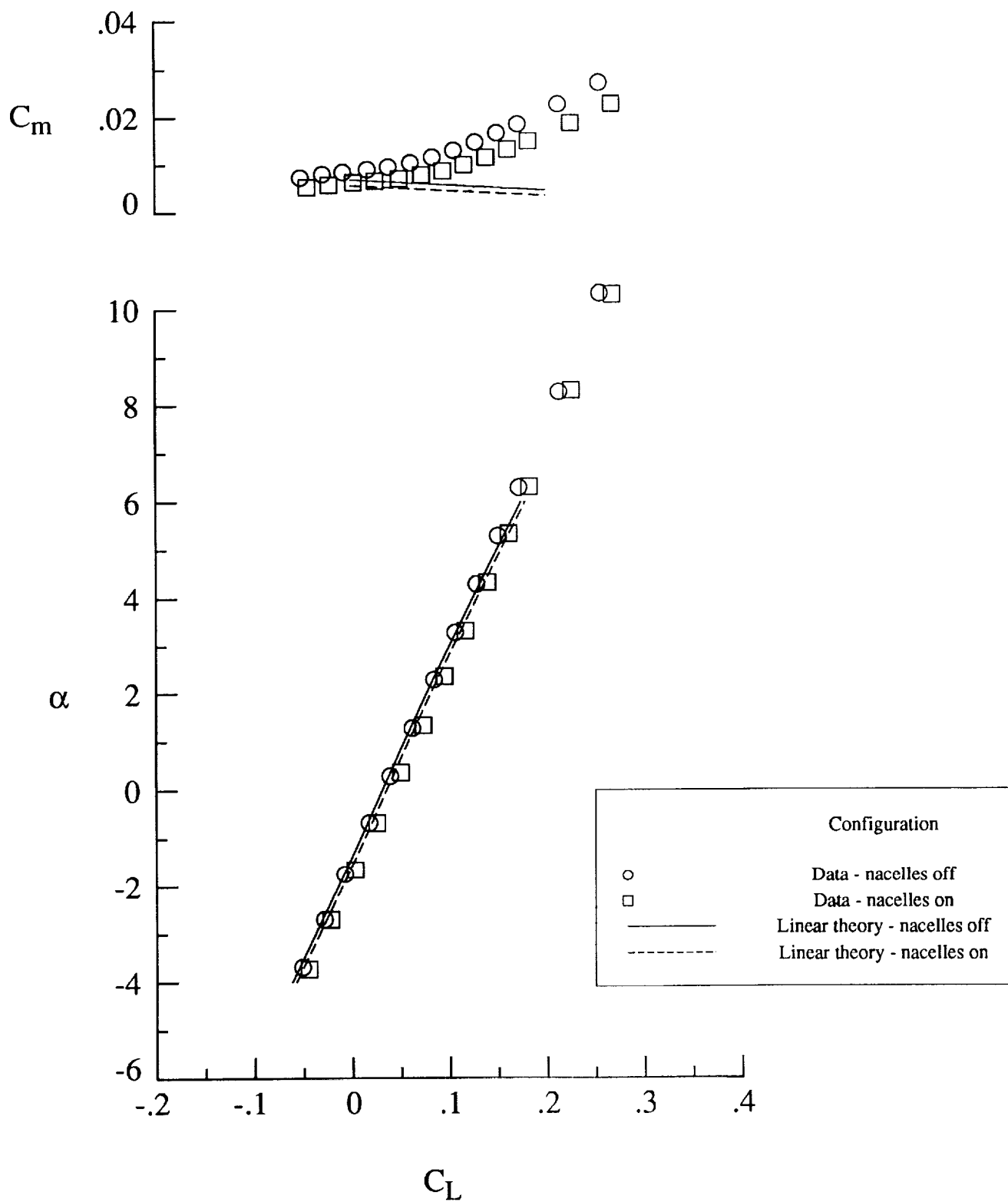
(a) Longitudinal aerodynamic characteristics.

Figure 9. Wind tunnel results and linear theory predictions. $M = 2.4$.



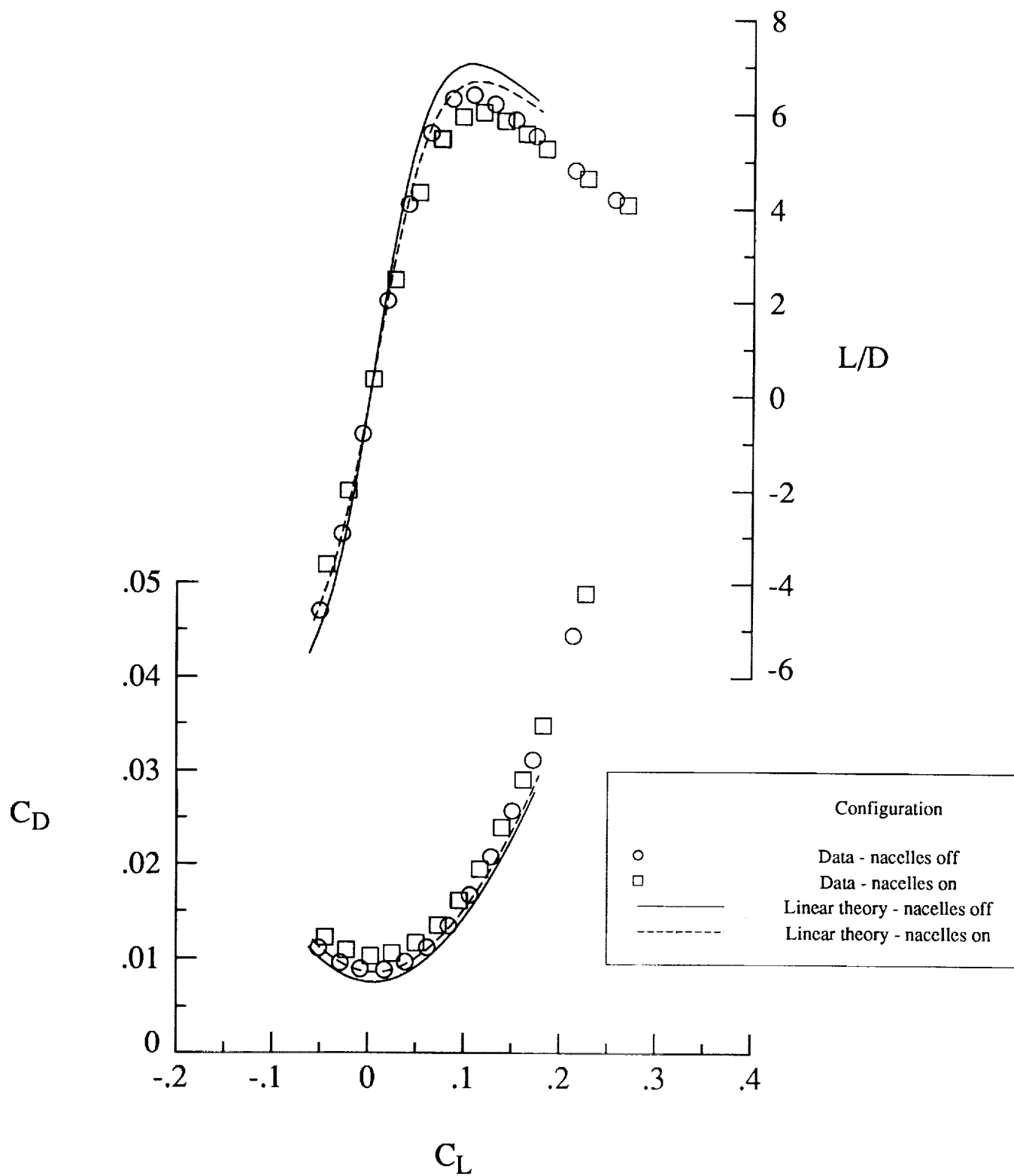
(b) Drag polar and L/D plots.

Figure 9. Concluded.



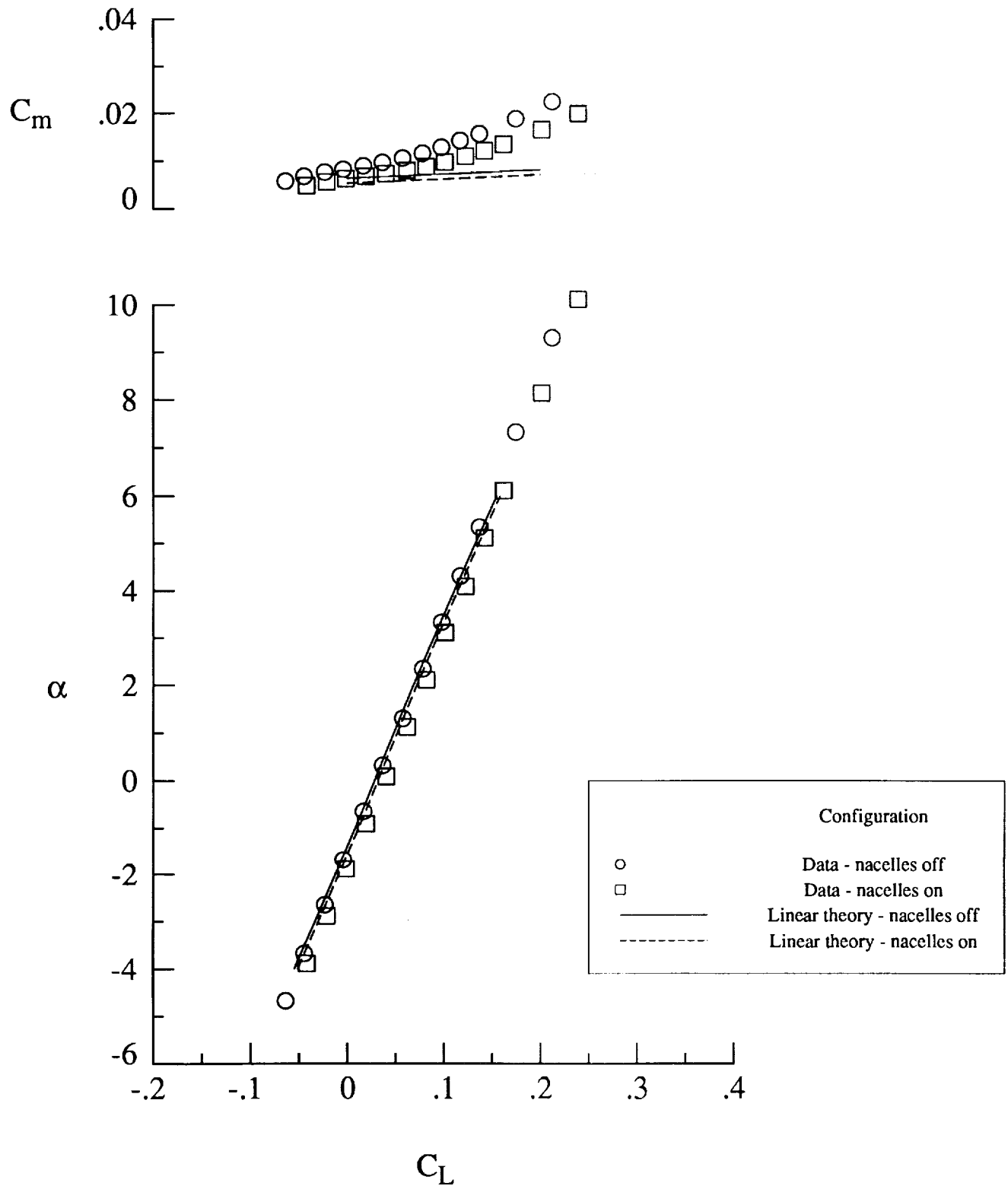
(a) Longitudinal aerodynamic characteristics.

Figure 10. Wind tunnel results and linear theory predictions. $M = 2.8$.



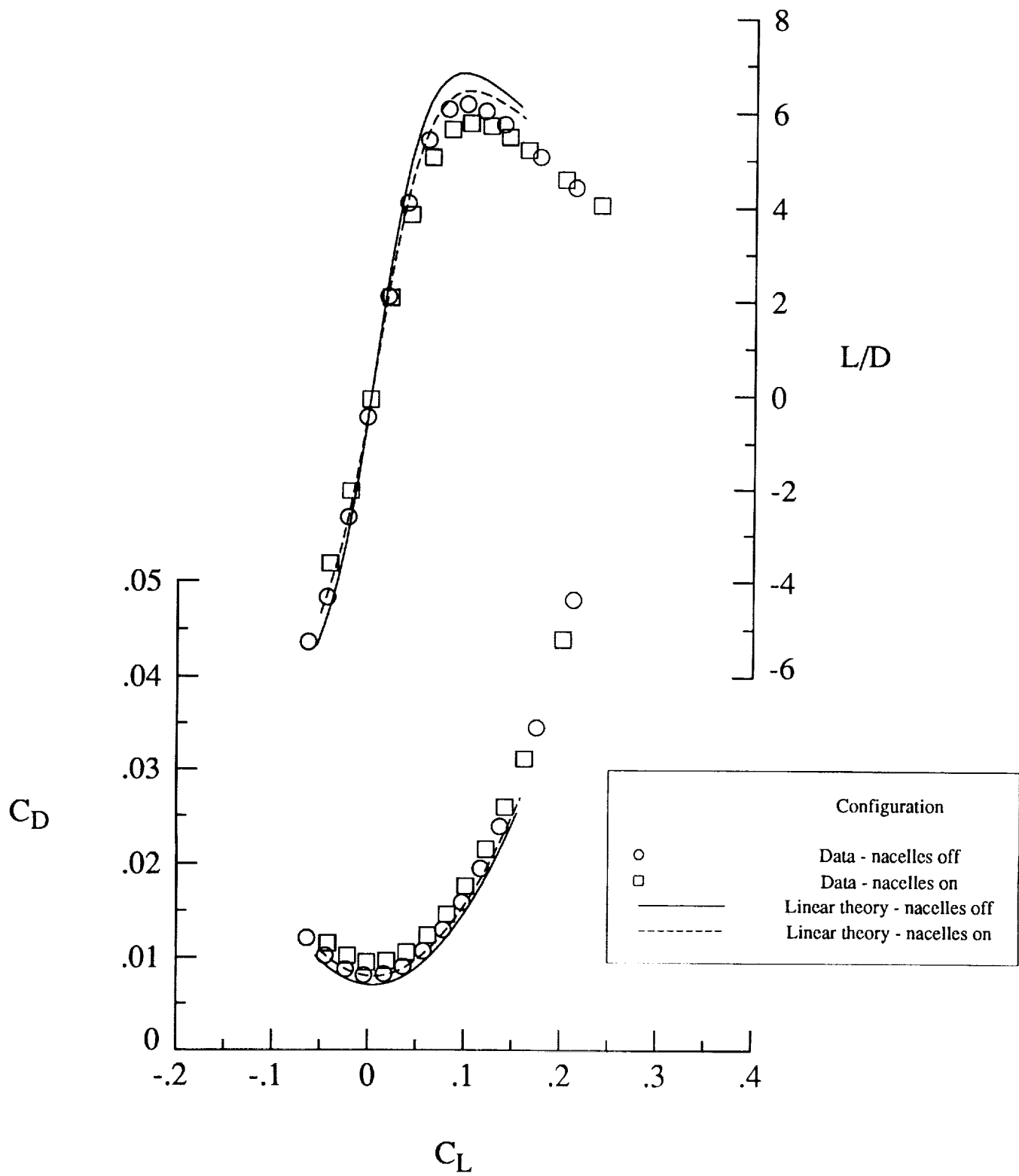
(b) Drag polar and L/D plots.

Figure 10. Concluded.



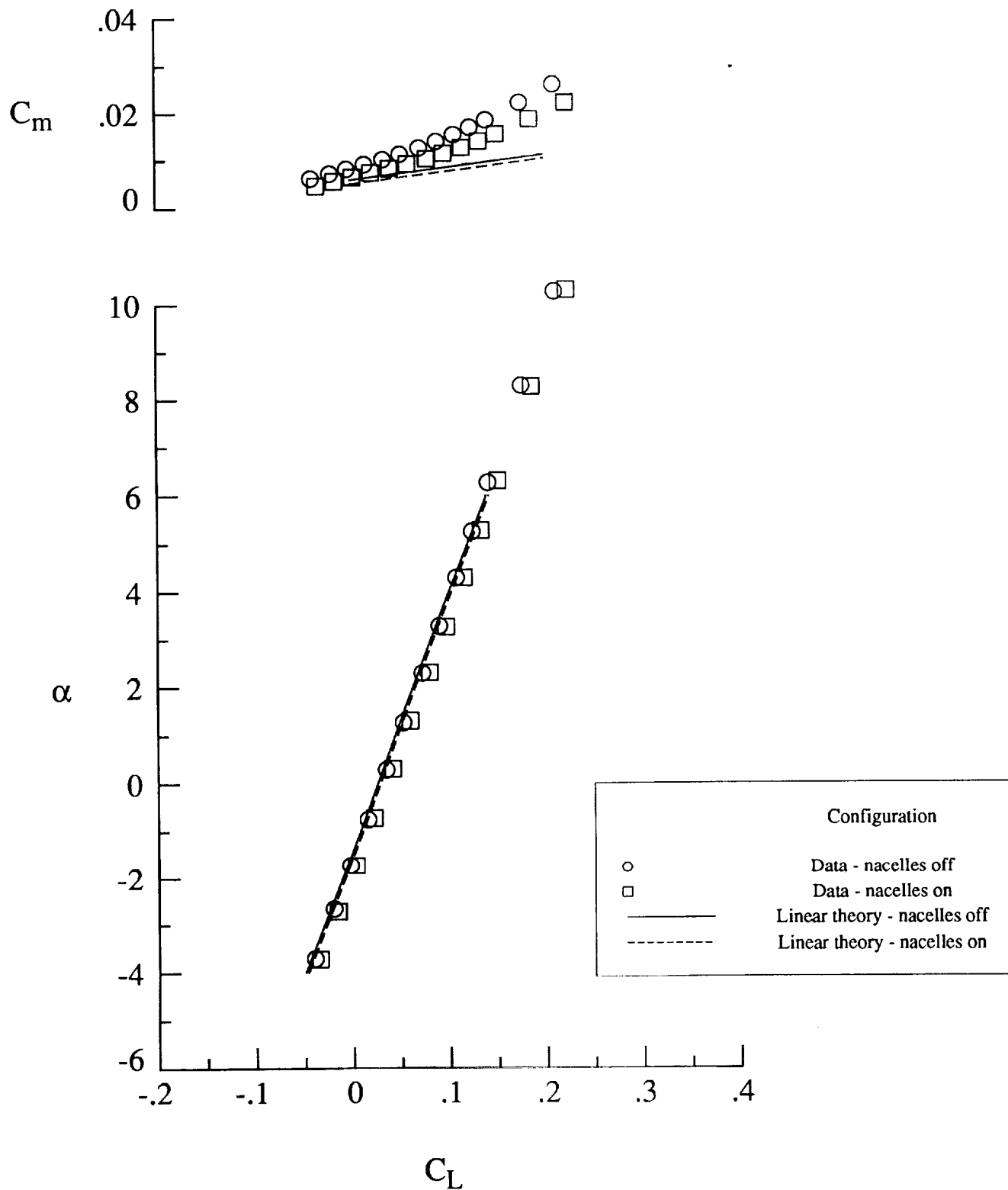
(a) Longitudinal aerodynamic characteristics.

Figure 11. Wind tunnel results and linear theory predictions. $M = 3.2$.



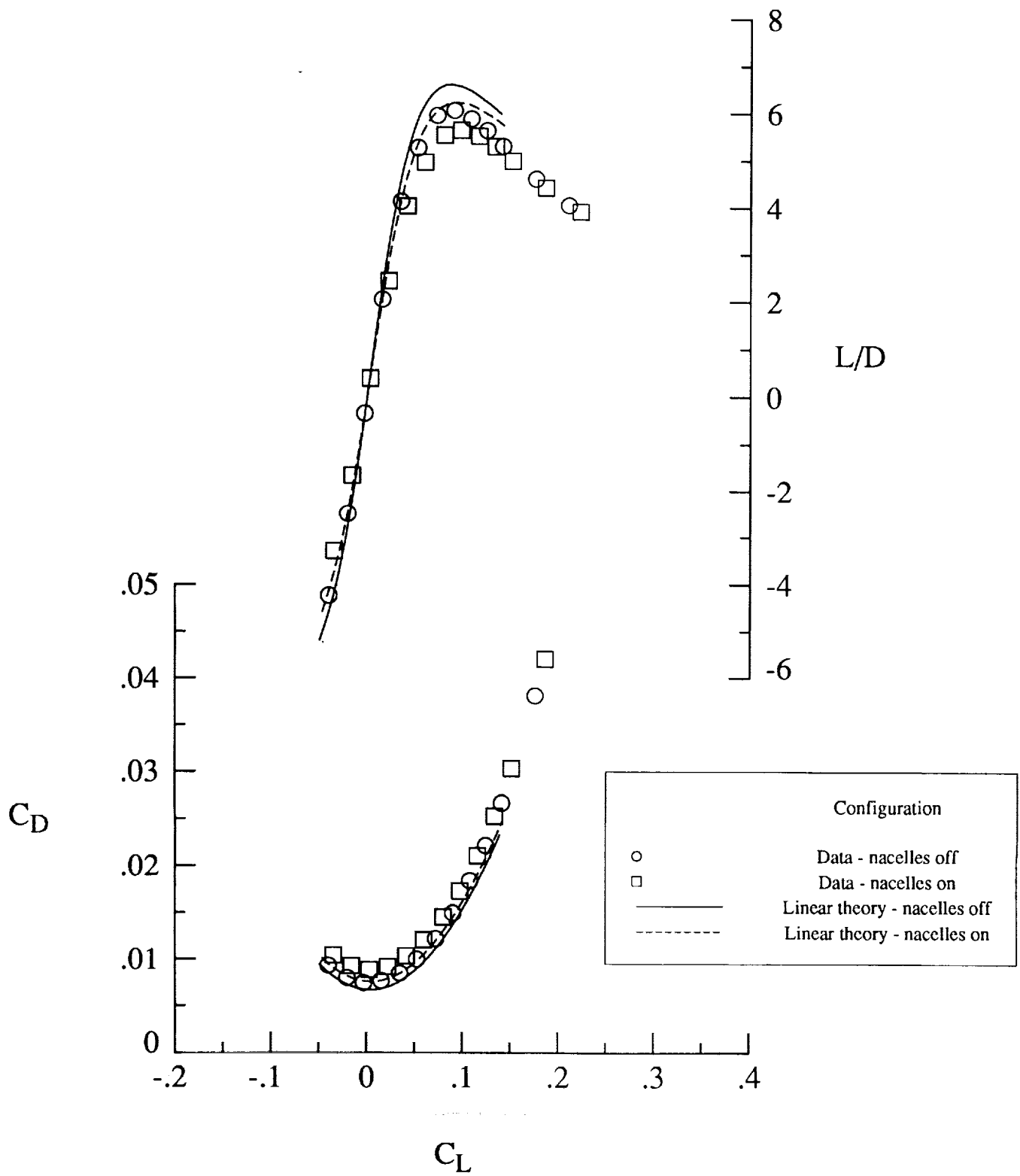
(b) Drag polar and L/D plots.

Figure 11. Concluded.



(a) Longitudinal aerodynamic characteristics.

Figure 12. Wind tunnel results and linear theory predictions. $M = 3.6$.



(b) Drag polar and L/D plots.

Figure 12. Concluded.

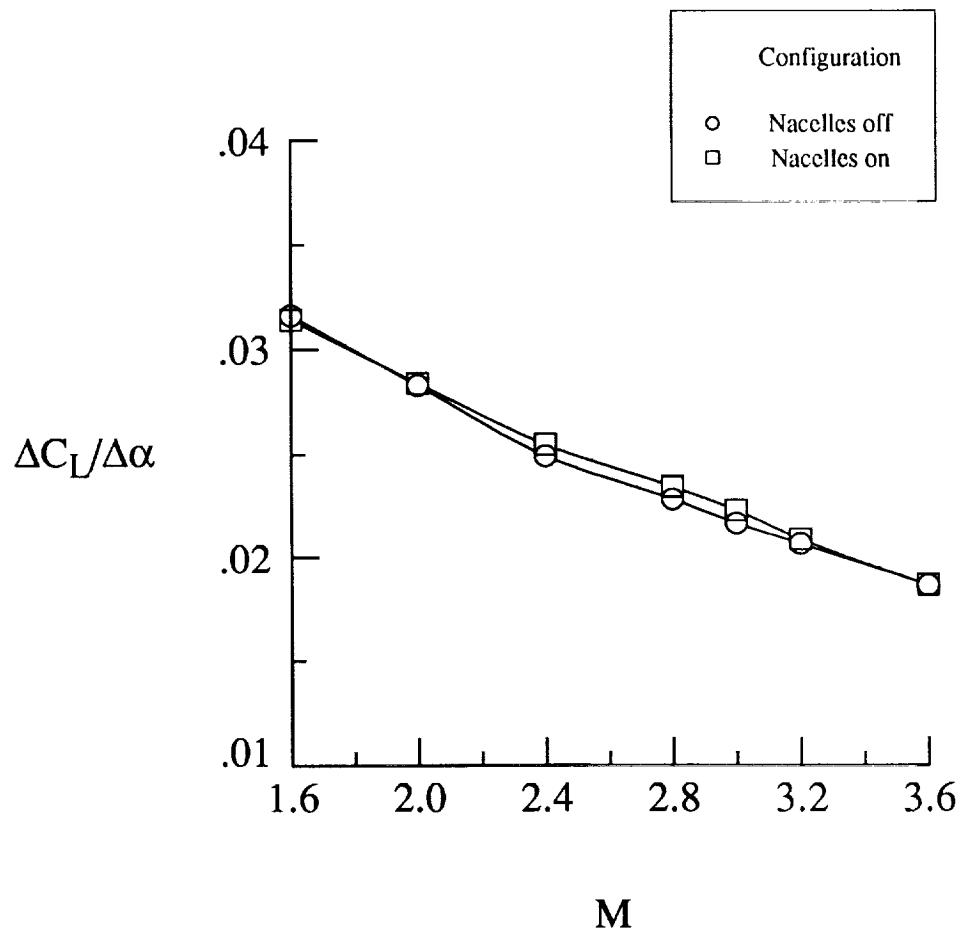


Figure 13. Experimental lift-curve slope at $\alpha = 0$.

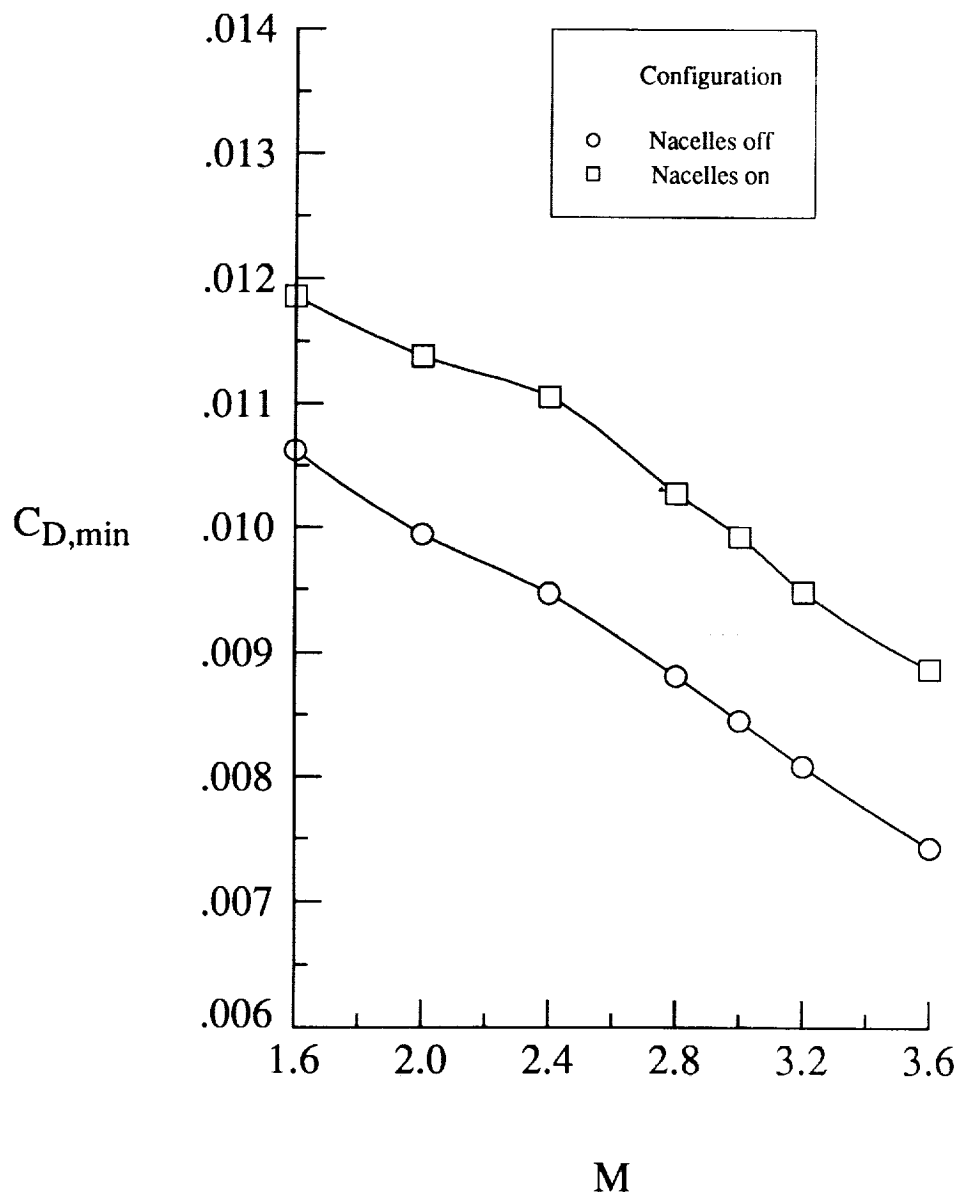


Figure 14. Experimental minimum drag.

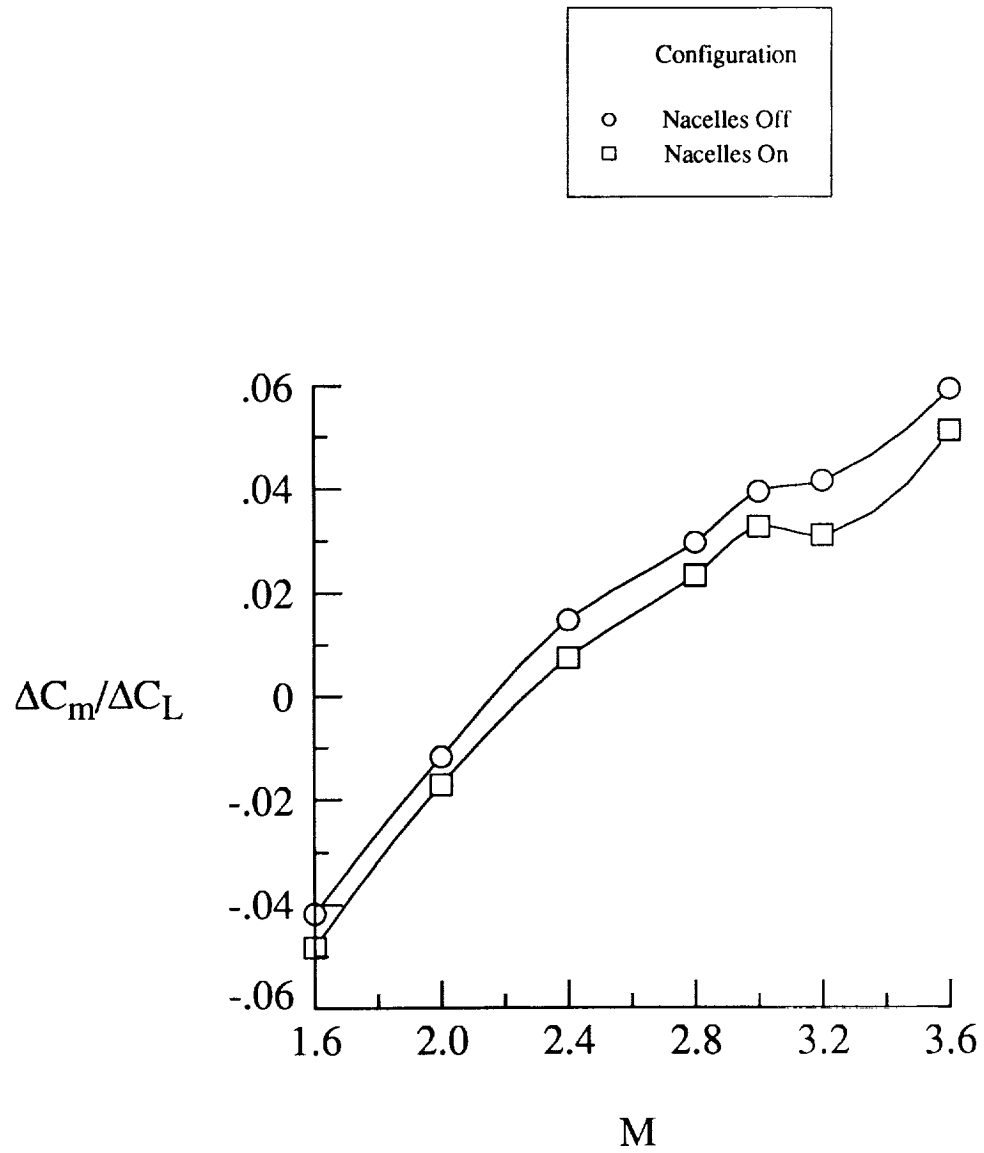


Figure 15. Experimental stability level at $C_L = 0$.

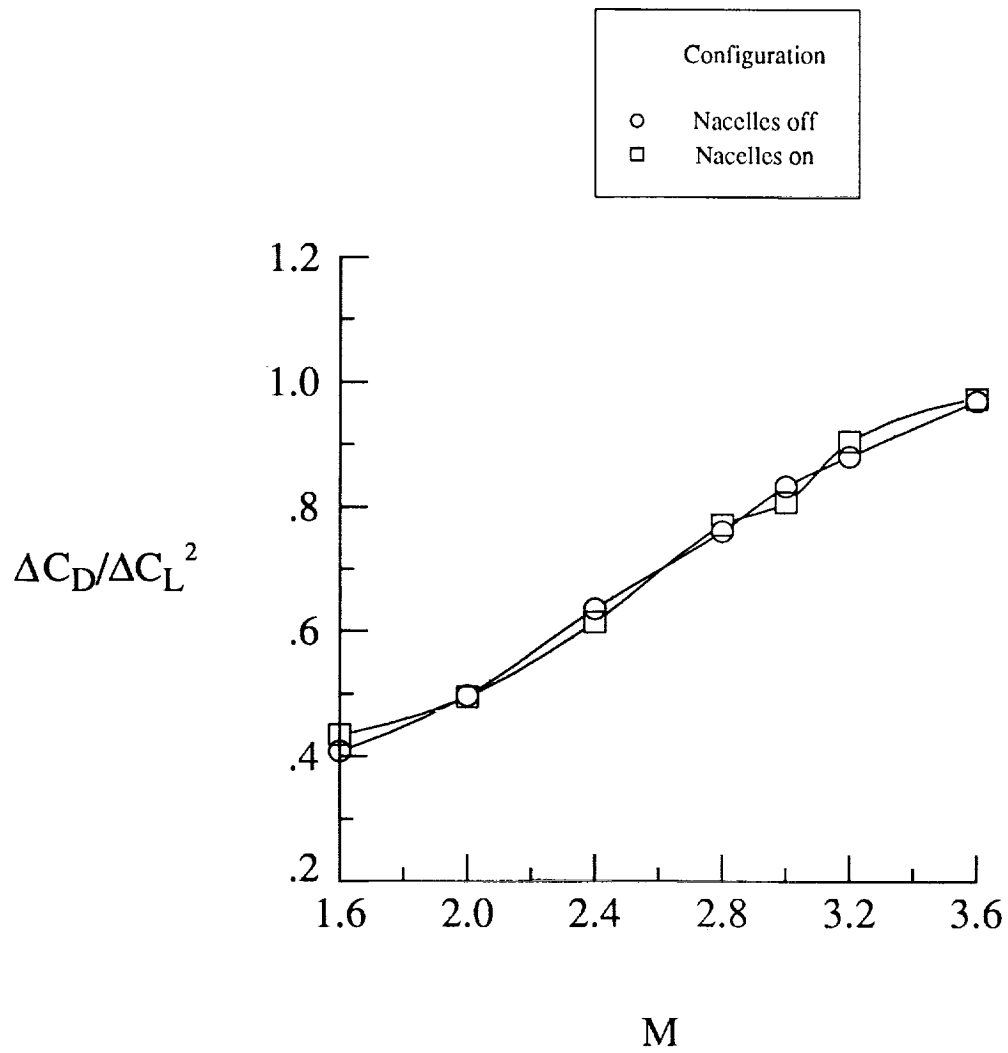


Figure 16. Experimental drag-due-to-lift factor.

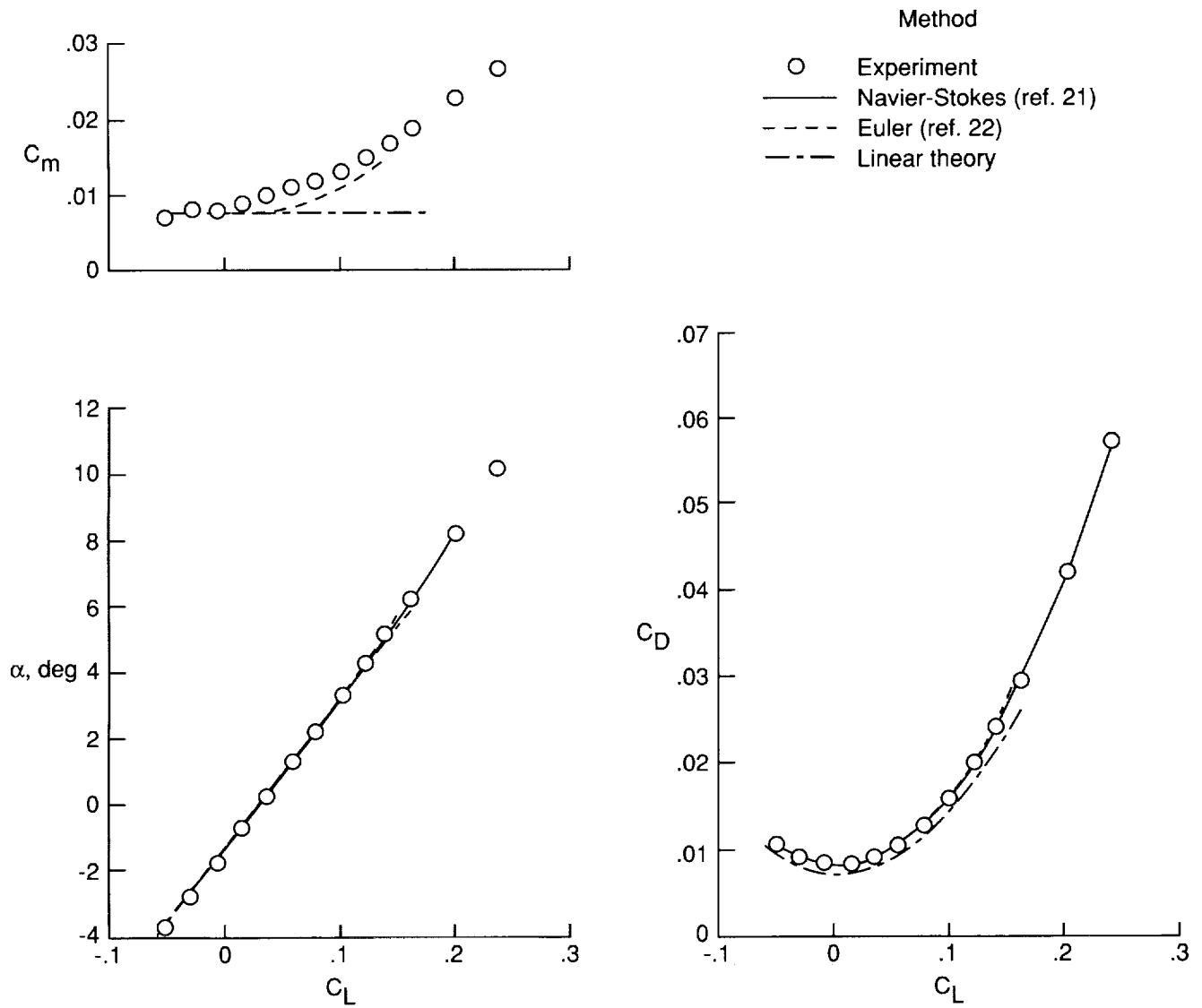


Figure 17. Experimental and theoretical results at $M = 3.0$, nacelles off.

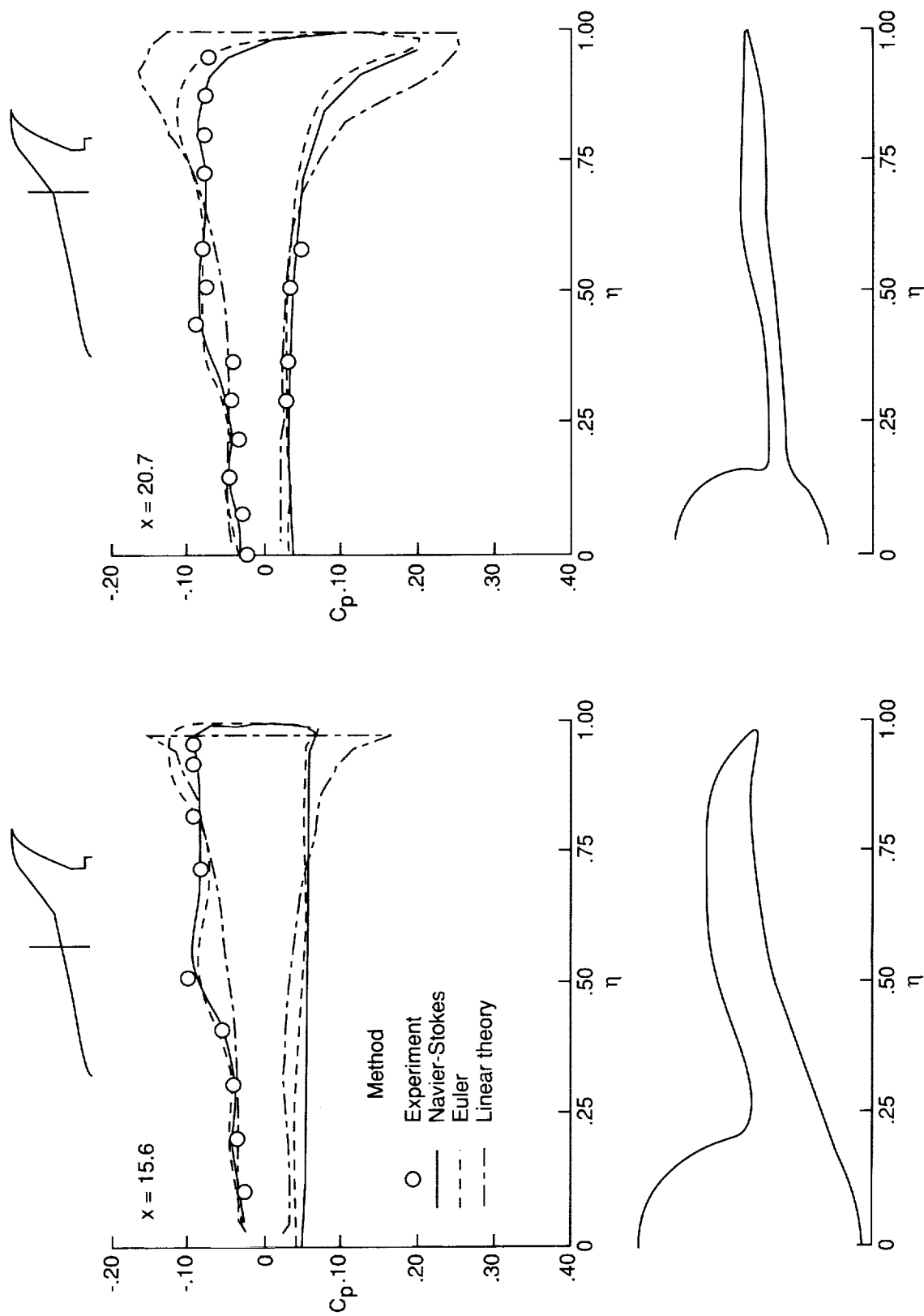


Figure 18. Experimental and theoretical surface pressure distributions with corresponding spanwise cross-sectional cuts. $M = 3.0$; nacelles off; $\alpha = 5^\circ$.

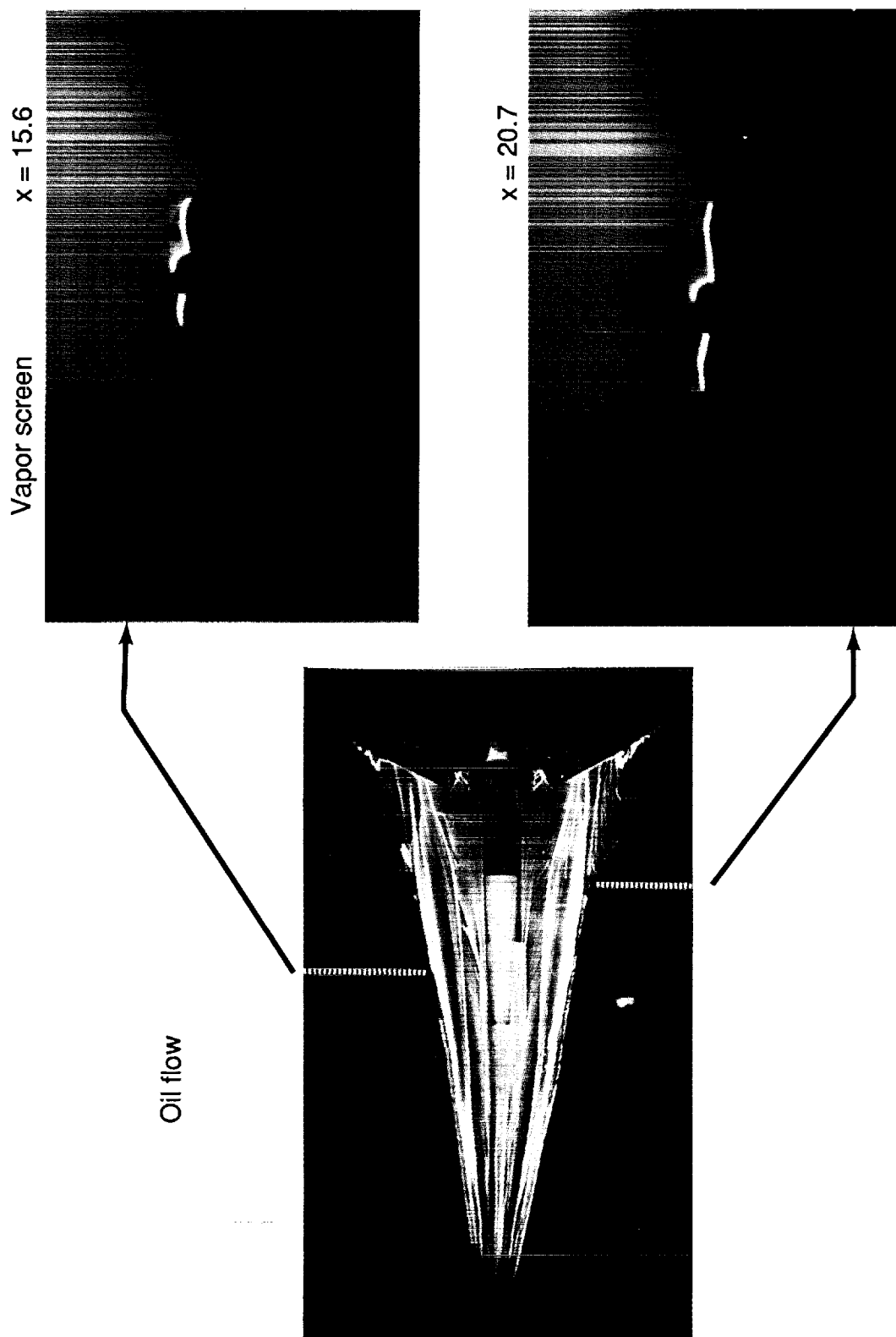
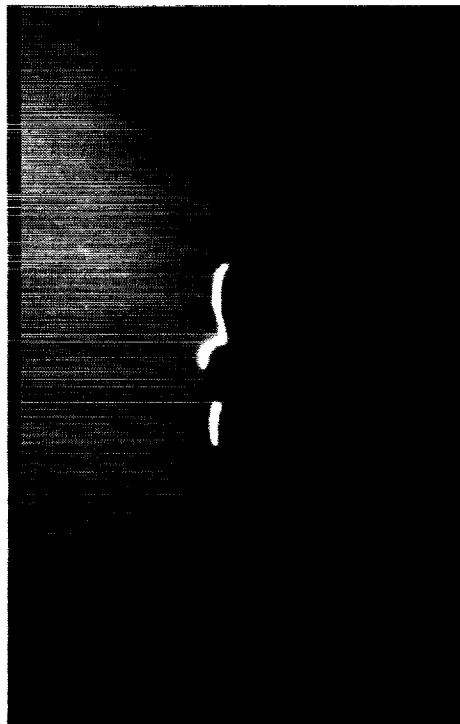


Figure 19. Oil flow and vapor screen photographs. $M = 3.0$; $\alpha = 5^\circ$.

Experiment



Vapor screen

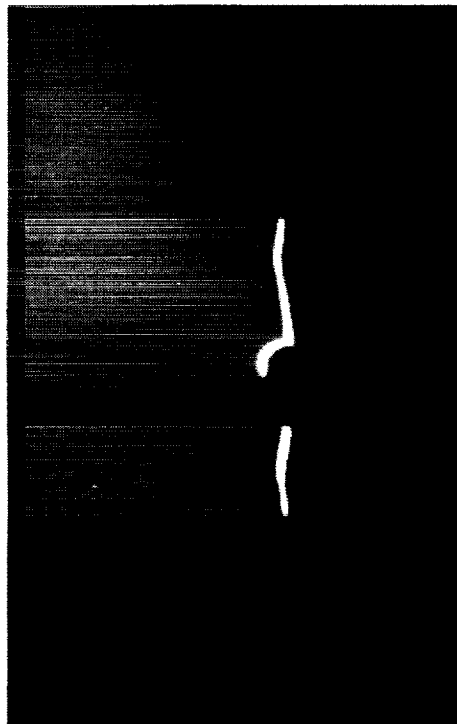
$x = 15.6$

Computation



Density

Experiment



Vapor screen

$x = 20.7$

Computation



Density

Figure 20. Vapor screen photographs compared with CFD vortex system from reference 21.

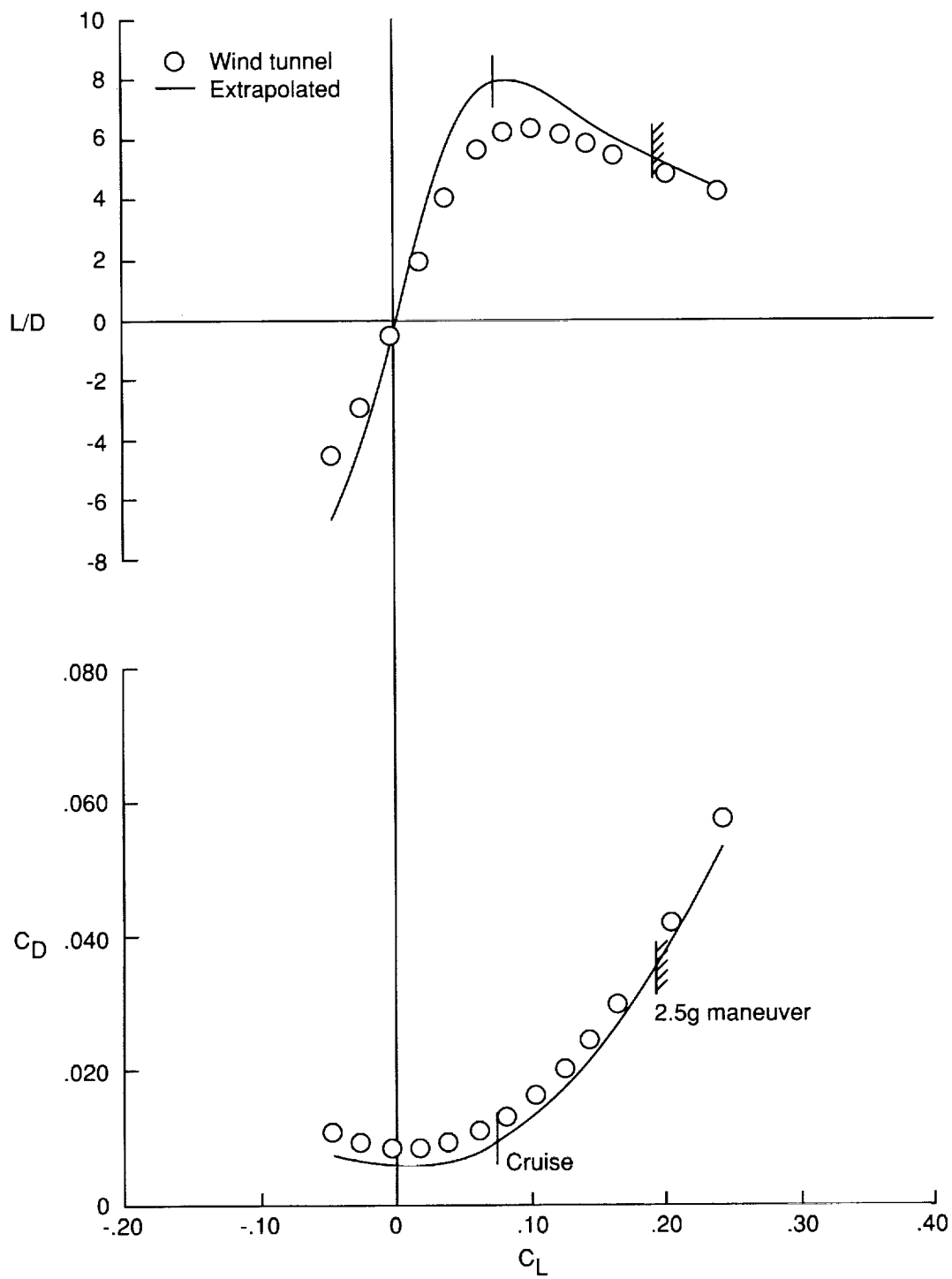


Figure 21. Extrapolation of wind tunnel data to full-scale flight conditions at Mach 3.0 and an altitude of 65 000 ft.

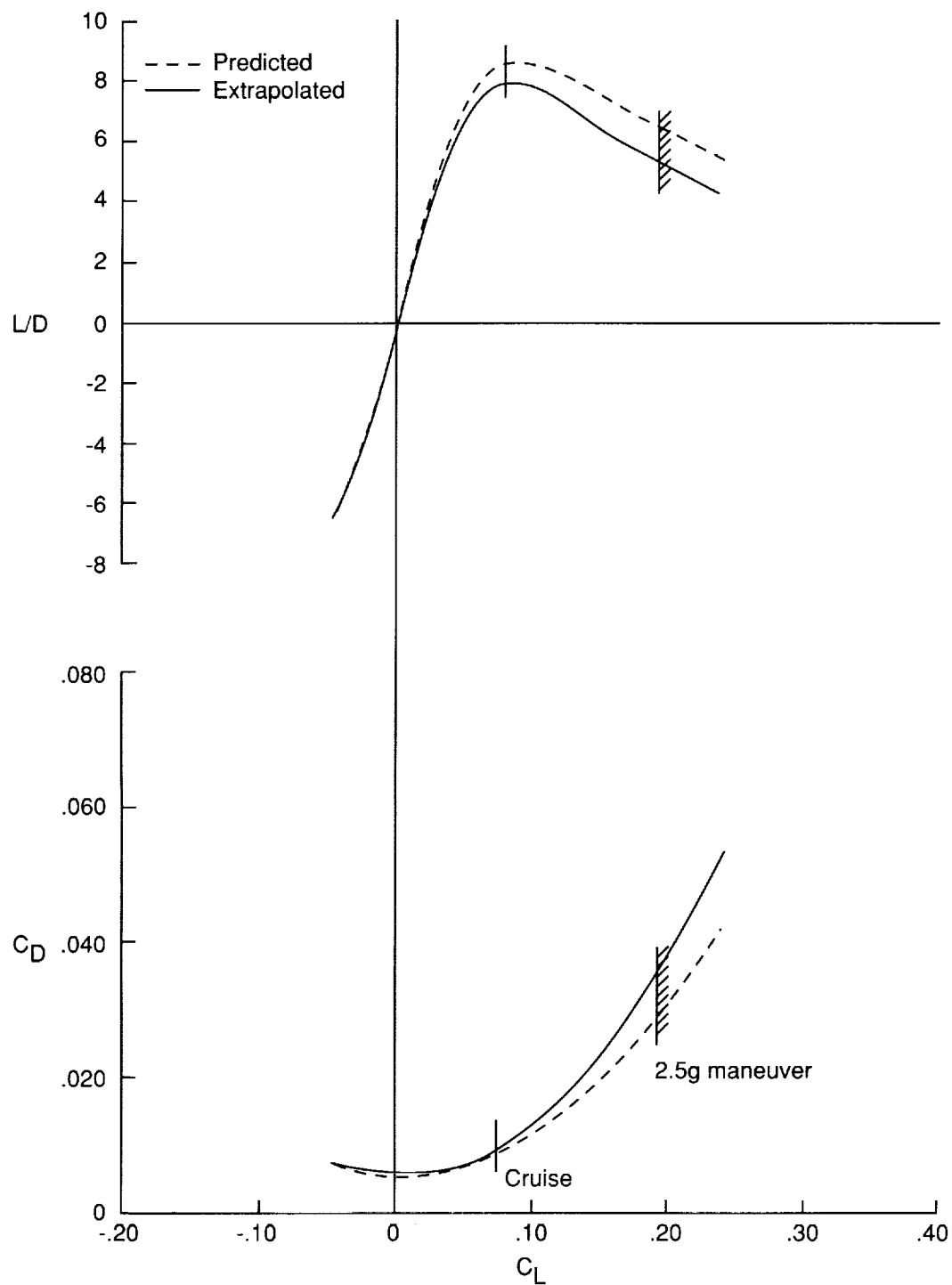


Figure 22. Extrapolated wind tunnel data and predicted aerodynamic characteristics of full-scale configuration at Mach 3.0 and an altitude of 65 000 ft.

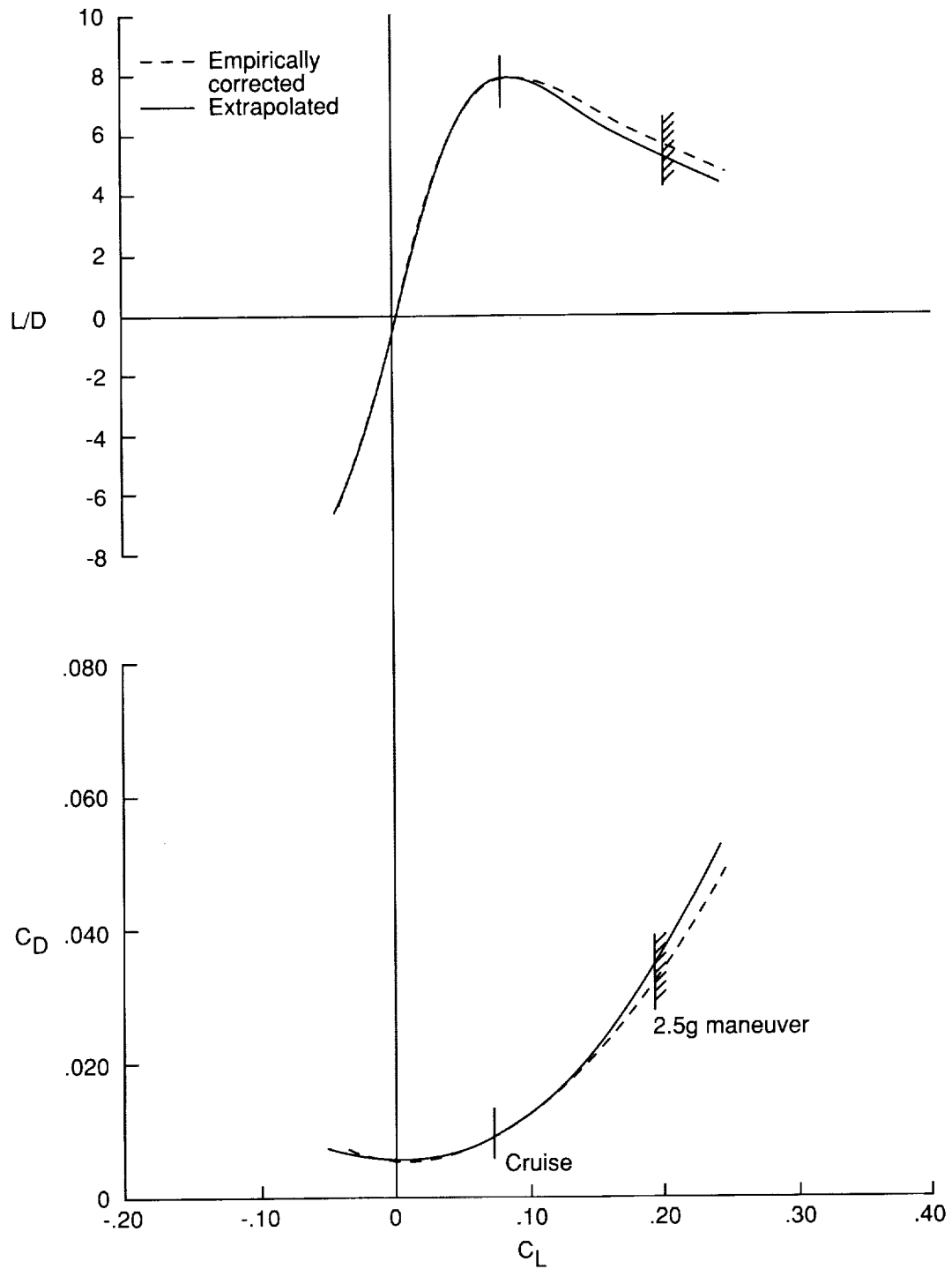


Figure 23. Extrapolated wind tunnel data and empirically corrected predicted aerodynamic characteristics of full-scale configuration at Mach 3.0 and an altitude of 65 000 ft.

Appendix A

Forces and Moments Listing

Table A1. Nacelles Off; $R = 2 \times 10^6$; $S = 1.235 \text{ ft}^2$; $\bar{c} = 15.66 \text{ in.}$

Mach 1.6							
α	C_L	C_D	C_m	L/D	C_N	C_A	$C_{D,c}$
-3.59	-0.0797	0.01345	0.01470	-5.93	-0.0804	0.00844	0.00134
-2.59	-0.0483	0.01158	0.01333	-4.17	-0.0488	0.00939	0.00136
-1.59	-0.0147	0.01073	0.01195	-1.37	-0.0150	0.01032	0.00138
-0.59	0.0159	0.01072	0.01061	1.48	0.0158	0.01088	0.00139
0.45	0.0499	0.01147	0.00919	4.35	0.0500	0.01107	0.00139
1.42	0.0798	0.01302	0.00807	6.13	0.0801	0.01105	0.00139
2.40	0.1121	0.01563	0.00713	7.17	0.1127	0.01093	0.00141
3.54	0.1523	0.02077	0.00787	7.33	0.1532	0.01133	0.00145
4.52	0.1865	0.02684	0.00954	6.95	0.1881	0.01207	0.00148
5.48	0.2180	0.03359	0.01146	6.49	0.2202	0.01262	0.00152
6.43	0.2496	0.04135	0.01397	6.04	0.2526	0.01313	0.00159
8.51	0.3144	0.06158	0.02086	5.11	0.3200	0.01439	0.00172
10.46	0.3750	0.08491	0.02765	4.42	0.3841	0.01541	0.00180

Mach 2.0							
α	C_L	C_D	C_m	L/D	C_N	C_A	$C_{D,c}$
-3.65	-0.0674	0.01264	0.01249	-5.33	-0.0681	0.00832	0.00128
-2.62	-0.0384	0.01086	0.01219	-3.54	-0.0389	0.00909	0.00130
-1.69	-0.0138	0.01007	0.01174	-1.37	-0.0141	0.00966	0.00132
-0.66	0.0155	0.01002	0.01133	1.55	0.0154	0.01020	0.00134
0.39	0.0452	0.01071	0.01104	4.22	0.0452	0.01040	0.00136
1.41	0.0736	0.01225	0.01094	6.01	0.0739	0.01043	0.00138
2.37	0.1003	0.01465	0.01115	6.85	0.1008	0.01049	0.00141
3.36	0.1298	0.01876	0.01250	6.92	0.1306	0.01113	0.00141
4.41	0.1598	0.02423	0.01444	6.59	0.1612	0.01189	0.00142
5.41	0.1881	0.03024	0.01635	6.22	0.1901	0.01237	0.00144
6.35	0.2146	0.03683	0.01842	5.83	0.2174	0.01286	0.00149
8.40	0.2700	0.05384	0.02389	5.02	0.2750	0.01380	0.00159

Mach 2.4							
α	C_L	C_D	C_m	L/D	C_N	C_A	$C_{D,c}$
-3.77	-0.0611	0.01221	0.00833	-5.01	-0.0618	0.00816	0.00100
-2.73	-0.0354	0.01048	0.00881	-3.38	-0.0359	0.00878	0.00099
-1.75	-0.0100	0.00957	0.00910	-1.05	-0.0103	0.00926	0.00099
-0.79	0.0130	0.00958	0.00924	1.36	0.0129	0.00976	0.00099
0.25	0.0390	0.01018	0.00954	3.83	0.0390	0.01001	0.00100
1.26	0.0652	0.01160	0.01009	5.62	0.0654	0.01016	0.00100
2.26	0.0892	0.01390	0.01078	6.41	0.0896	0.01038	0.00101
3.24	0.1153	0.01751	0.01241	6.58	0.1161	0.01097	0.00101
4.24	0.1403	0.02203	0.01417	6.37	0.1416	0.01160	0.00102
5.29	0.1670	0.02770	0.01632	6.03	0.1688	0.01218	0.00104
6.23	0.1895	0.03344	0.01829	5.67	0.1920	0.01268	0.00105
8.25	0.2365	0.04812	0.02287	4.91	0.2409	0.01371	0.00107
10.28	0.2847	0.06671	0.02829	4.27	0.2920	0.01482	0.00110

Table A1. Continued

Mach 2.8

α	C_L	C_D	C_m	L/D	C_N	C_A	$C_{D,c}$
-3.68	-0.0510	0.01110	0.00737	-4.59	-0.0516	0.00781	0.00080
-2.69	-0.0283	0.00958	0.00805	-2.95	-0.0287	0.00824	0.00080
-1.74	-0.0074	0.00894	0.00847	-0.82	-0.0076	0.00871	0.00080
-0.67	0.0177	0.00884	0.00905	2.00	0.0176	0.00904	0.00080
0.29	0.0393	0.00967	0.00962	4.07	0.0394	0.00947	0.00080
1.28	0.0622	0.01117	0.01045	5.57	0.0624	0.00977	0.00080
2.29	0.0847	0.01347	0.01164	6.29	0.0852	0.01007	0.00080
3.29	0.1066	0.01672	0.01308	6.37	0.1073	0.01057	0.00080
4.30	0.1287	0.02081	0.01482	6.19	0.1299	0.01111	0.00081
5.30	0.1507	0.02574	0.01675	5.85	0.1524	0.01171	0.00081
6.30	0.1721	0.03121	0.01866	5.51	0.1745	0.01215	0.00082
8.29	0.2133	0.04441	0.02283	4.80	0.2174	0.01320	0.00083
10.34	0.2553	0.06091	0.02738	4.19	0.2620	0.01411	0.00085

Mach 3.0

α	C_L	C_D	C_m	L/D	C_N	C_A	$C_{D,c}$
-3.73	-0.0490	0.01076	0.00668	-4.55	-0.0496	0.00755	0.00071
-2.74	-0.0274	0.00935	0.00751	-2.93	-0.0278	0.00803	0.00070
-1.72	-0.0044	0.00853	0.00831	-0.52	-0.0047	0.00839	0.00071
-0.72	0.0169	0.00860	0.00902	1.96	0.0168	0.00881	0.00071
0.26	0.0377	0.00936	0.00980	4.03	0.0378	0.00919	0.00071
1.30	0.0612	0.01096	0.01080	5.59	0.0615	0.00957	0.00071
2.24	0.0810	0.01312	0.01199	6.17	0.0814	0.00995	0.00071
3.28	0.1028	0.01629	0.01349	6.31	0.1036	0.01038	0.00071
4.30	0.1241	0.02032	0.01516	6.11	0.1252	0.01097	0.00071
5.26	0.1429	0.02463	0.01678	5.80	0.1446	0.01142	0.00072
6.28	0.1636	0.03002	0.01872	5.45	0.1659	0.01196	0.00072
8.26	0.2031	0.04244	0.02266	4.79	0.2071	0.01281	0.00073
10.23	0.2414	0.05770	0.02682	4.18	0.2478	0.01392	0.00074

Mach 3.2

α	C_L	C_D	C_m	L/D	C_N	C_A	$C_{D,c}$
-4.67	-0.0636	0.01208	0.00577	-5.27	-0.0644	0.00685	0.00061
-3.68	-0.0443	0.01021	0.00678	-4.34	-0.0448	0.00734	0.00061
-2.65	-0.0230	0.00878	0.00765	-2.62	-0.0234	0.00771	0.00061
-1.68	-0.0038	0.00814	0.00826	-0.47	-0.0040	0.00802	0.00062
-0.64	0.0171	0.00826	0.00898	2.08	0.0170	0.00845	0.00062
0.32	0.0369	0.00906	0.00969	4.07	0.0370	0.00886	0.00062
1.30	0.0579	0.01071	0.01061	5.40	0.0581	0.00939	0.00062
2.34	0.0785	0.01296	0.01164	6.05	0.0790	0.00975	0.00062
3.33	0.0980	0.01591	0.01291	6.16	0.0987	0.01019	0.00062
4.31	0.1173	0.01951	0.01431	6.01	0.1185	0.01063	0.00062
5.34	0.1371	0.02389	0.01572	5.74	0.1387	0.01102	0.00062
7.33	0.1746	0.03457	0.01885	5.05	0.1776	0.01202	0.00063
9.30	0.2121	0.04810	0.02248	4.41	0.2171	0.01317	0.00063

Table A1. Concluded

Mach 3.6

α	C_L	C_D	C_m	L/D	C_N	C_A	$C_{D,c}$
-3.70	-0.0395	0.00935	0.00621	-4.23	-0.0401	0.00677	0.00049
-2.66	-0.0200	0.00801	0.00724	-2.50	-0.0204	0.00708	0.00049
-1.72	-0.0026	0.00745	0.00815	-0.35	-0.0028	0.00737	0.00049
-0.75	0.0157	0.00767	0.00915	2.05	0.0156	0.00787	0.00049
0.30	0.0351	0.00849	0.01023	4.13	0.0351	0.00831	0.00049
1.27	0.0527	0.01000	0.01132	5.27	0.0529	0.00883	0.00050
2.30	0.0725	0.01219	0.01267	5.95	0.0729	0.00927	0.00050
3.29	0.0904	0.01492	0.01403	6.06	0.0911	0.00971	0.00050
4.30	0.1081	0.01838	0.01551	5.88	0.1092	0.01022	0.00050
5.26	0.1247	0.02215	0.01699	5.63	0.1262	0.01062	0.00050
6.26	0.1412	0.02665	0.01856	5.30	0.1433	0.01109	0.00050
8.29	0.1759	0.03812	0.02225	4.61	0.1796	0.01235	0.00049
10.28	0.2103	0.05190	0.02609	4.05	0.2162	0.01353	0.00049

Table A2. Nacelles On; $R = 2 \times 10^6$; $S = 1.235 \text{ ft}^2$; $\bar{c} = 15.66 \text{ in.}$

Mach 1.6

α	C_L	C_D	C_m	L/D	C_N	C_A	$C_{D,c}$
-3.80	-0.0718	0.01462	0.01087	-4.91	-0.0729	0.00973	0.00152
-2.72	-0.0373	0.01268	0.00928	-2.94	-0.0380	0.01083	0.00158
-1.71	-0.0030	0.01190	0.00762	-0.25	-0.0035	0.01177	0.00164
-0.79	0.0258	0.01205	0.00617	2.15	0.0256	0.01239	0.00167
0.21	0.0563	0.01296	0.00453	4.34	0.0563	0.01276	0.00171
1.29	0.0915	0.01494	0.00313	6.12	0.0919	0.01290	0.00175
2.30	0.1259	0.01795	0.00228	7.01	0.1267	0.01291	0.00180
3.22	0.1547	0.02183	0.00213	7.09	0.1559	0.01316	0.00185
4.26	0.1932	0.02841	0.00398	6.80	0.1952	0.01407	0.00189
5.23	0.2257	0.03537	0.00565	6.38	0.2284	0.01478	0.00195
6.31	0.2634	0.04458	0.00823	5.91	0.2672	0.01556	0.00201

Mach 2.0

α	C_L	C_D	C_m	L/D	C_N	C_A	$C_{D,c}$
-3.61	-0.0545	0.01345	0.00845	-4.05	-0.0555	0.00995	0.00133
-2.67	-0.0277	0.01202	0.00821	-2.30	-0.0284	0.01070	0.00136
-1.68	-0.0005	0.01141	0.00761	-0.04	-0.0009	0.01138	0.00139
-0.67	0.0277	0.01160	0.00706	2.39	0.0275	0.01193	0.00143
0.44	0.0594	0.01274	0.00650	4.66	0.0595	0.01230	0.00147
1.40	0.0868	0.01453	0.00619	5.97	0.0873	0.01244	0.00152
2.33	0.1138	0.01709	0.00627	6.66	0.1146	0.01249	0.00156
3.38	0.1446	0.02167	0.00749	6.67	0.1458	0.01318	0.00158
4.42	0.1751	0.02752	0.00927	6.36	0.1770	0.01406	0.00161
5.41	0.2030	0.03383	0.01117	6.00	0.2057	0.01473	0.00163
6.40	0.2328	0.04134	0.01339	5.63	0.2363	0.01540	0.00167
8.37	0.2855	0.05848	0.01853	4.88	0.2916	0.01670	0.00174

Mach 2.4

α	C_L	C_D	C_m	L/D	C_N	C_A	$C_{D,c}$
-3.72	-0.0515	0.01321	0.00578	-3.90	-0.0525	0.00979	0.00106
-2.76	-0.0275	0.01176	0.00611	-2.34	-0.0281	0.01039	0.00107
-1.78	-0.0025	0.01110	0.00626	-0.22	-0.0029	0.01100	0.00107
-0.77	0.0233	0.01124	0.00638	2.07	0.0231	0.01154	0.00107
0.28	0.0500	0.01216	0.00655	4.11	0.0501	0.01192	0.00107
1.28	0.0763	0.01388	0.00683	5.50	0.0767	0.01218	0.00108
2.27	0.1005	0.01644	0.00750	6.11	0.1011	0.01250	0.00109
3.28	0.1270	0.02036	0.00892	6.23	0.1281	0.01314	0.00109
4.22	0.1519	0.02507	0.01062	6.06	0.1536	0.01392	0.00110
5.27	0.1775	0.03089	0.01236	5.74	0.1798	0.01463	0.00111
6.28	0.2030	0.03747	0.01444	5.42	0.2062	0.01527	0.00112
8.27	0.2507	0.05278	0.01865	4.75	0.2562	0.01659	0.00113
10.28	0.2982	0.07159	0.02331	4.16	0.3068	0.01789	0.00116

Table A2. Continued

Mach 2.8

α	C_L	C_D	C_m	L/D	C_N	C_A	$C_{D,c}$
-3.72	-0.0442	0.01223	0.00531	-3.61	-0.0450	0.00930	0.00081
-2.70	-0.0220	0.01092	0.00585	-2.02	-0.0226	0.00985	0.00082
-1.65	0.0034	0.01029	0.00635	0.33	0.0030	0.01038	0.00082
-0.68	0.0259	0.01056	0.00663	2.45	0.0257	0.01087	0.00082
0.36	0.0504	0.01168	0.00712	4.31	0.0505	0.01138	0.00082
1.35	0.0736	0.01352	0.00788	5.44	0.0740	0.01182	0.00082
2.36	0.0955	0.01613	0.00880	5.92	0.0962	0.01224	0.00082
3.32	0.1171	0.01949	0.01006	6.01	0.1182	0.01276	0.00083
4.33	0.1398	0.02397	0.01164	5.83	0.1414	0.01347	0.00083
5.35	0.1619	0.02909	0.01333	5.57	0.1641	0.01406	0.00083
6.31	0.1830	0.03483	0.01503	5.25	0.1860	0.01477	0.00083
8.33	0.2263	0.04892	0.01886	4.63	0.2314	0.01610	0.00084
10.32	0.2683	0.06577	0.02290	4.08	0.2762	0.01740	0.00086

Mach 3.0

α	C_L	C_D	C_m	L/D	C_N	C_A	$C_{D,c}$
-3.73	-0.0419	0.01190	0.00480	-3.52	-0.0427	0.00911	0.00072
-2.68	-0.0190	0.01057	0.00555	-1.79	-0.0195	0.00965	0.00072
-1.76	0.0016	0.00995	0.00623	0.16	0.0012	0.00998	0.00072
-0.77	0.0237	0.01022	0.00677	2.32	0.0236	0.01054	0.00073
0.28	0.0470	0.01125	0.00735	4.18	0.0471	0.01103	0.00072
1.31	0.0702	0.01317	0.00827	5.33	0.0705	0.01158	0.00072
2.34	0.0922	0.01573	0.00941	5.86	0.0928	0.01201	0.00073
3.29	0.1122	0.01891	0.01061	5.93	0.1133	0.01253	0.00072
4.28	0.1332	0.02312	0.01203	5.76	0.1347	0.01325	0.00072
5.23	0.1527	0.02767	0.01350	5.52	0.1548	0.01383	0.00073
6.22	0.1729	0.03313	0.01514	5.22	0.1757	0.01449	0.00072
8.28	0.2157	0.04689	0.01883	4.60	0.2206	0.01580	0.00072
10.28	0.2555	0.06311	0.02262	4.05	0.2632	0.01728	0.00073

Mach 3.2

α	C_L	C_D	C_m	L/D	C_N	C_A	$C_{D,c}$
-3.88	-0.0417	0.01151	0.00483	-3.62	-0.0425	0.00863	0.00062
-2.89	-0.0210	0.01025	0.00559	-2.05	-0.0216	0.00916	0.00062
-1.89	-0.0010	0.00953	0.00628	-0.10	-0.0013	0.00949	0.00062
-0.90	0.0198	0.00966	0.00679	2.05	0.0196	0.00997	0.00063
0.09	0.0406	0.01058	0.00732	3.83	0.0406	0.01053	0.00062
1.12	0.0622	0.01237	0.00804	5.03	0.0625	0.01117	0.00062
2.10	0.0823	0.01462	0.00884	5.63	0.0828	0.01164	0.00062
3.11	0.1017	0.01765	0.00981	5.76	0.1026	0.01219	0.00062
4.10	0.1227	0.02151	0.01106	5.71	0.1241	0.01282	0.00063
5.12	0.1422	0.02597	0.01221	5.47	0.1441	0.01340	0.00063
6.12	0.1622	0.03120	0.01354	5.20	0.1648	0.01401	0.00061
8.14	0.2016	0.04398	0.01656	4.58	0.2061	0.01546	0.00061
10.13	0.2393	0.05915	0.01997	4.04	0.2464	0.01696	0.00063

Table A2. Concluded

Mach 3.6

α	C_L	C_D	C_m	L/D	C_N	C_A	$C_{D,c}$
-3.72	-0.0343	0.01041	0.00468	-3.30	-0.0350	0.00813	0.00045
-2.72	-0.0155	0.00928	0.00558	-1.67	-0.0159	0.00851	0.00045
-1.73	0.0034	0.00887	0.00652	0.39	0.0031	0.00896	0.00045
-0.71	0.0225	0.00920	0.00740	2.44	0.0223	0.00948	0.00046
0.32	0.0417	0.01033	0.00832	4.03	0.0418	0.01012	0.00046
1.30	0.0599	0.01207	0.00928	4.96	0.0602	0.01073	0.00046
2.31	0.0803	0.01450	0.01040	5.53	0.0808	0.01131	0.00046
3.28	0.0975	0.01728	0.01153	5.64	0.0984	0.01177	0.00046
4.30	0.1163	0.02107	0.01280	5.52	0.1177	0.01244	0.00046
5.28	0.1337	0.02526	0.01411	5.29	0.1356	0.01306	0.00046
6.30	0.1513	0.03031	0.01564	4.99	0.1539	0.01382	0.00045
8.27	0.1860	0.04202	0.01873	4.42	0.1904	0.01537	0.00046
10.31	0.2228	0.05695	0.02224	3.91	0.2298	0.01702	0.00047

Appendix B

Vapor Screen Photographs

Vapor screen photographs are shown for—

$M = 1.6, \alpha = 5^\circ$ at the following x locations:

- $x = 15.6$ without nacelles
- 20.7 without nacelles
- 29.5 without nacelles
- 29.5 with nacelles

$M = 3.0, \alpha = 1^\circ, 3^\circ$, and 5° at the following x locations:

- $x = 15.6$ without nacelles
- 20.7 without nacelles
- 29.5 without nacelles
- 29.5 with nacelles

$M = 3.0, \alpha = 8^\circ$, and 10° at the following x locations:

- $x = 20.7$ without nacelles
- 23.0 without nacelles
- 29.5 without nacelles
- 29.5 with nacelles

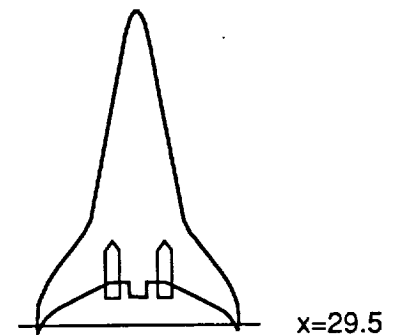
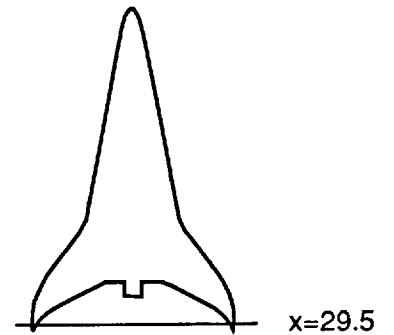
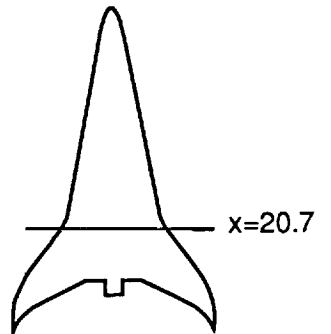
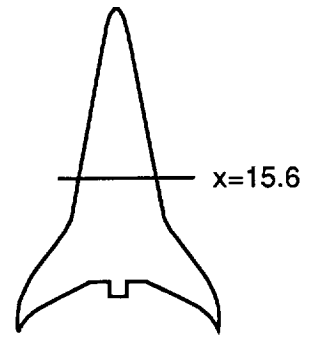


Figure B1. Vapor screen photographs. Mach 1.6; $\alpha = 5^\circ$.

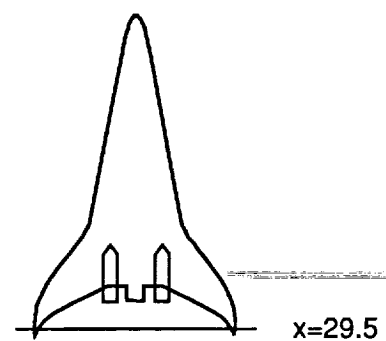
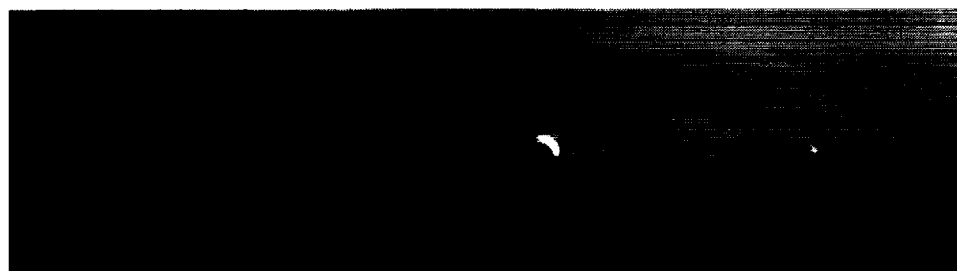
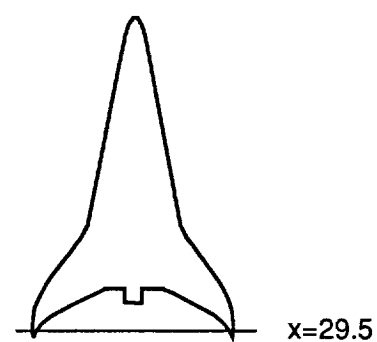
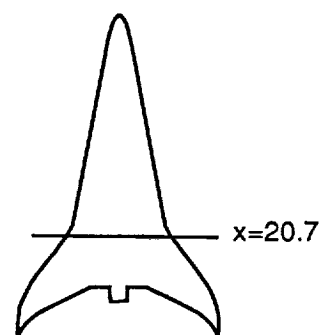
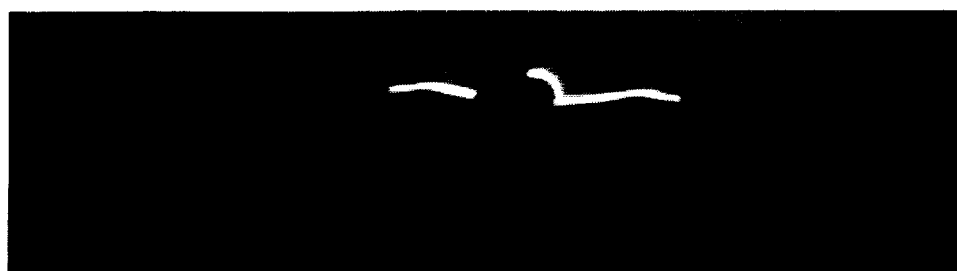
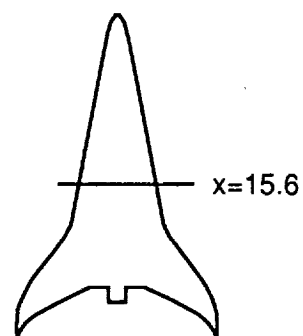


Figure B2. Vapor screen photographs. Mach 3.0; $\alpha = 1^\circ$.

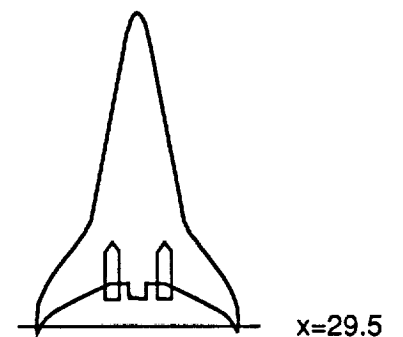
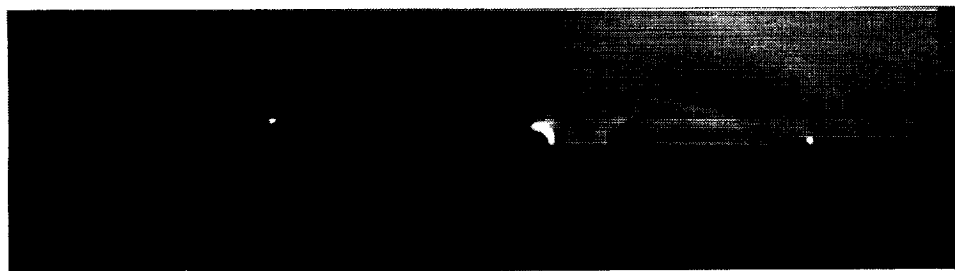
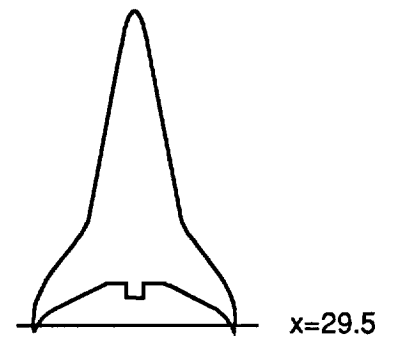
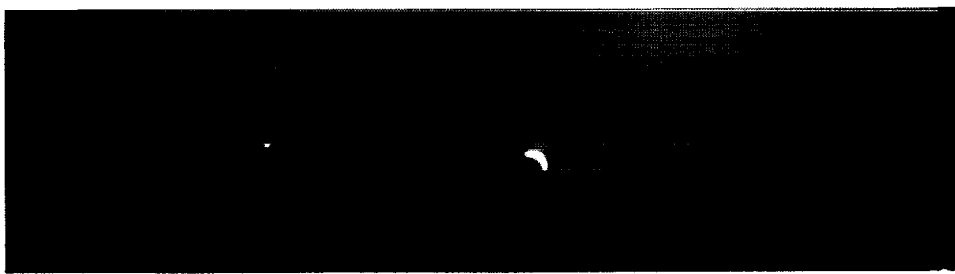
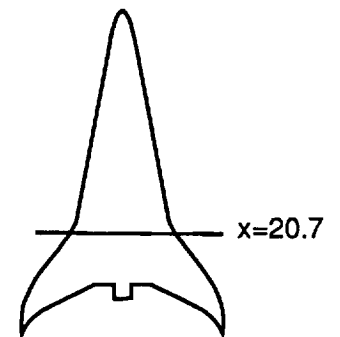
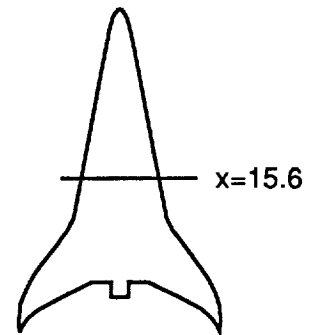


Figure B3. Vapor screen photographs. Mach 3.0; $\alpha = 3^\circ$.

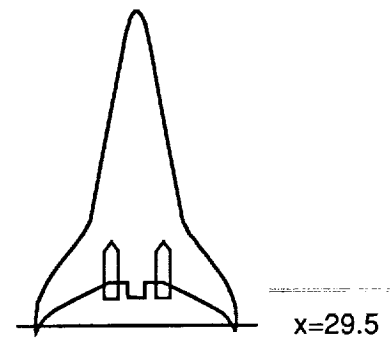
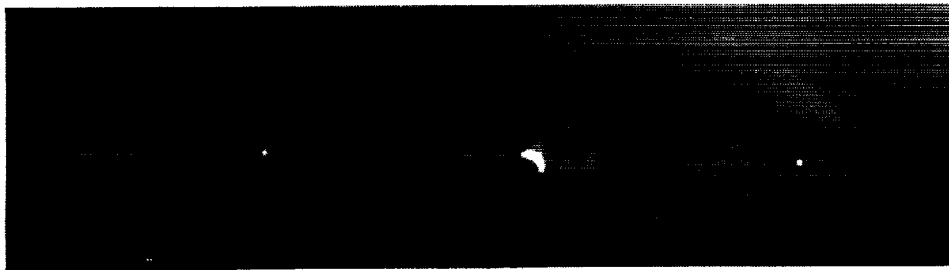
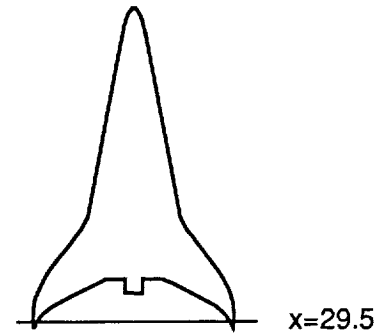
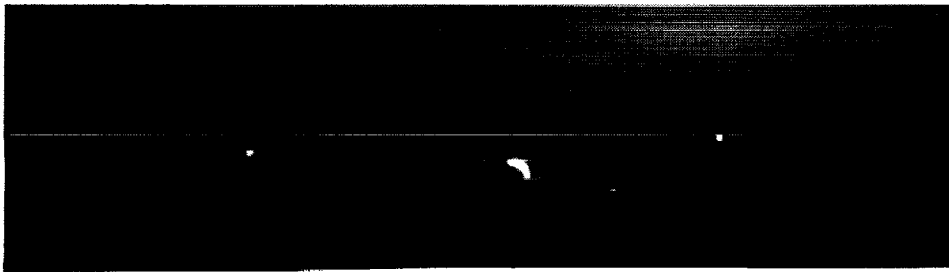
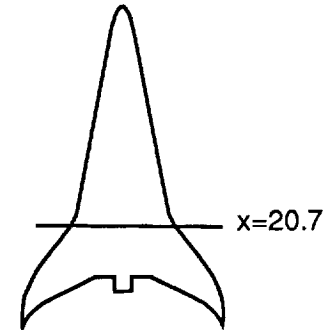
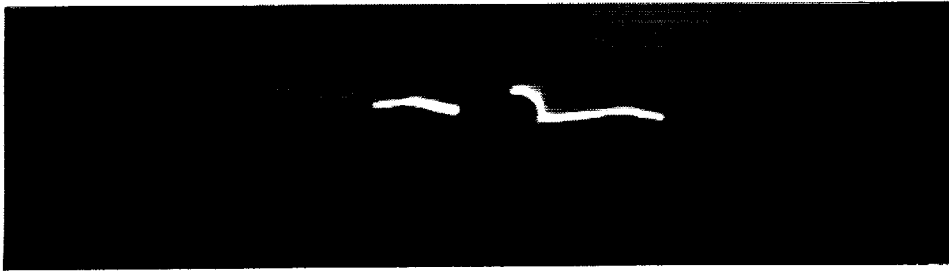
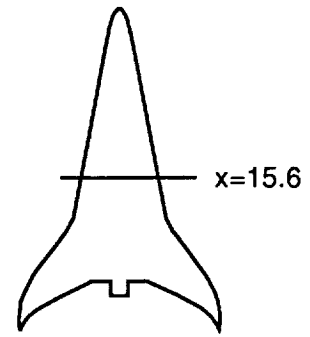
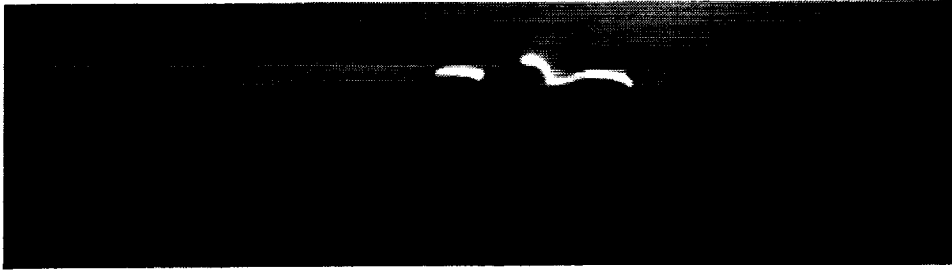


Figure B4. Vapor screen photographs. Mach 3.0; $\alpha = 5^\circ$.

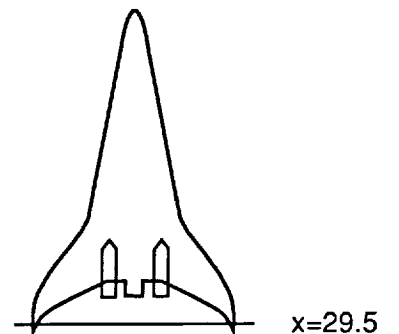
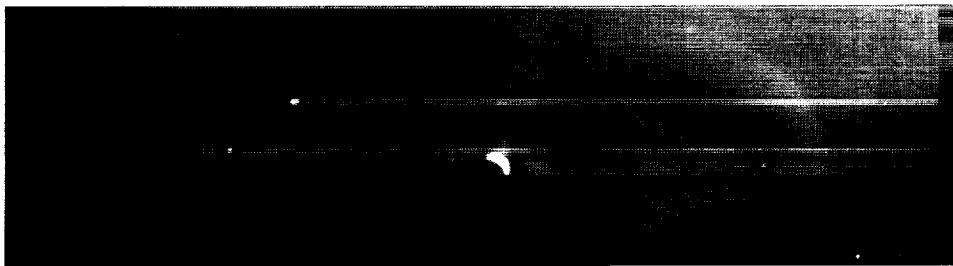
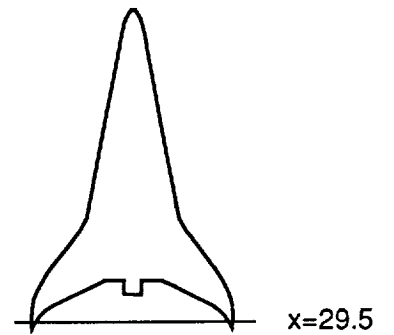
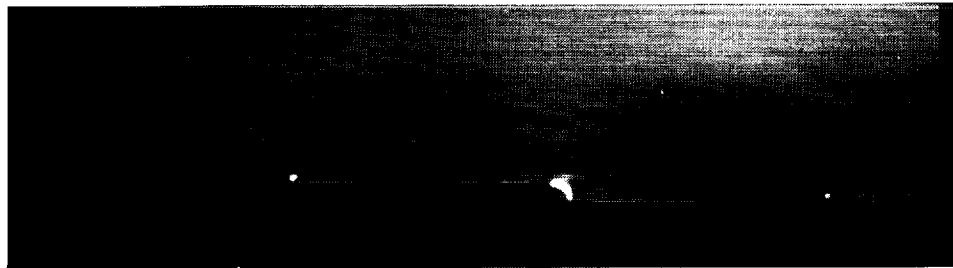
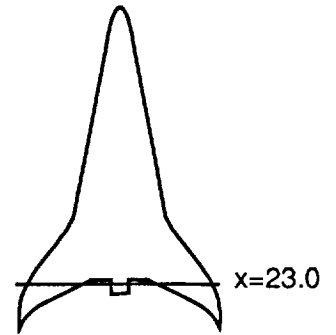
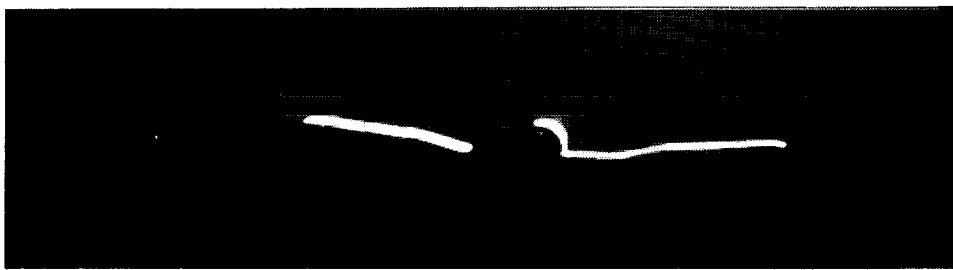
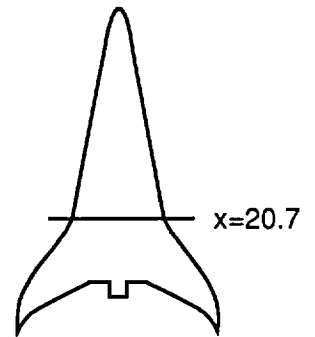


Figure B5. Vapor screen photographs. Mach 3.0; $\alpha = 8^\circ$.

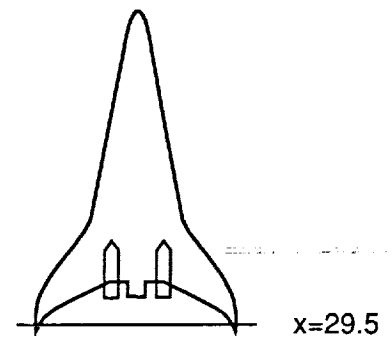
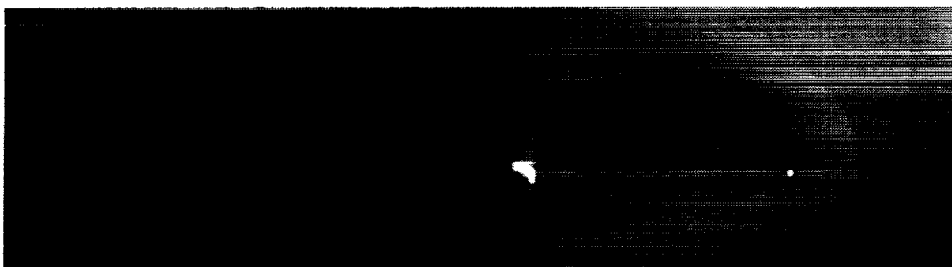
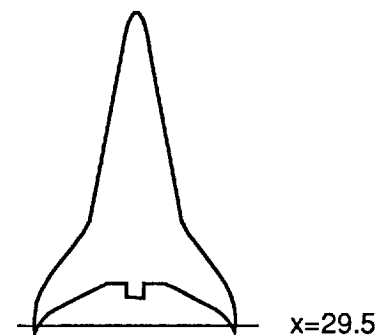
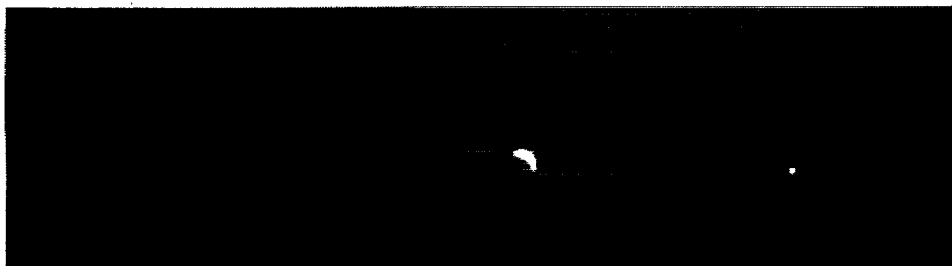
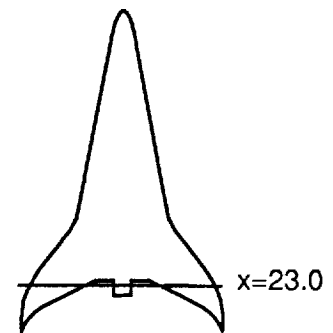
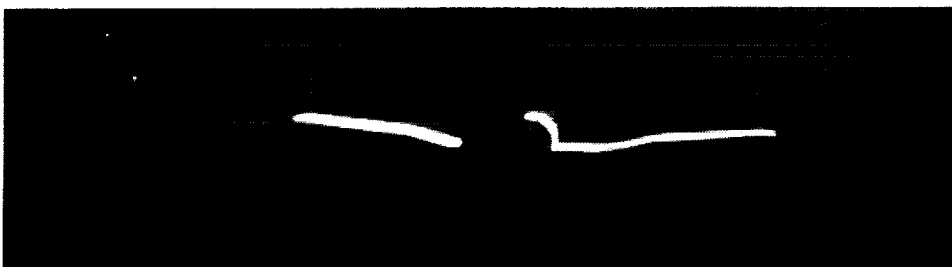
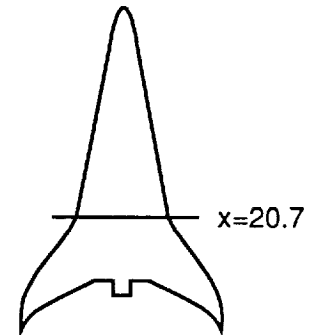


Figure B6. Vapor screen photographs. Mach 3.0; $\alpha = 10^\circ$.

Appendix C

Oil Flow Photographs

Oil flow photographs are shown at the following conditions—

$M = 1.6$ and $M = 3.0$

Top view

Nacelles off

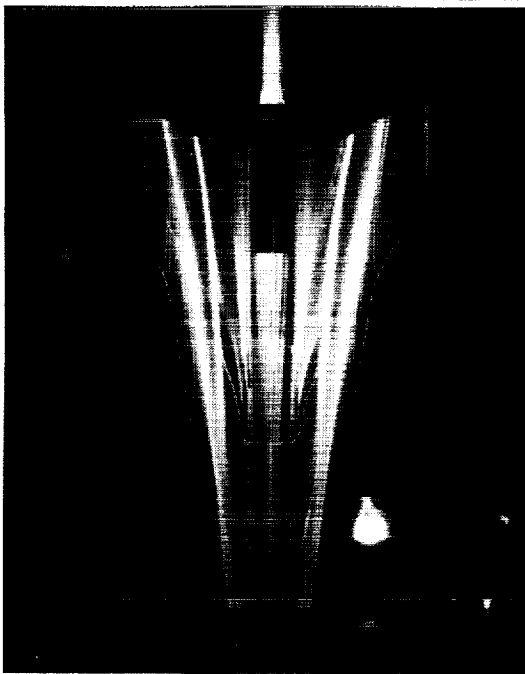
$\alpha = -1^\circ$, $\alpha = 1^\circ$, $\alpha = 3^\circ$, and $\alpha = 5^\circ$

$M = 3.0$

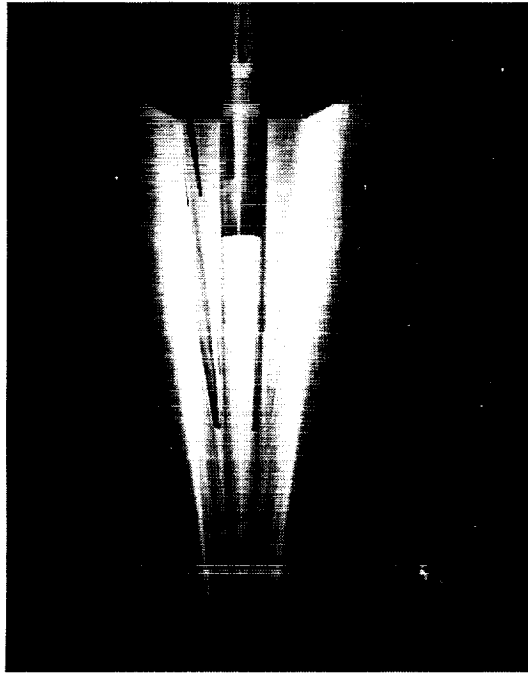
Bottom view

Nacelles off and on

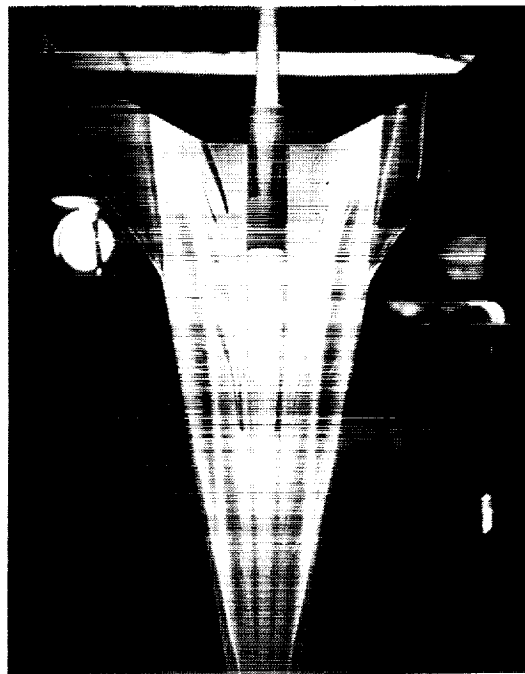
$\alpha = -1^\circ$, $\alpha = 1^\circ$, $\alpha = 3^\circ$, and $\alpha = 5^\circ$



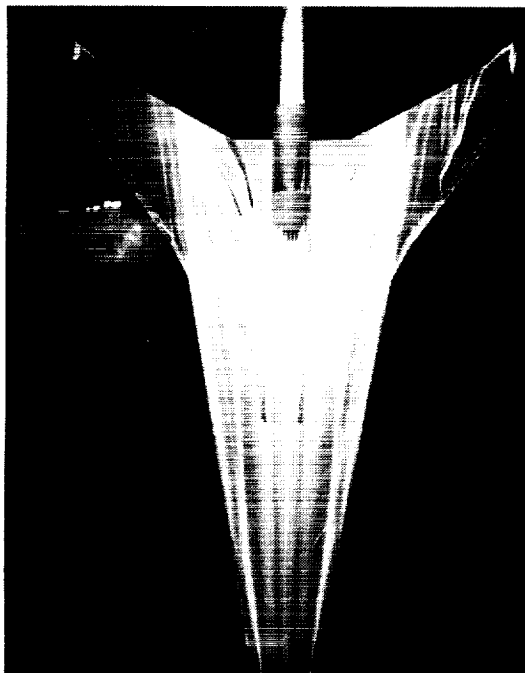
$\alpha = -1^\circ$



$\alpha = 1^\circ$

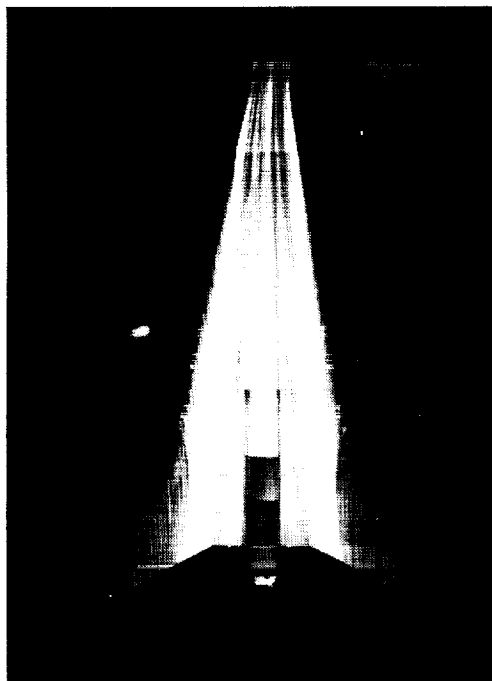


$\alpha = 3^\circ$

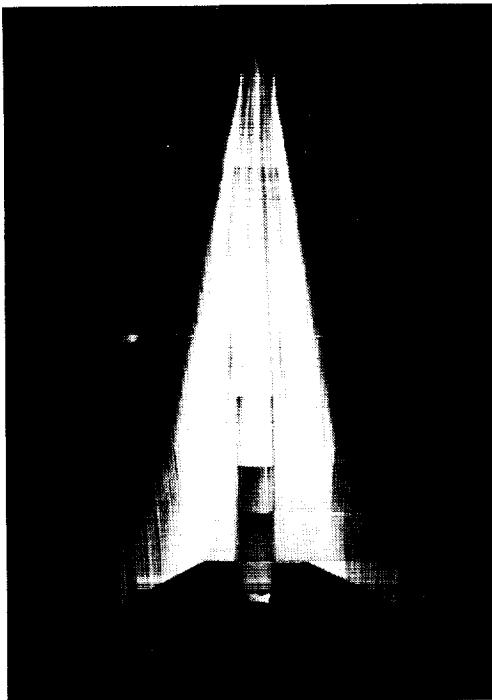


$\alpha = 5^\circ$

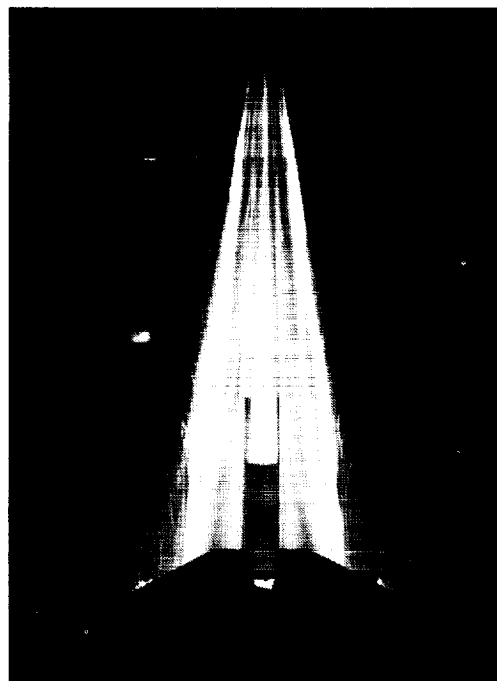
Figure C1. Oil flow photographs. Mach 1.6; nacelles off; top view.



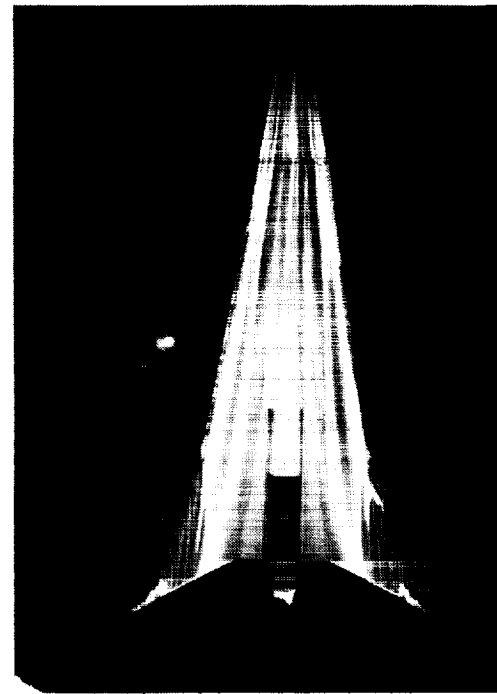
$\alpha = -1^\circ$



$\alpha = 1^\circ$

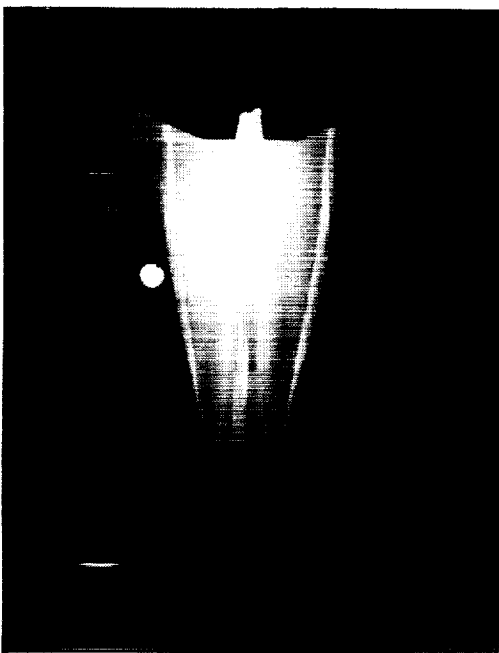


$\alpha = 3^\circ$

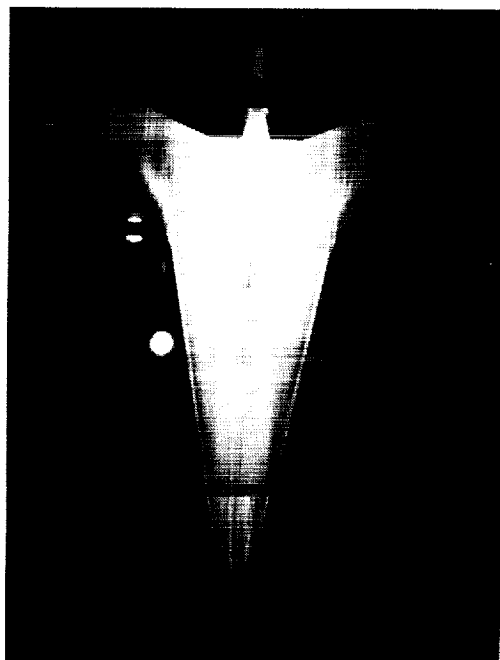


$\alpha = 5^\circ$

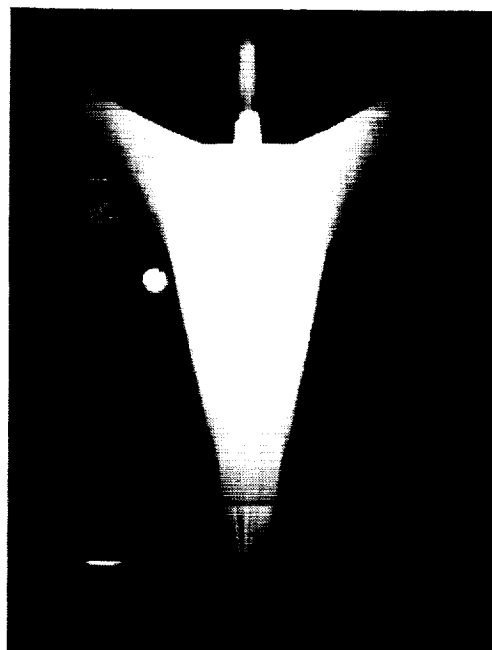
Figure C2. Oil flow photographs. Mach 3.0; nacelles off; top view.



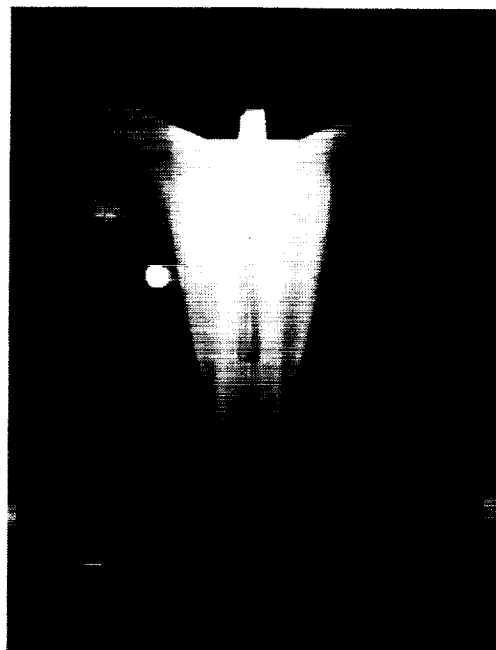
$\alpha = -1^\circ$



$\alpha = 1^\circ$

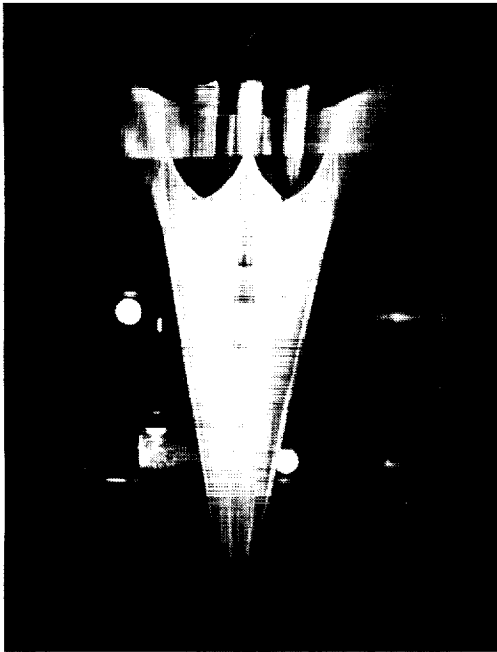


$\alpha = 3^\circ$

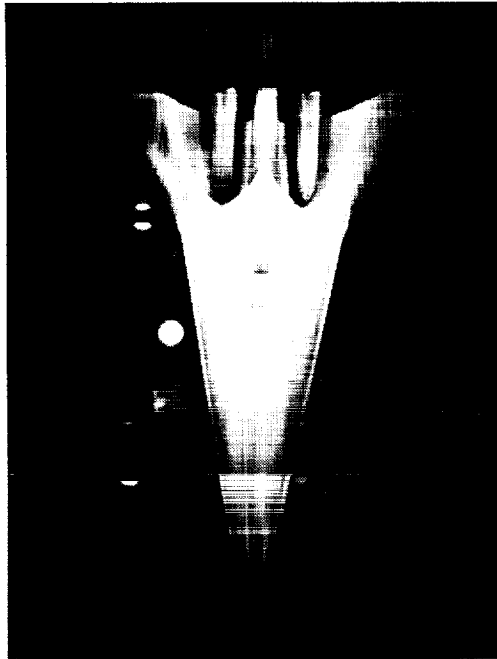


$\alpha = 5^\circ$

Figure C3. Oil flow photographs. Mach 3.0; nacelles off; bottom view.

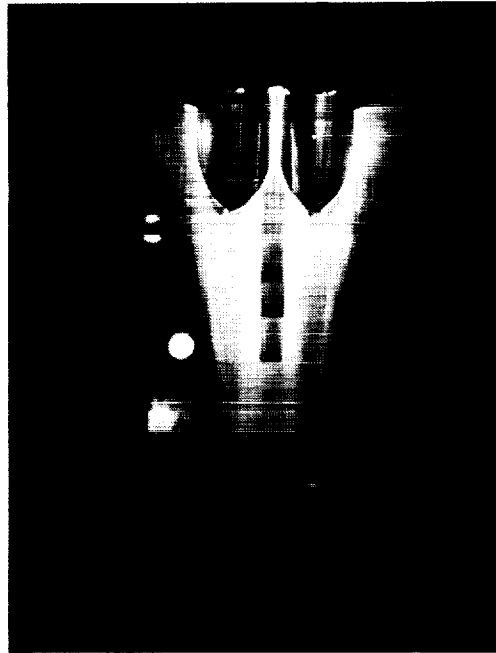


$\alpha = -1^\circ$



$\alpha = 1^\circ$

Photograph not available.



$\alpha = 5^\circ$

$\alpha = 3^\circ$

Figure C4. Oil flow photographs. Mach 3.0; nacelles on; bottom view.

Appendix D

Surface Pressure Plots

Surface pressures were plotted for the following conditions --

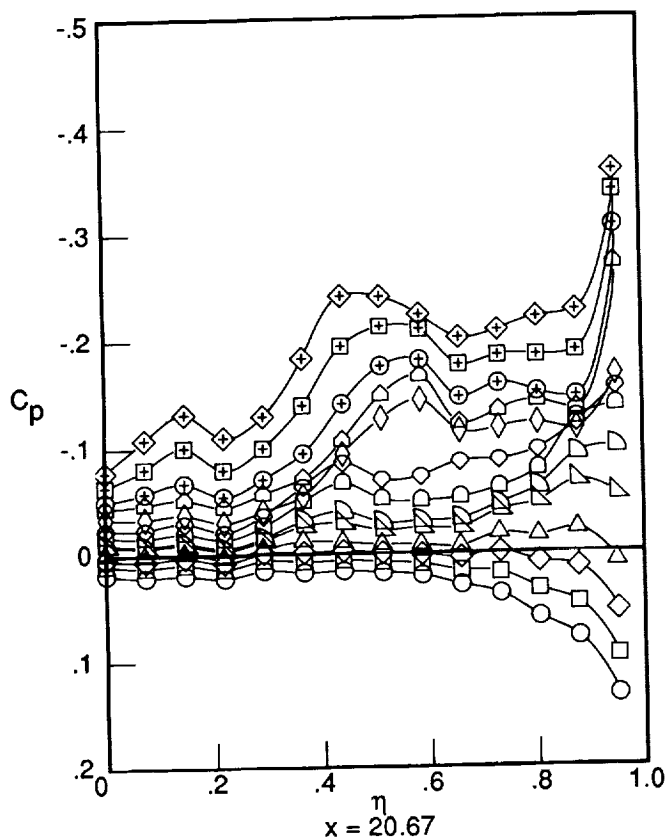
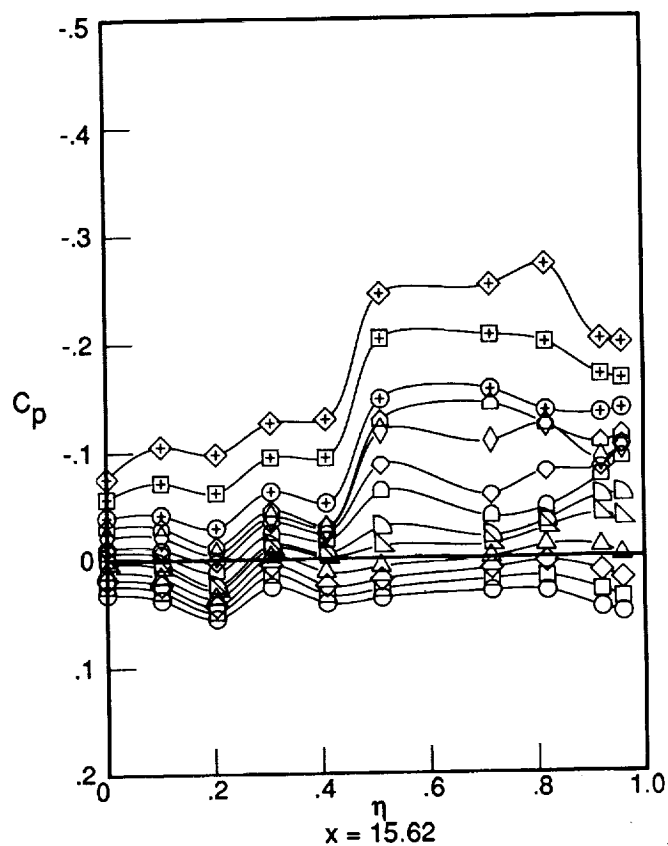
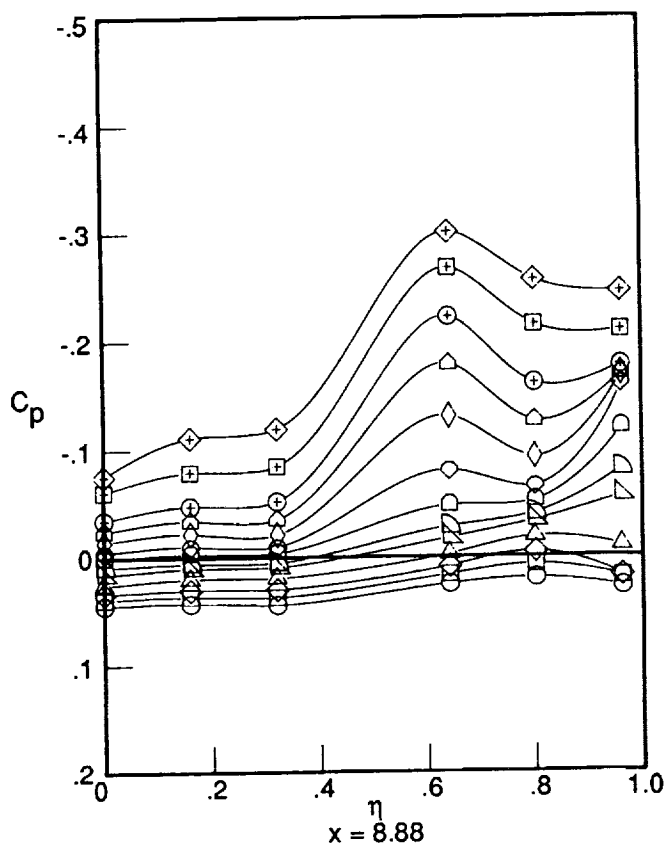
$M = 1.6, 2.0, 2.4, 2.8, 3.0, 3.2,$ and 3.6

$\alpha = -4^\circ - 10^\circ$

$x = 8.88, 15.62, 20.67, 20.67$ (lower surface), and 23.00

$y = 2.11$ and 6.04

With and without nacelles



α	
-3.94	○
-3.00	□
-2.04	◇
-1.10	△
.06	▽
.96	◐
2.05	◑
3.06	◒
4.07	◓
4.99	◔
5.98	⊕
8.04	⊞
10.03	⊠

Figure D1. Surface pressure distributions. Mach 1.6; nacelles off.

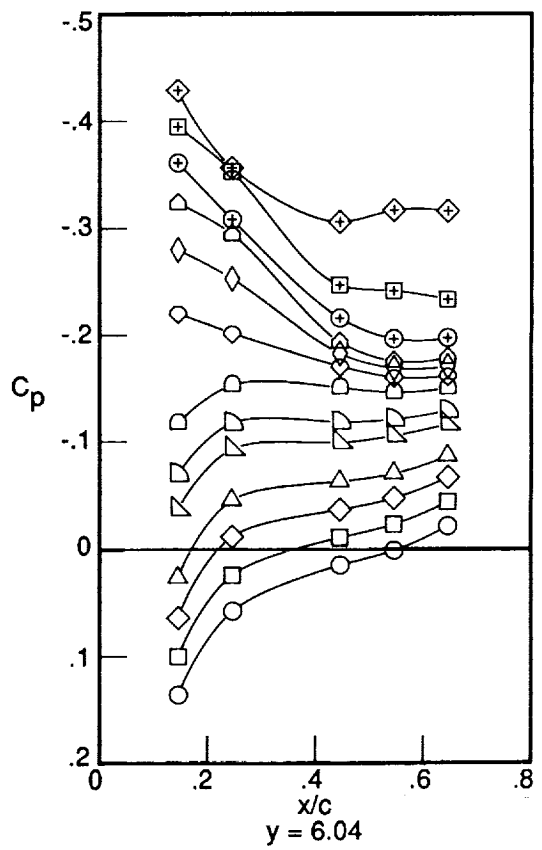
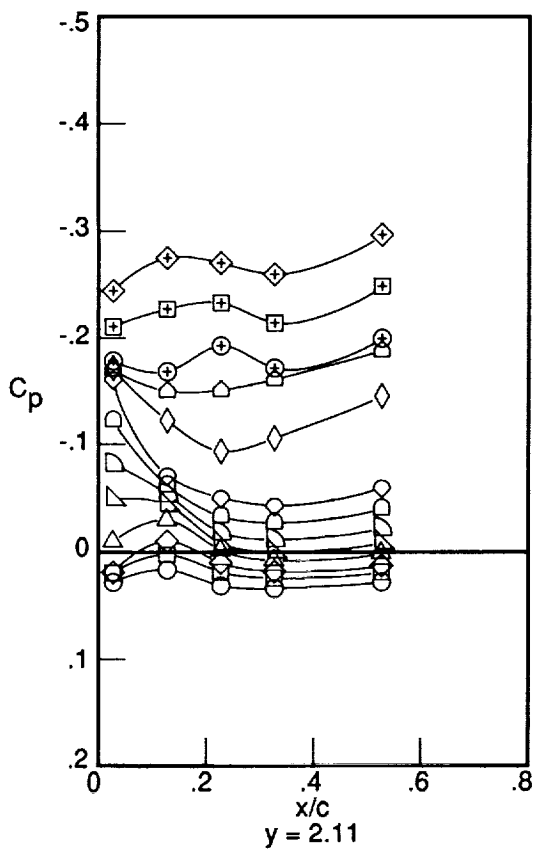
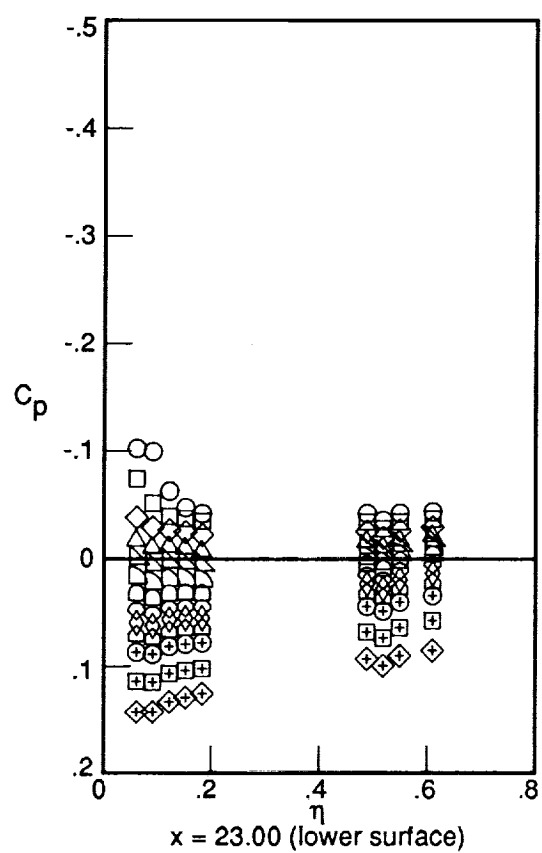
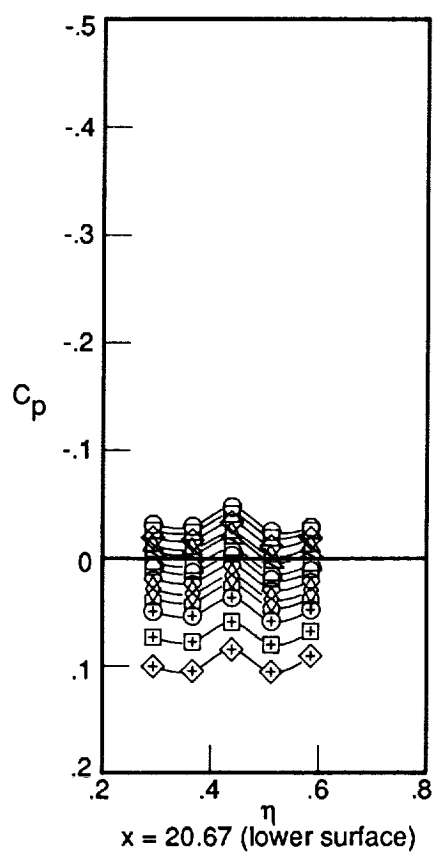


Figure D1. Concluded.

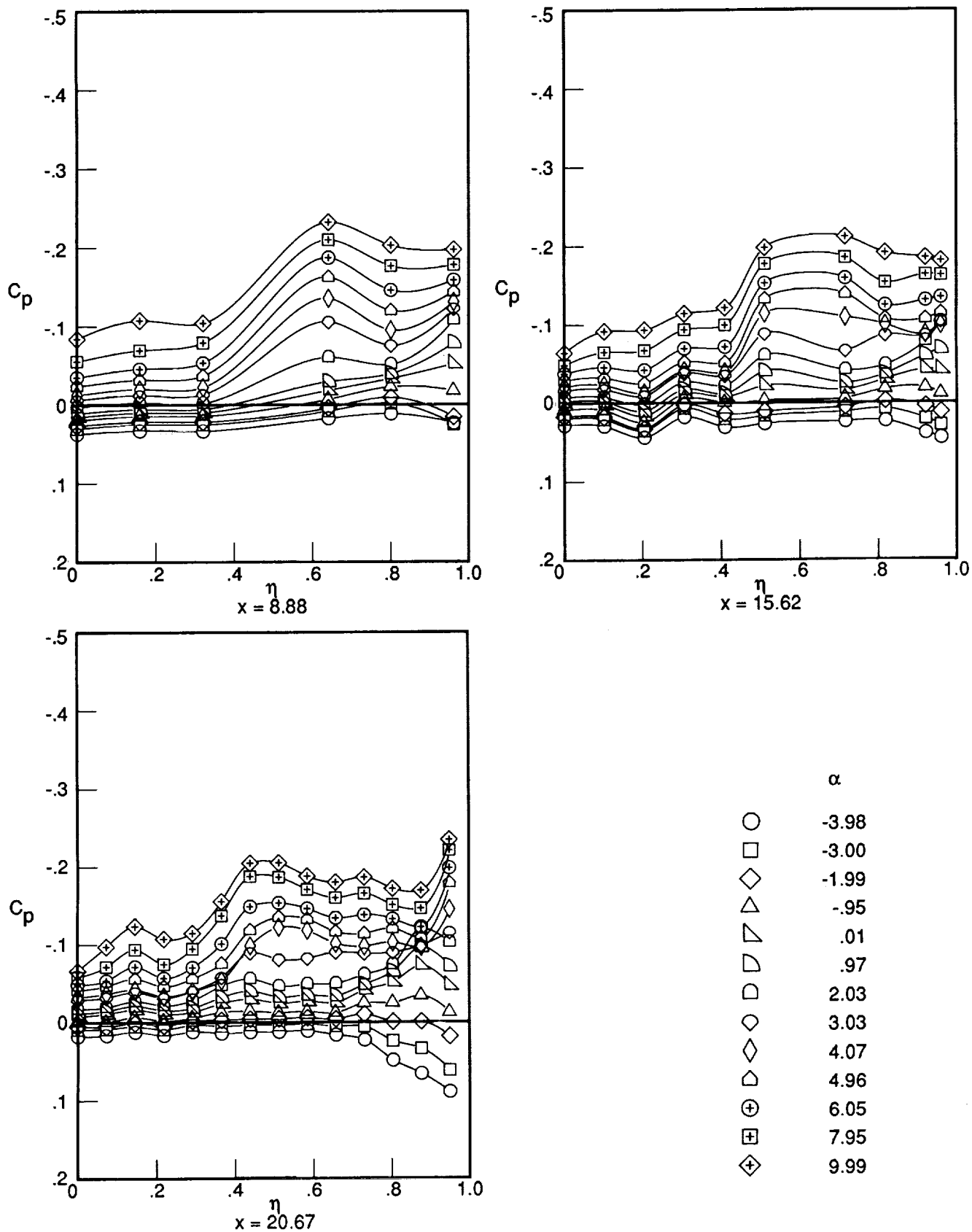


Figure D2. Surface pressure distributions. Mach 2.0; nacelles off.

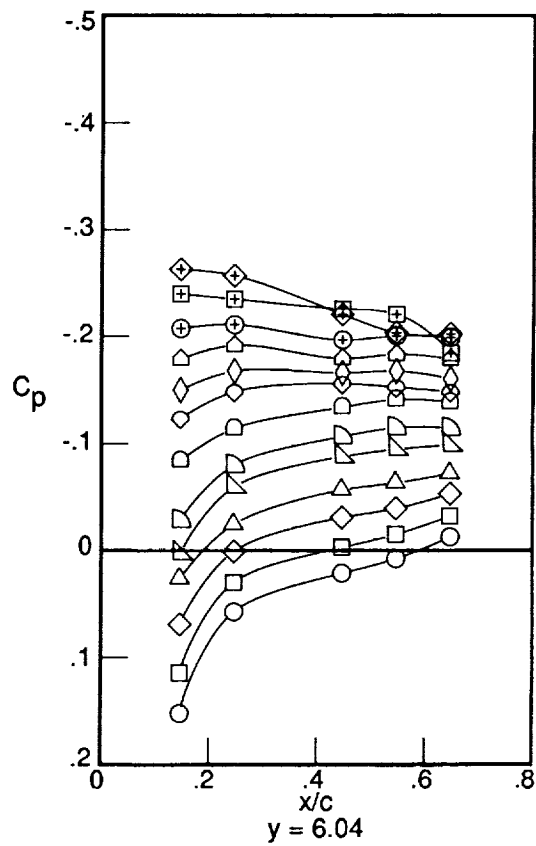
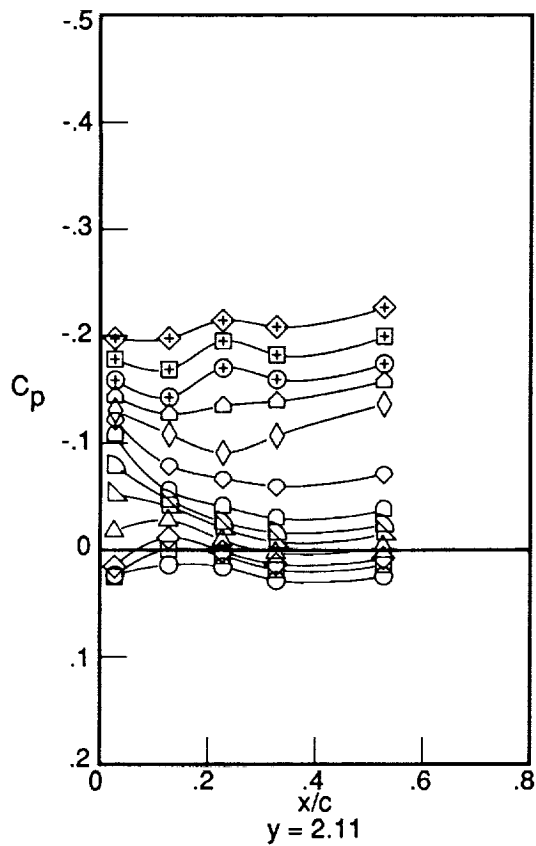
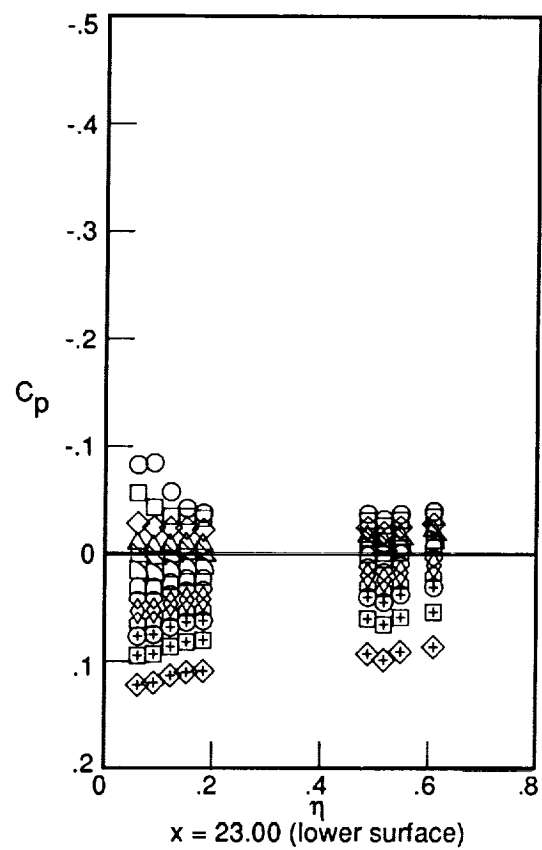
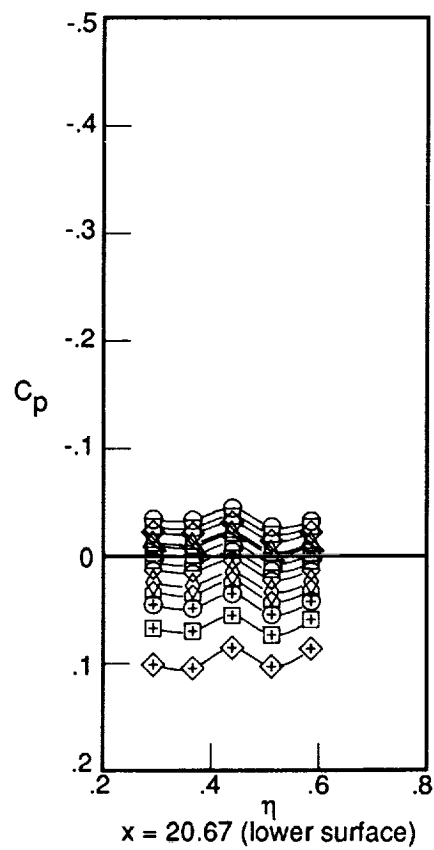
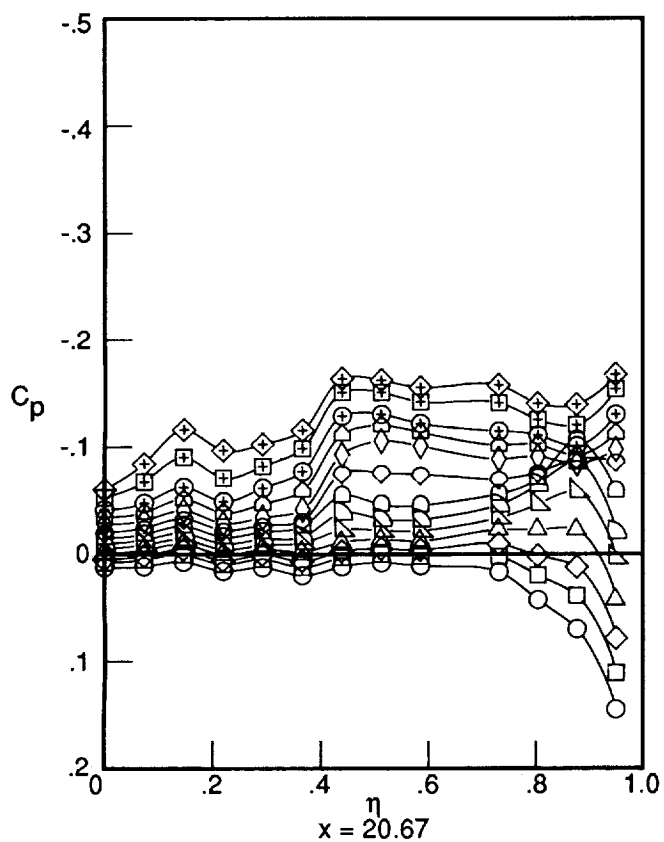
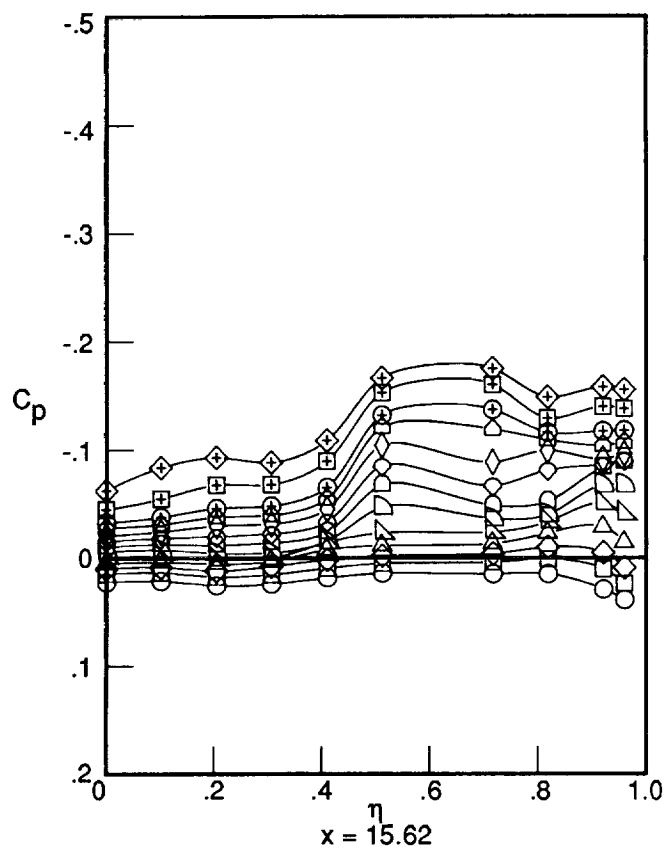
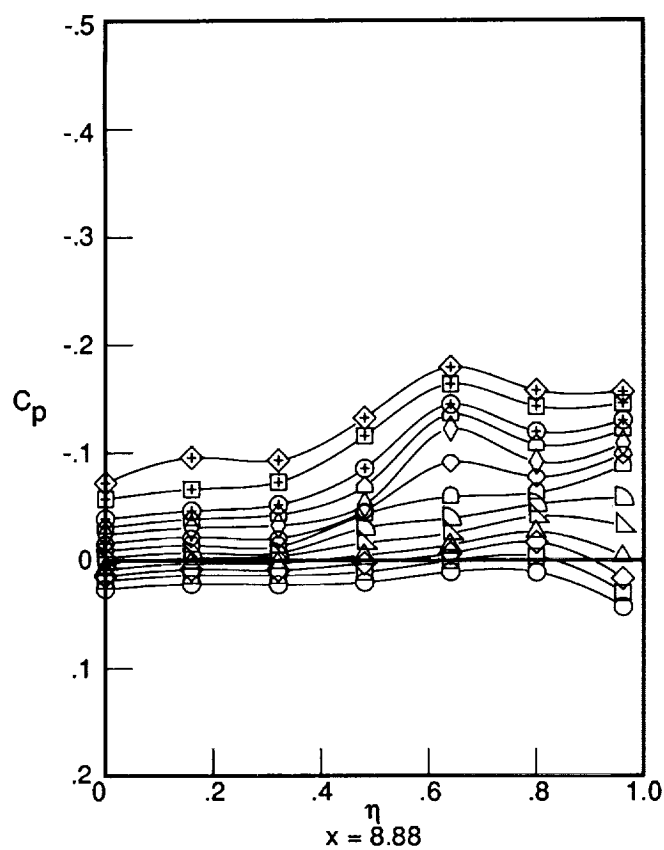


Figure D2. Concluded.



α	
-4.04	○
-2.97	□
-2.00	◇
-1.00	△
0.00	▽
.99	◐
1.98	◑
2.96	◒
3.97	◅
5.01	◈
5.99	⊕
7.97	⊞
9.96	⊠

Figure D3. Surface pressure distributions. Mach 2.4; nacelles off.

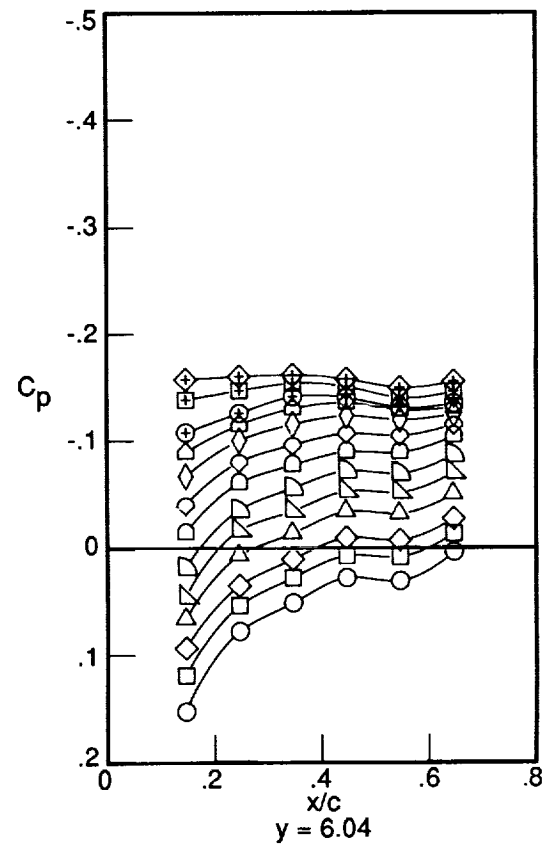
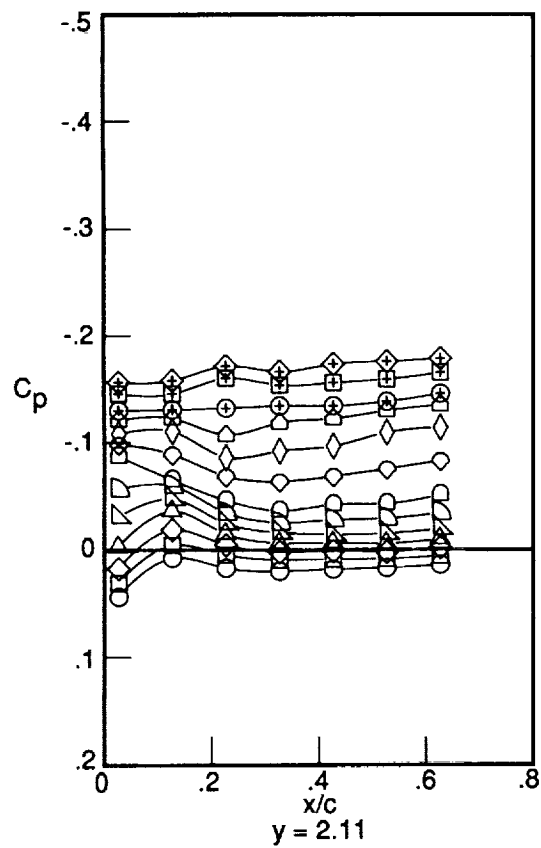
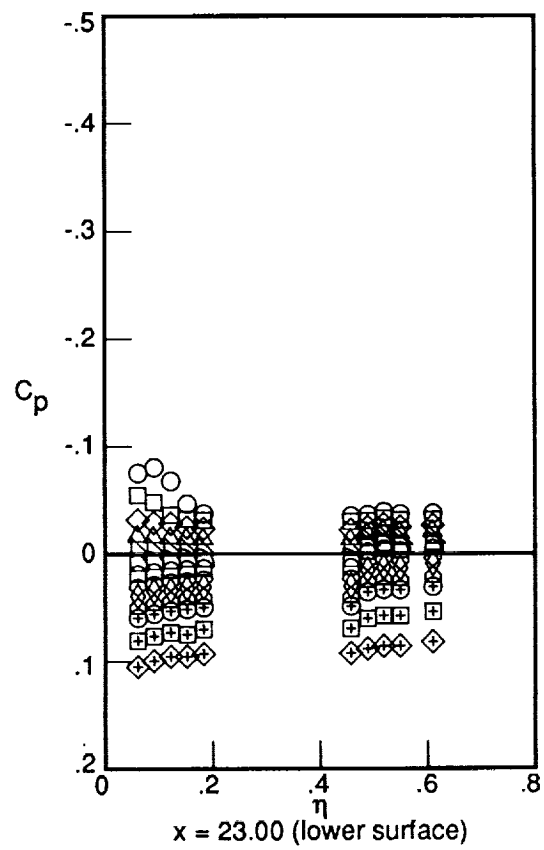
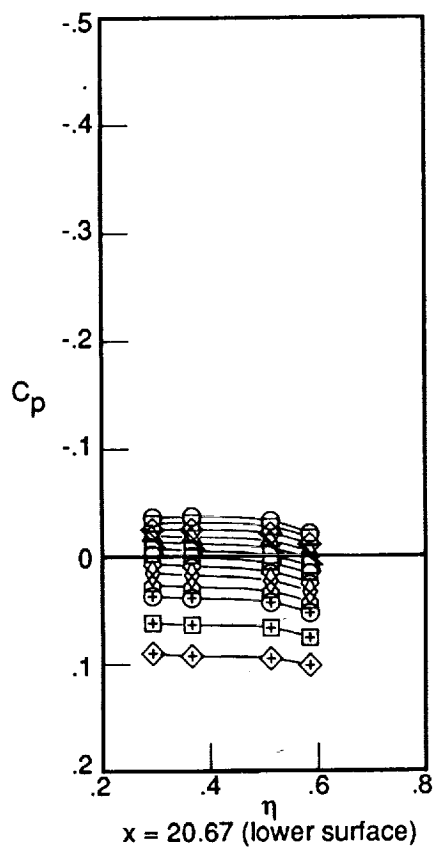
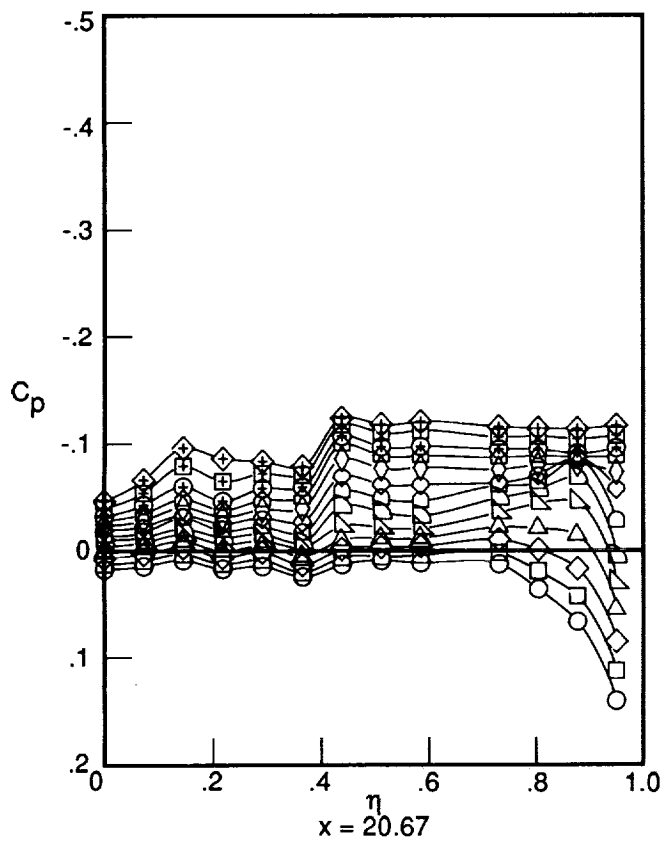
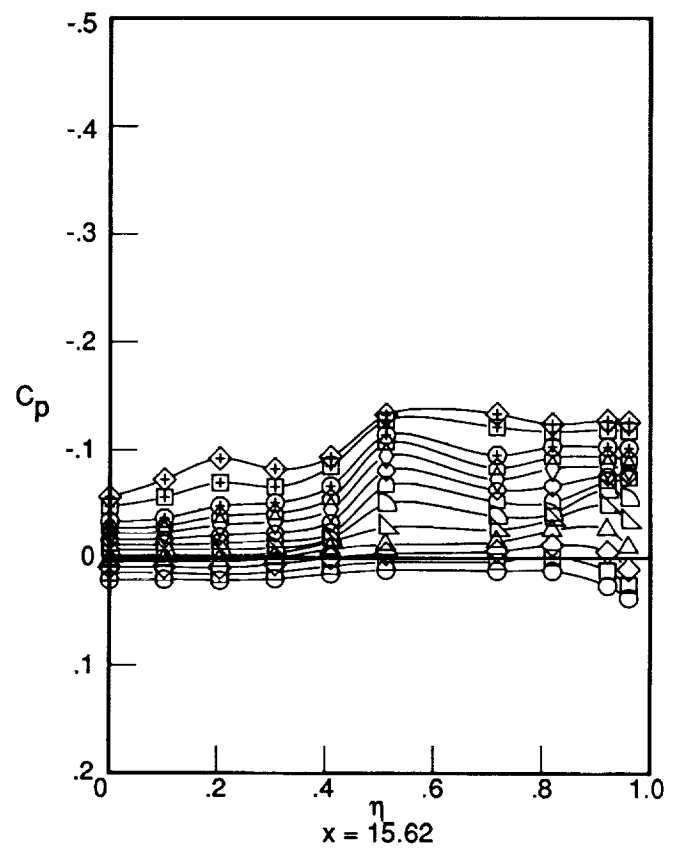
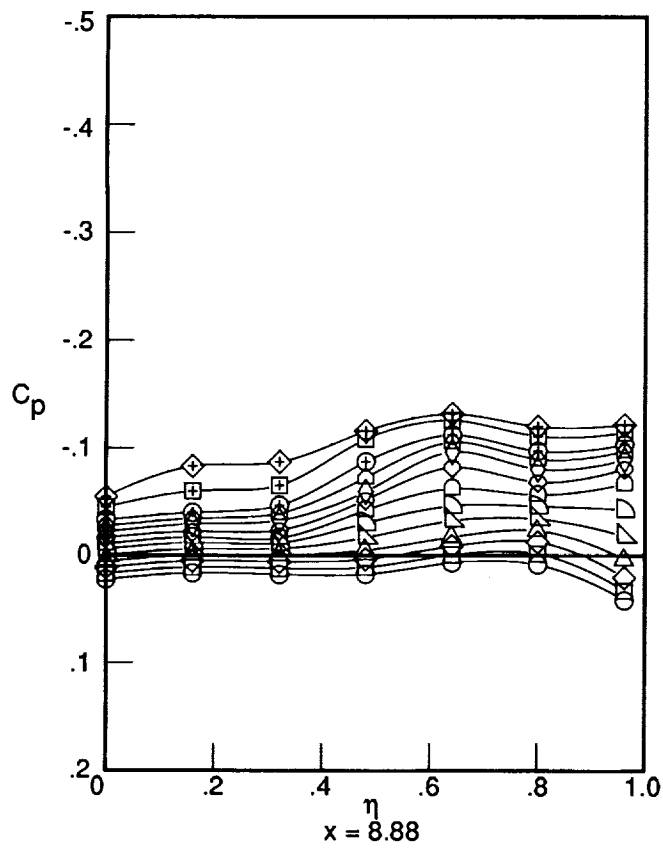


Figure D3. Concluded.



α	
-4.00	○
-2.99	□
-1.99	◇
-.99	△
.04	▽
1.04	◐
2.00	◑
3.01	◒
4.04	◓
4.98	◔
6.04	⊕
8.05	⊞
10.00	⊠

Figure D4. Surface pressure distributions. Mach 2.8; nacelles off.

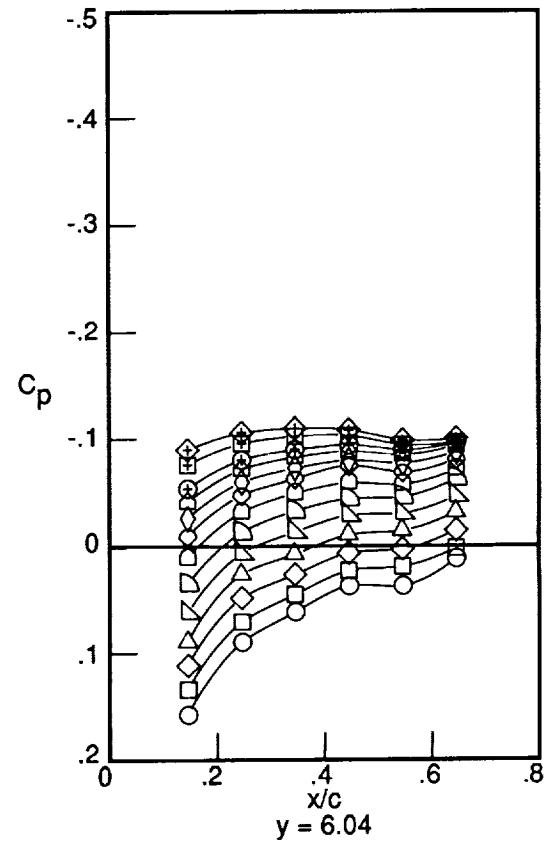
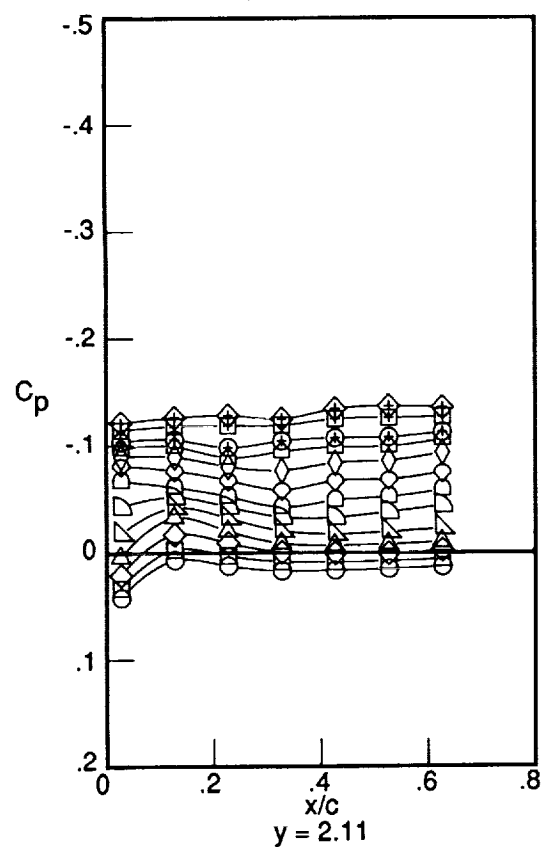
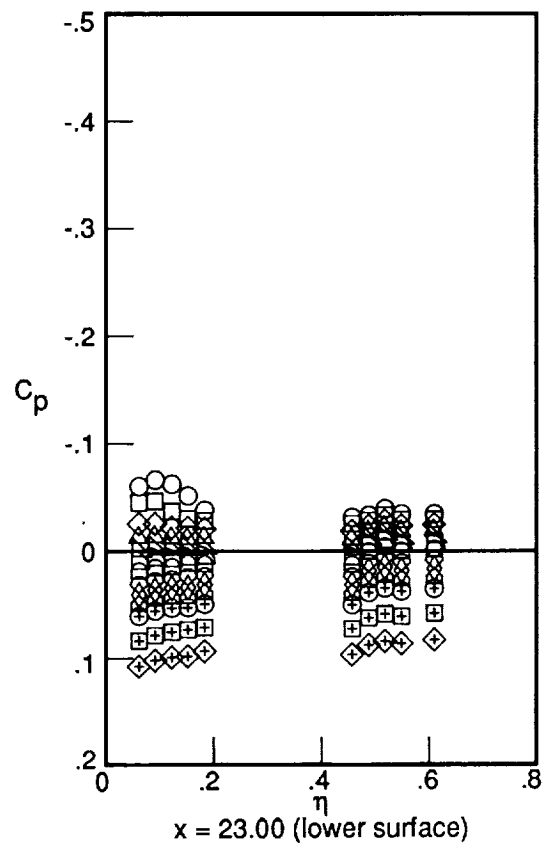
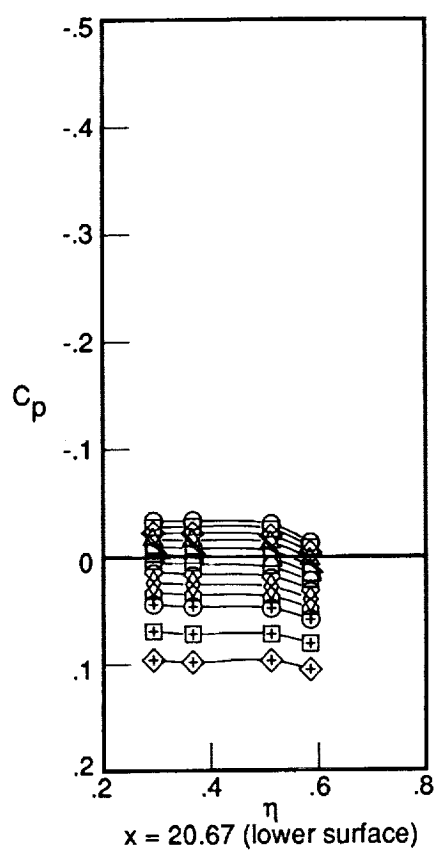
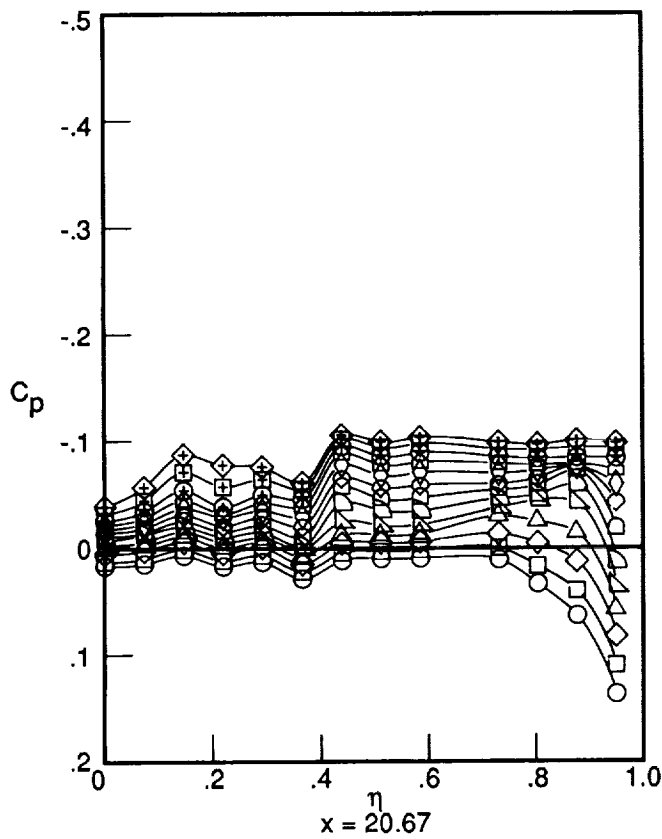
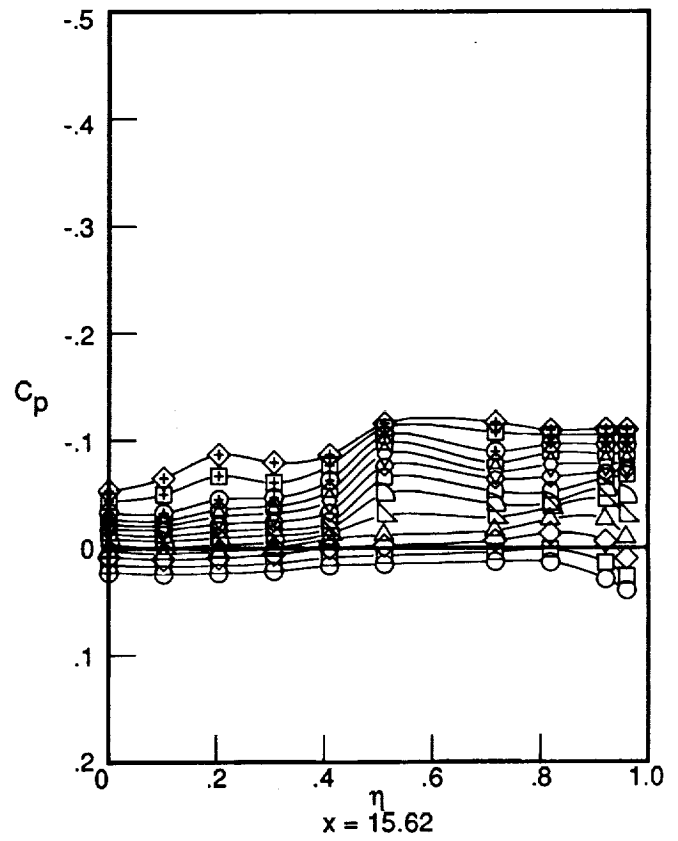
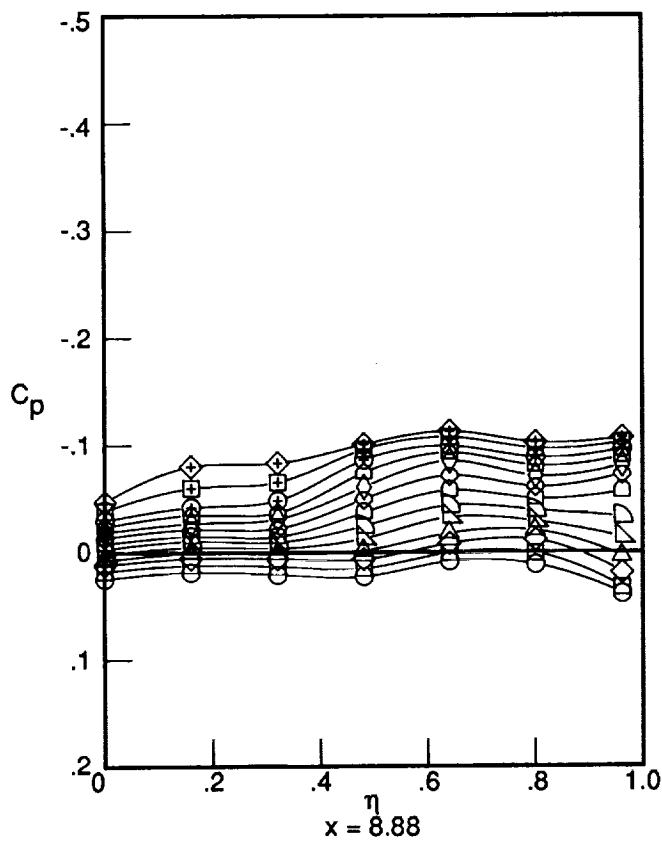


Figure D4. Concluded.



α	
-4.02	○
-3.03	□
-1.96	◇
-1.01	△
.01	▵
1.02	◻
1.98	◊
2.99	◈
3.98	◊
4.99	◈
6.04	⊕
8.06	⊕
10.10	⊕

Figure D5. Surface pressure distributions. Mach 3.0; nacelles off.

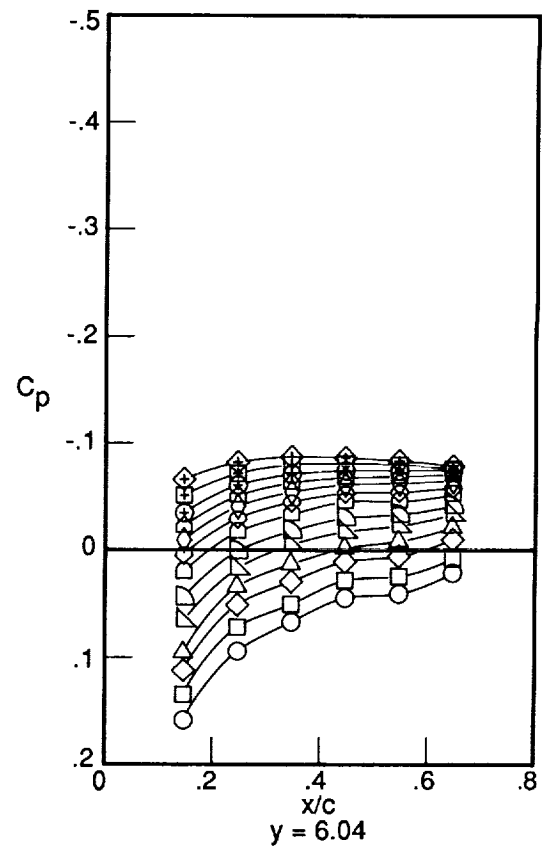
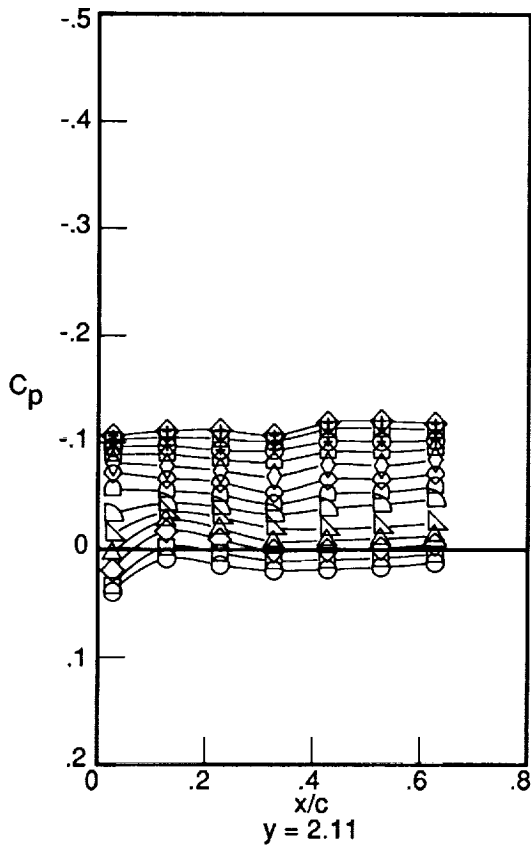
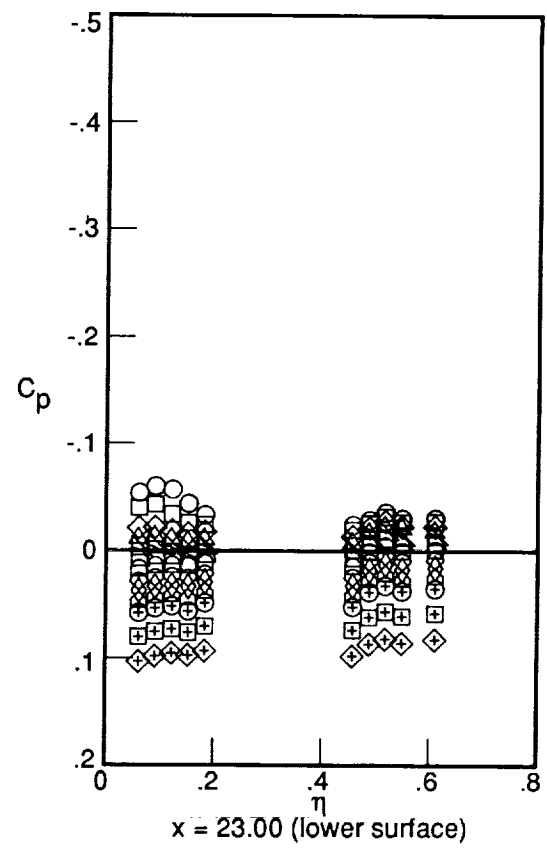
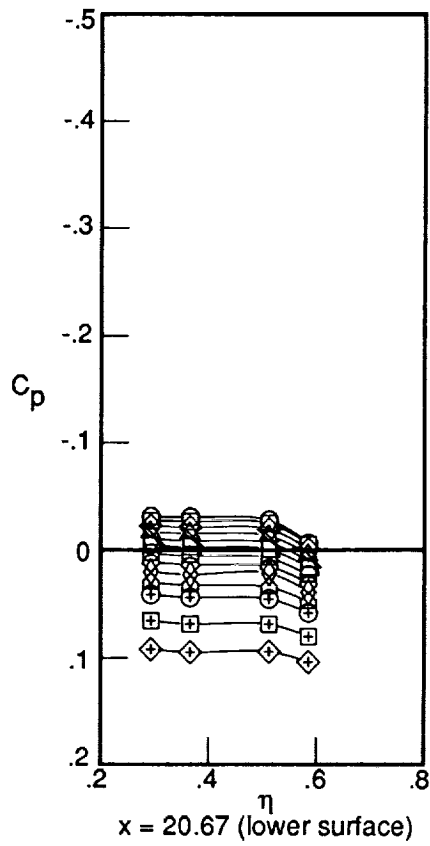
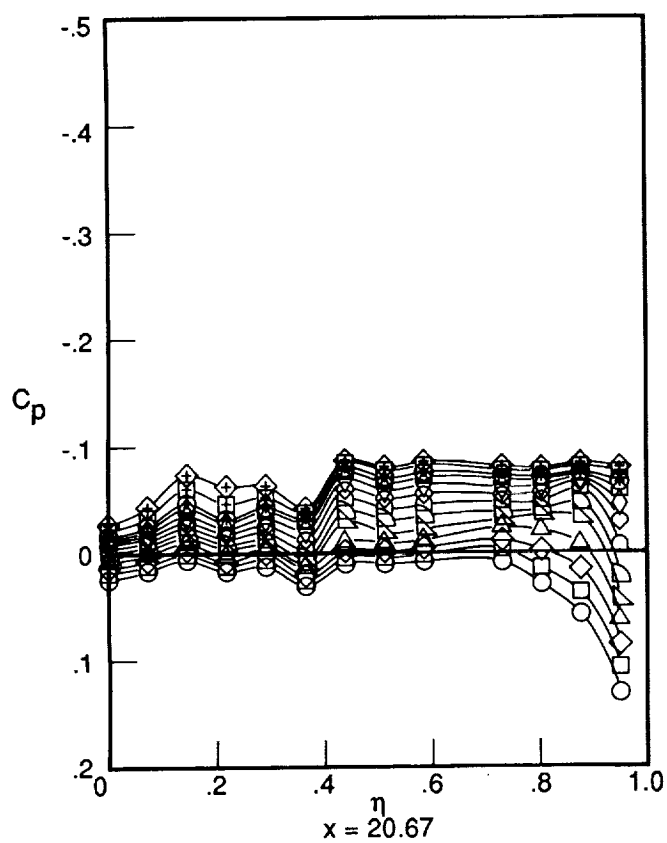
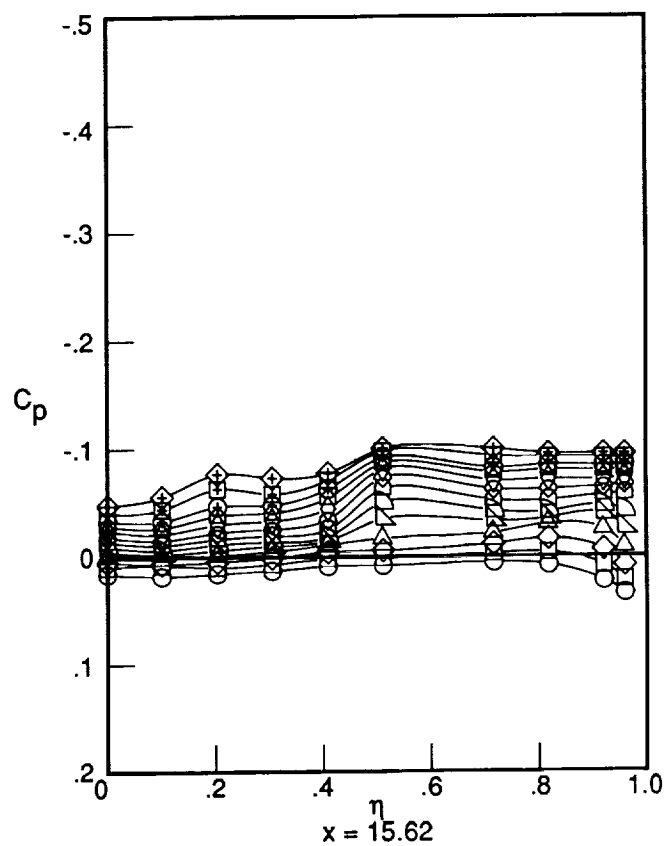
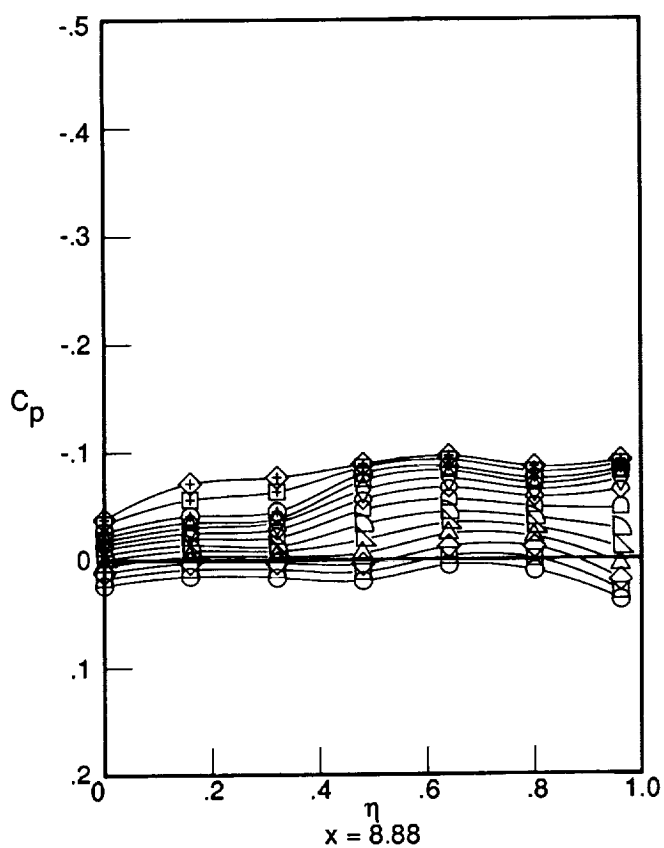


Figure D5. Concluded.



α	
-3.99	○
-2.99	□
-2.02	◇
-.99	△
.01	▽
.99	◐
2.01	◑
2.98	◊
4.05	◈
4.96	◉
6.04	⊕
8.00	⊞
10.00	⊠

Figure D6. Surface pressure distributions. Mach 3.2; nacelles off.

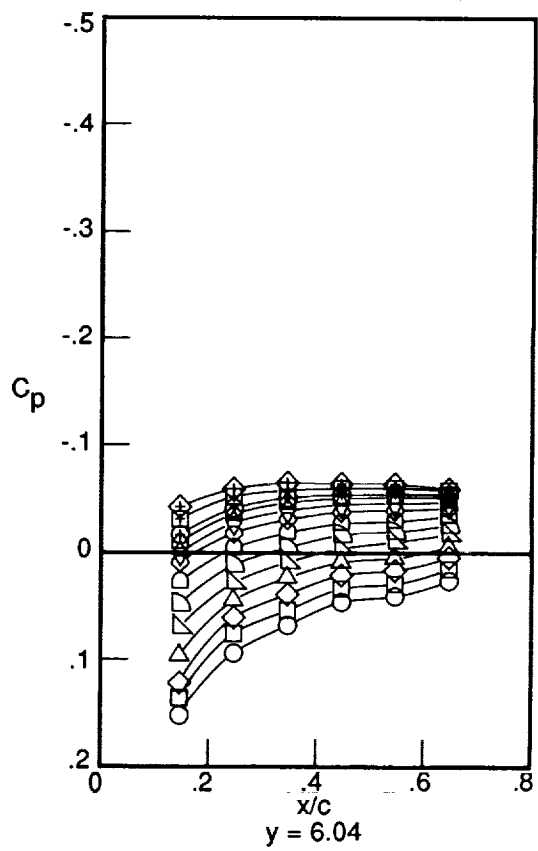
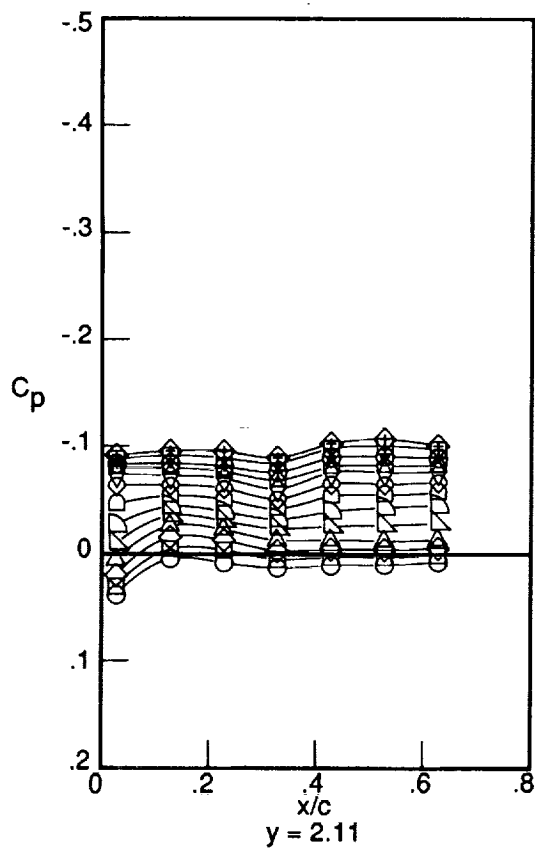
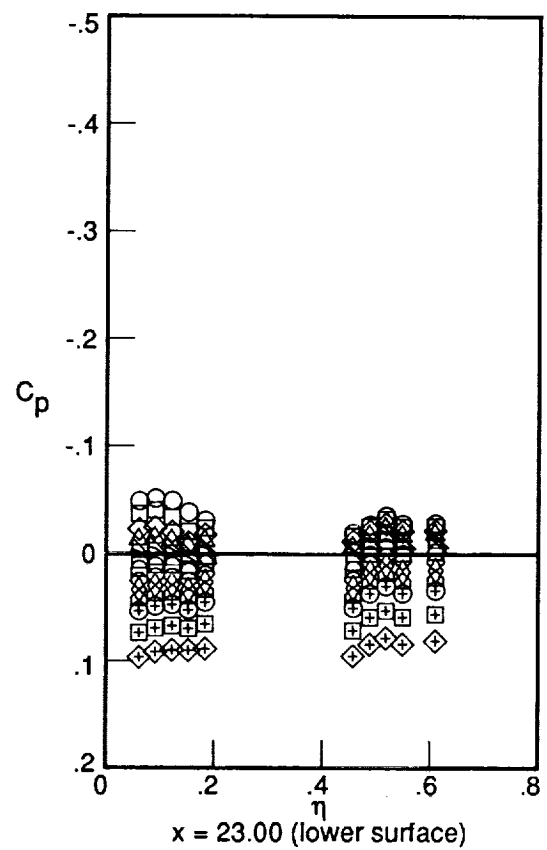
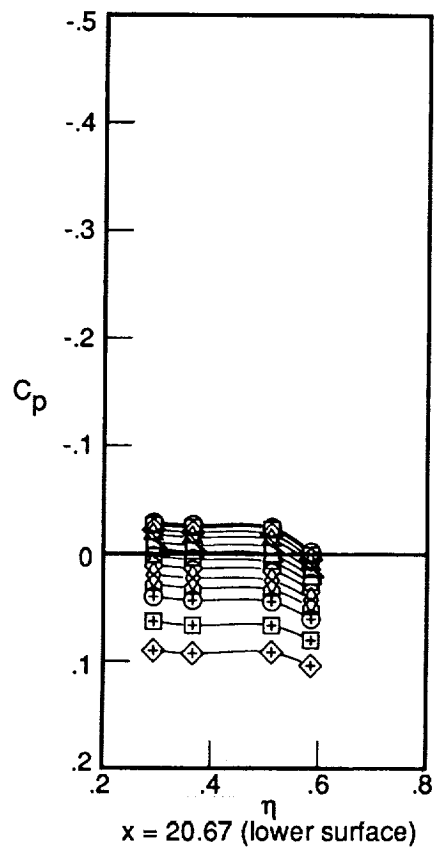
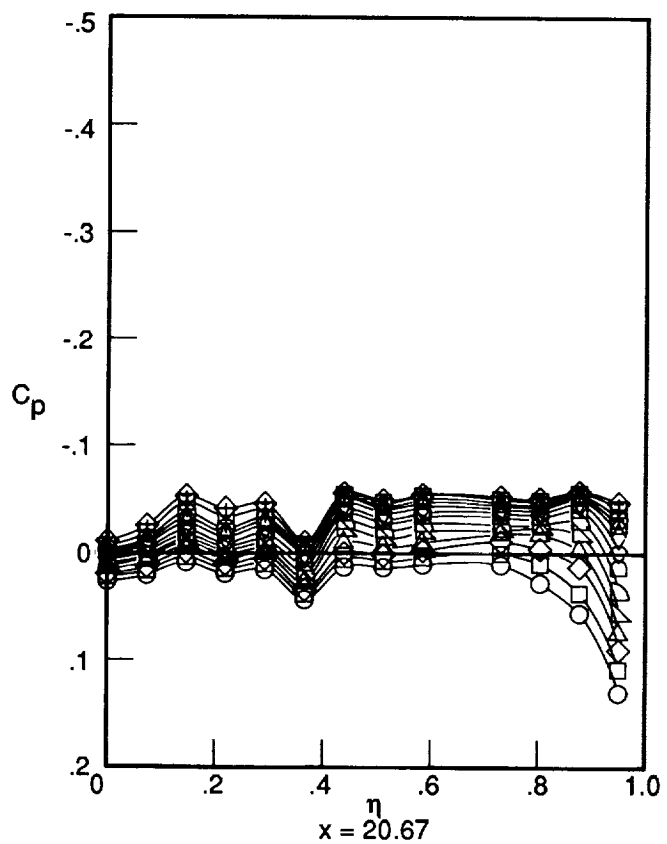
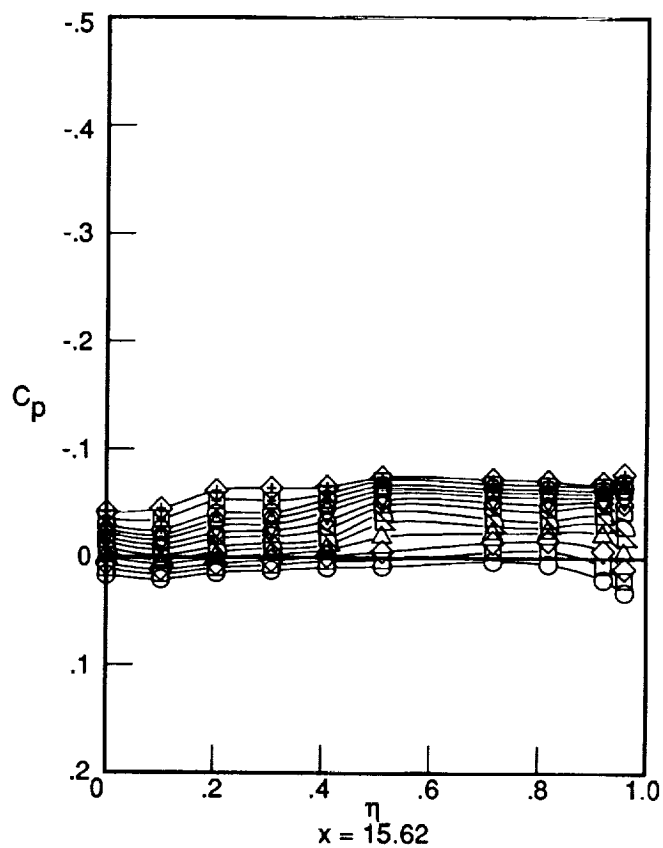
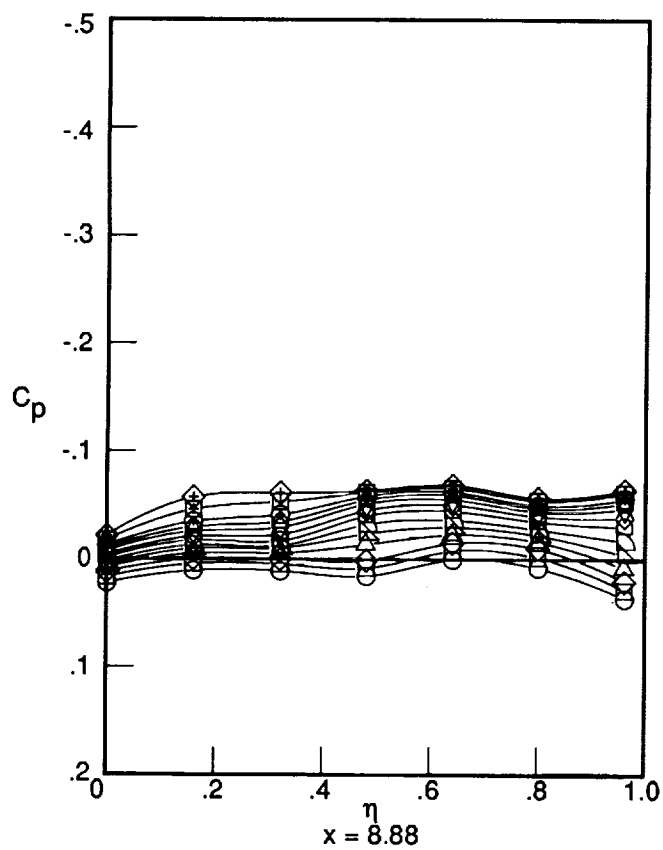


Figure D6. Concluded.



	α
○	-4.04
□	-2.98
◇	-2.01
△	-.97
▽	.02
▢	.99
◻	2.04
◊	3.01
◇	4.04
△	4.98
⊕	6.04
⊕	7.99
⊕	10.01

Figure D7. Surface pressure distributions. Mach 3.6; nacelles off.

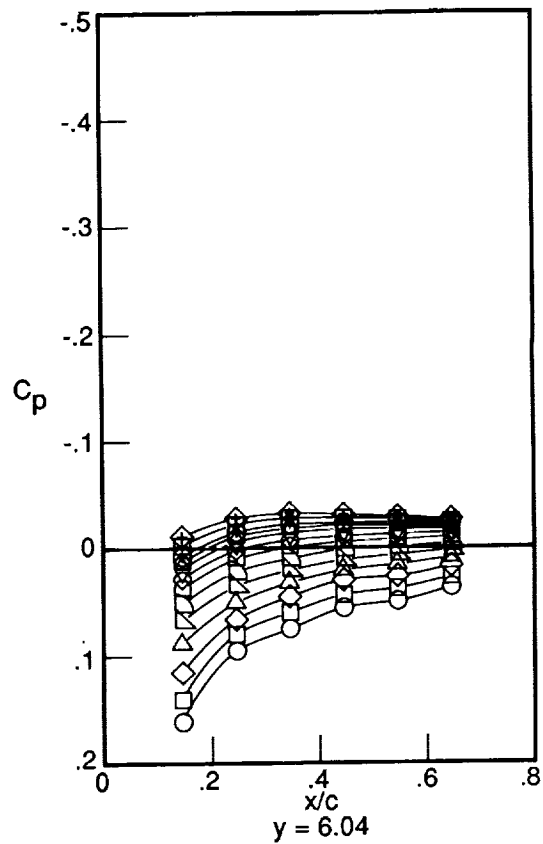
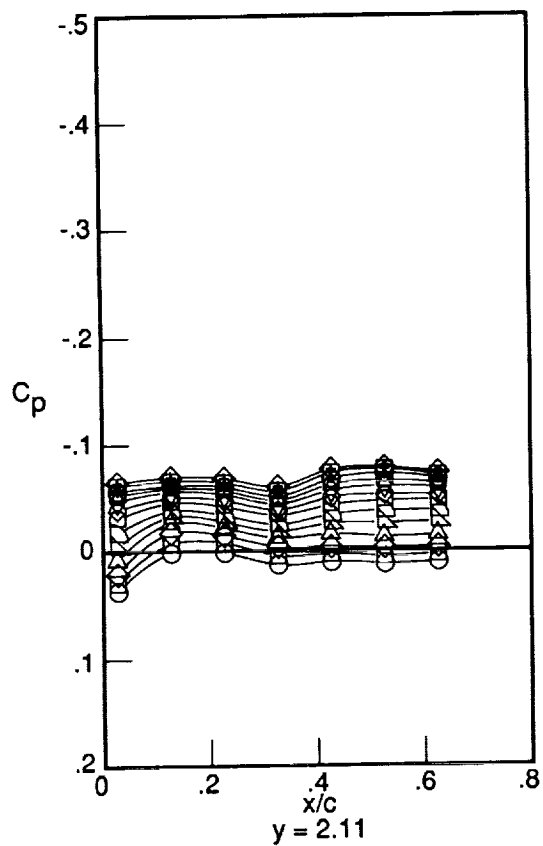
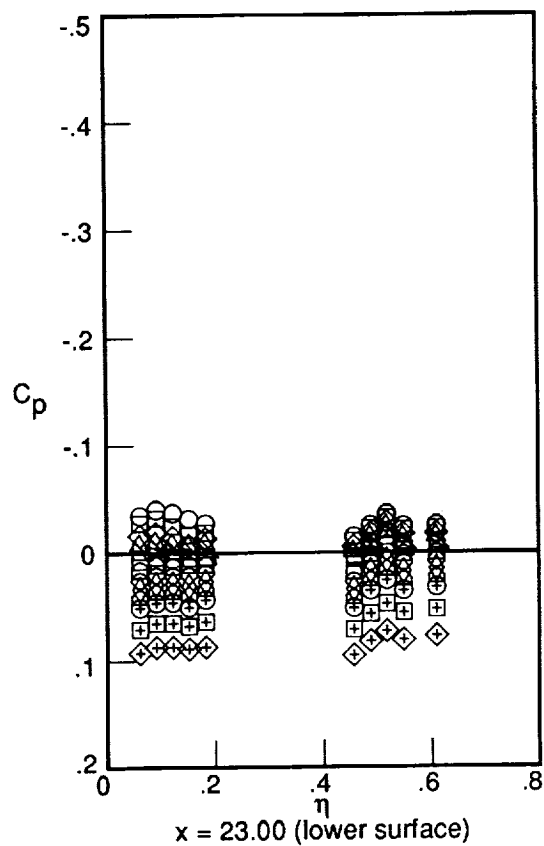
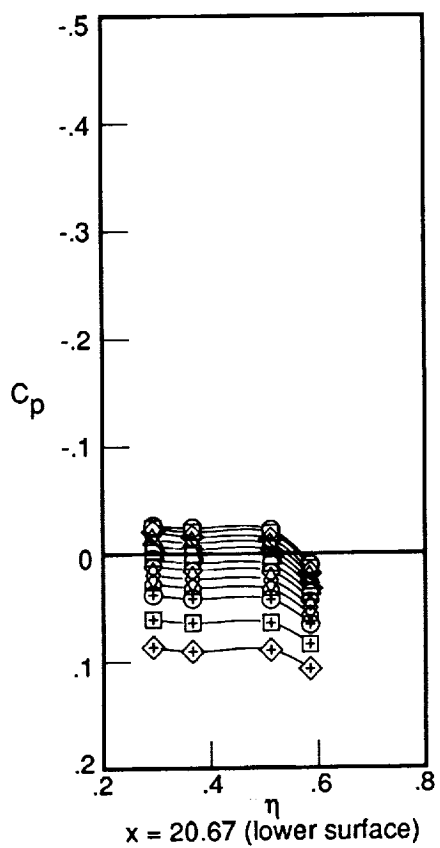
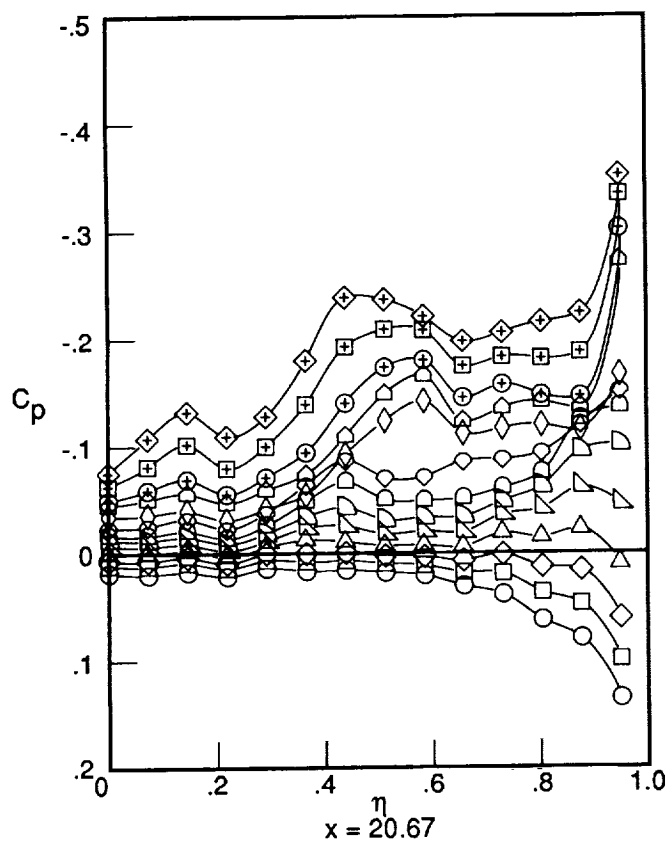
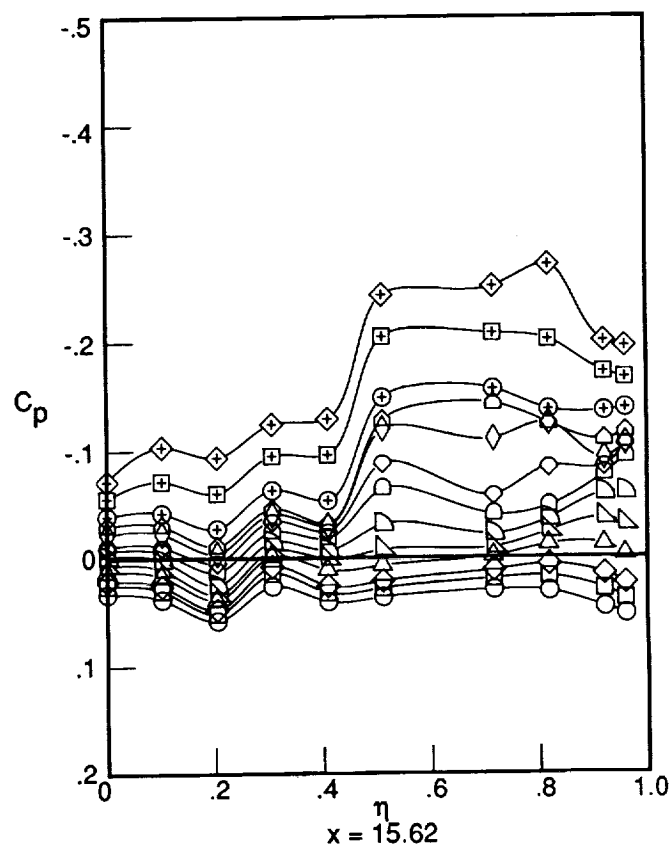
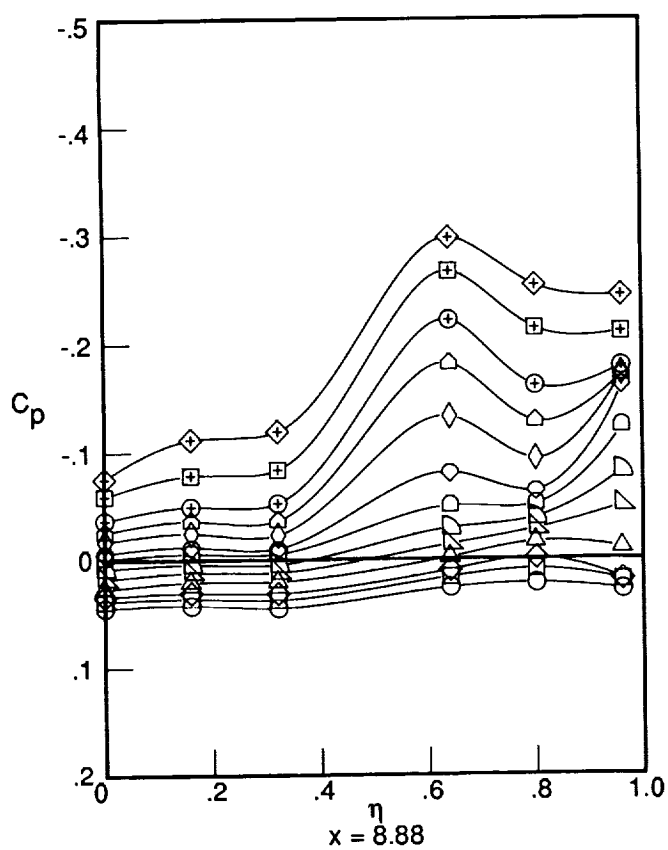


Figure D7. Concluded.



	α
○	-3.97
□	-3.00
◇	-2.07
△	-1.07
▽	.07
▢	.96
◻	2.09
◊	3.05
◇	4.05
△	5.03
⊕	5.98
⊕	8.06
⊕	10.04

Figure D8. Surface pressure distributions. Mach 1.6; nacelles on.

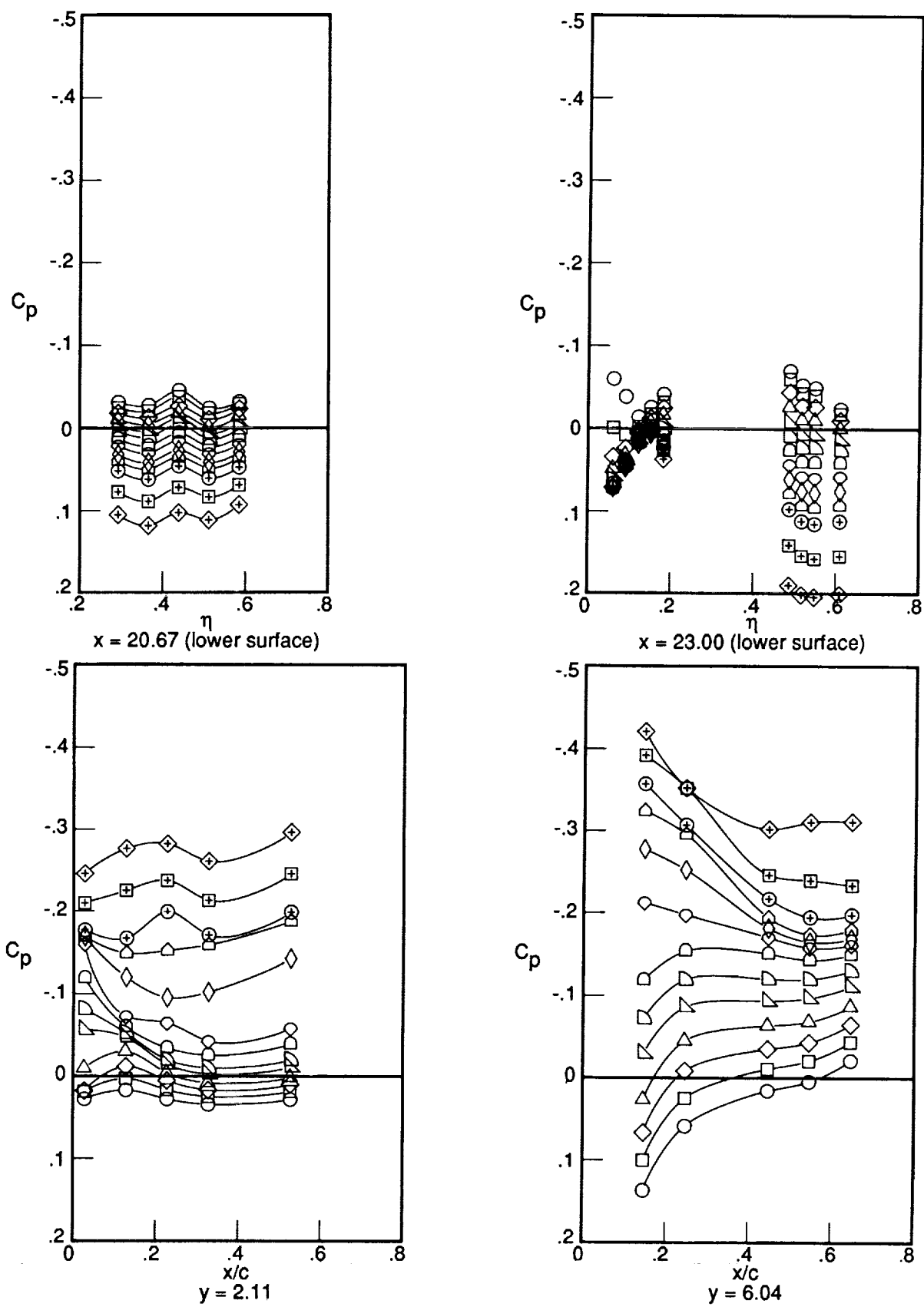
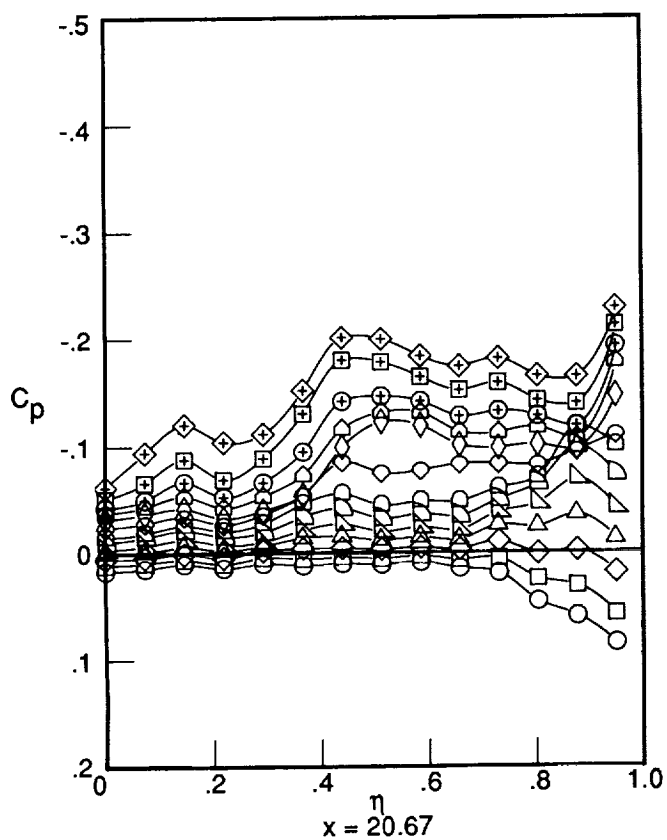
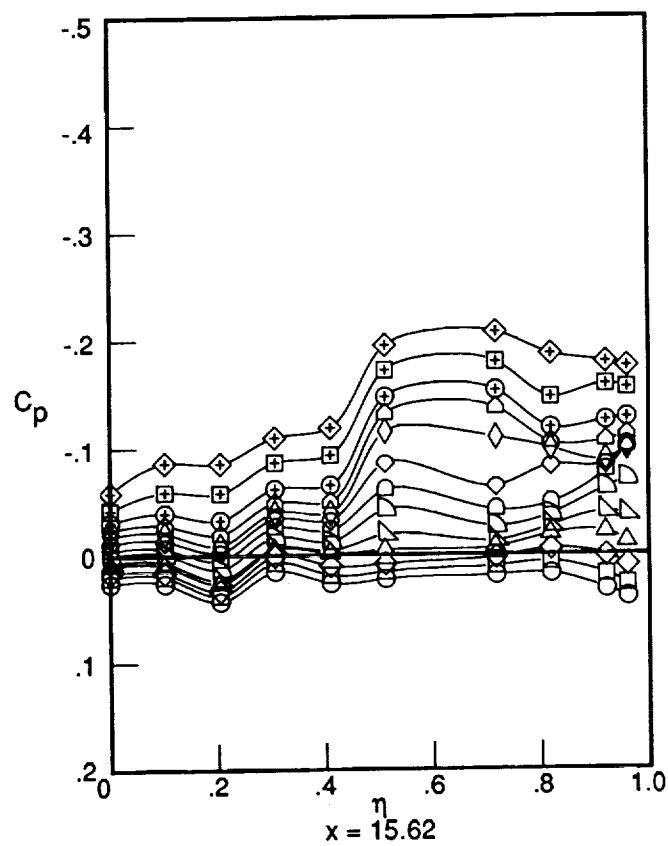
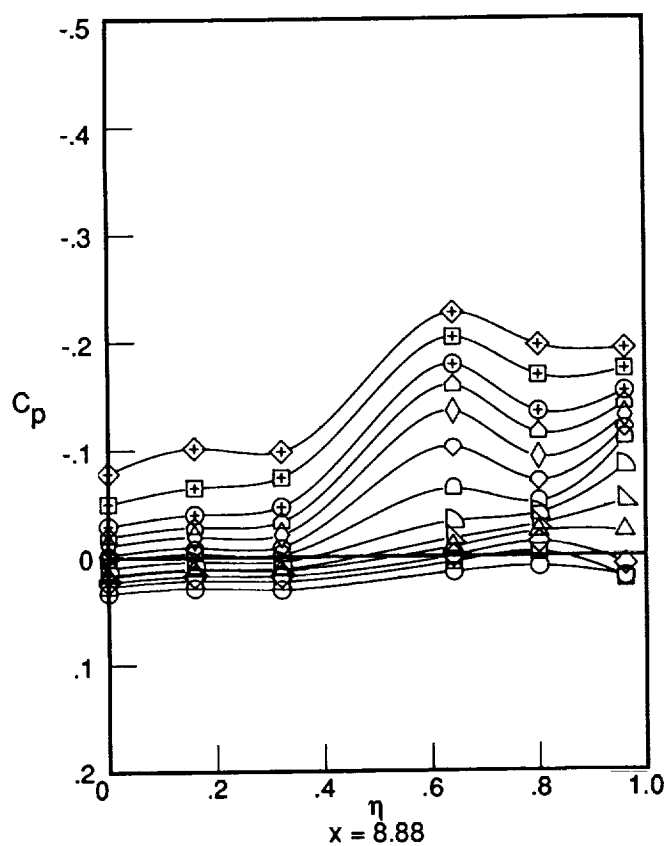


Figure D8. Concluded.



α	
-3.97	○
-2.99	□
-2.02	◇
-.97	△
0.00	▽
.99	◐
2.04	◑
3.02	◊
4.09	◈
4.99	◉
6.02	⊕
7.95	⊞
10.01	⊠

Figure D9. Surface pressure distributions. Mach 2.0; nacelles on.

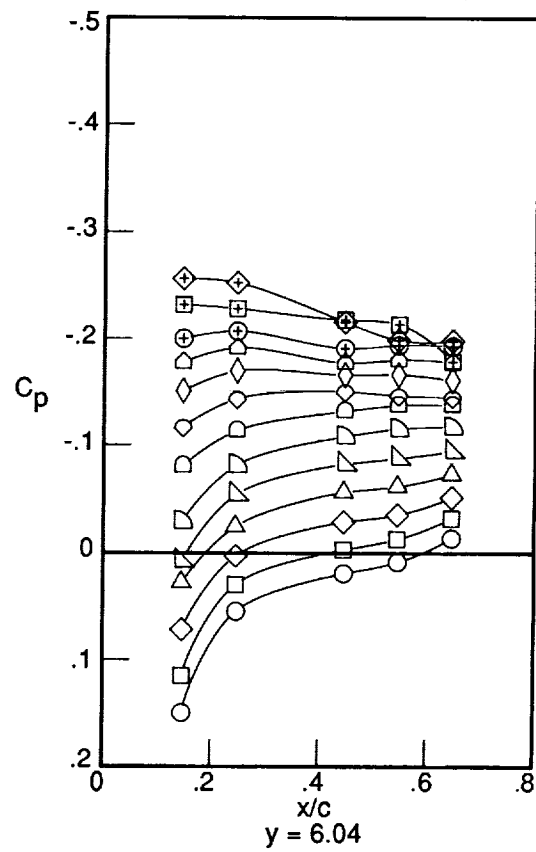
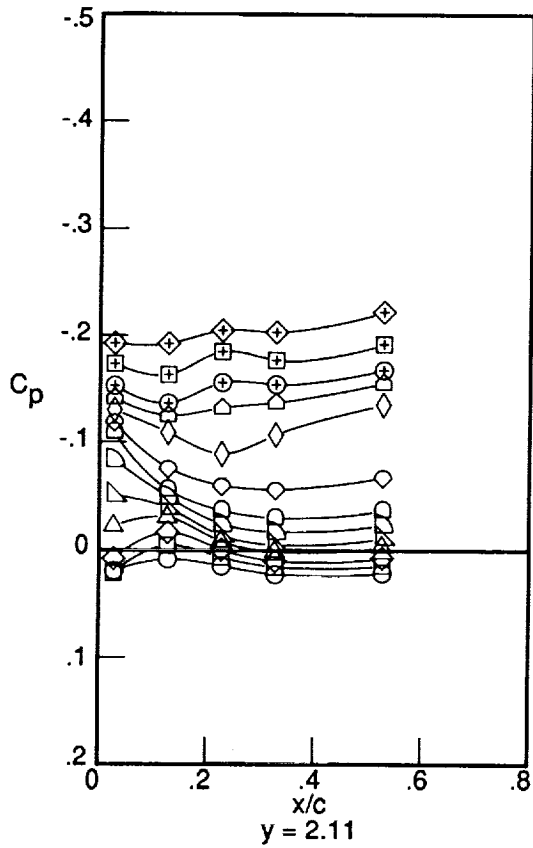
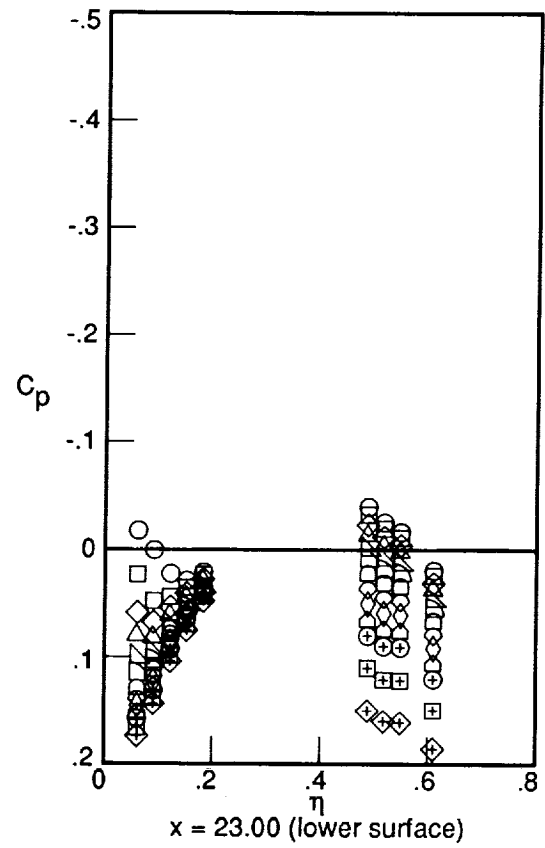
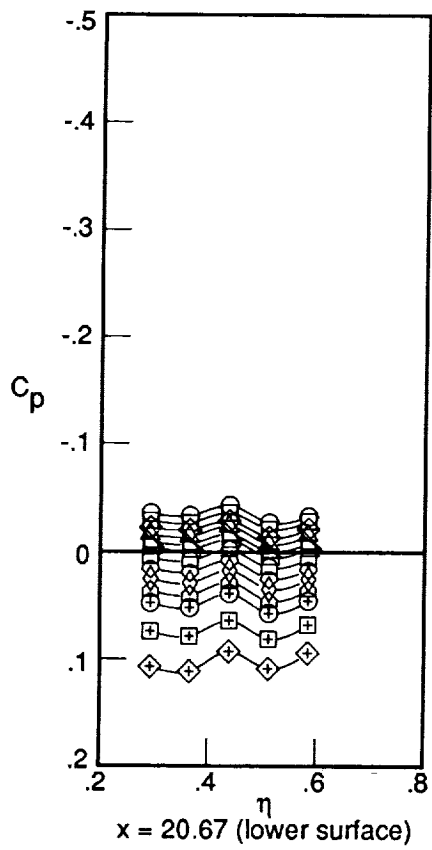
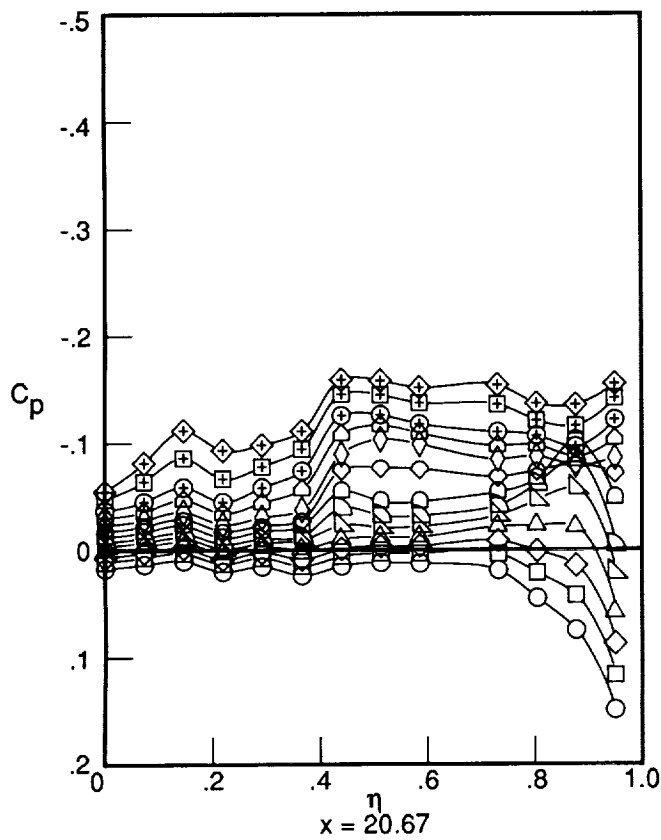
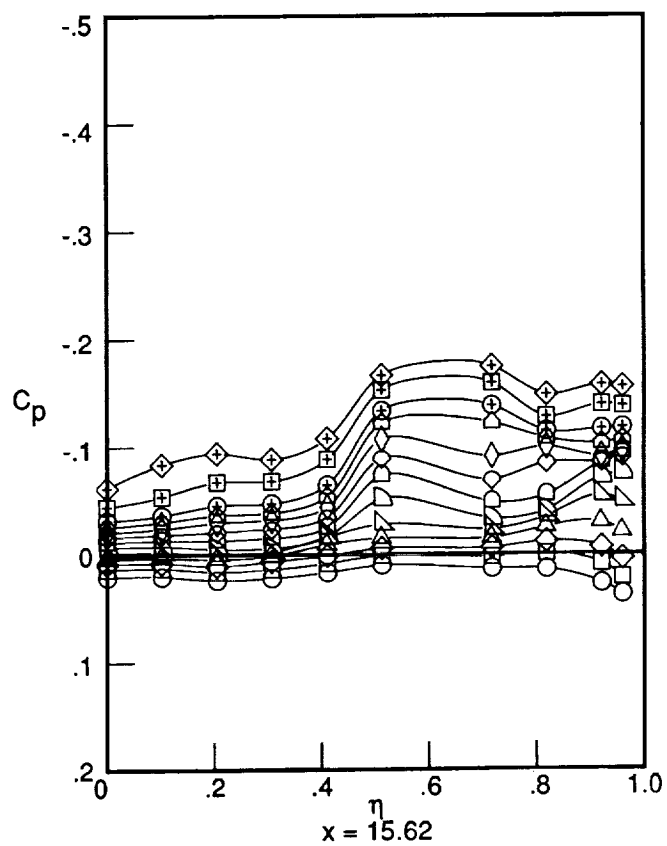
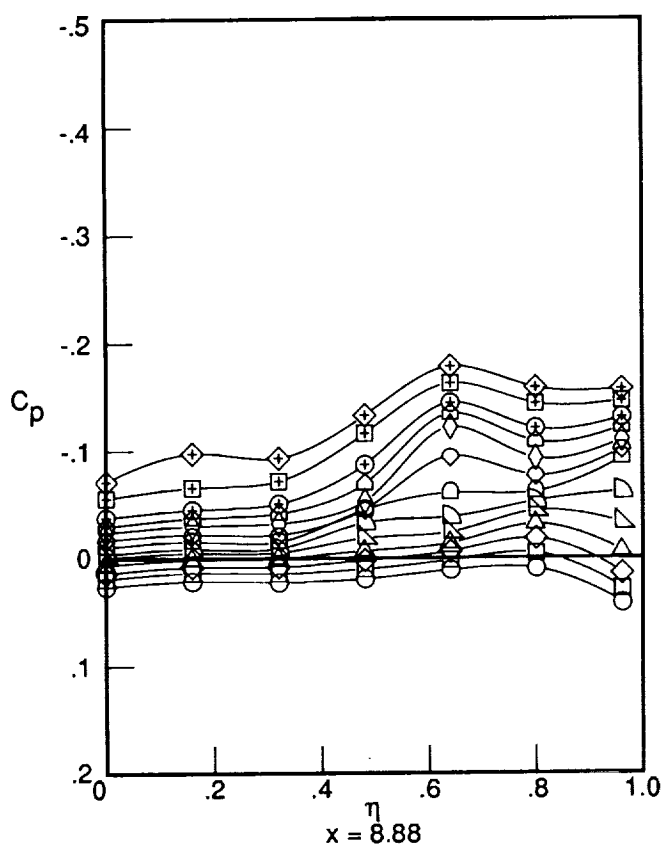


Figure D9. Concluded.



	α
○	-4.05
□	-2.96
◇	-2.03
△	-1.00
▵	.48
◐	.99
◑	2.01
◒	2.97
◓	3.98
◔	5.00
⊕	6.01
⊞	7.96
⊠	9.96

Figure D10. Surface pressure distributions. Mach 2.4; nacelles on.

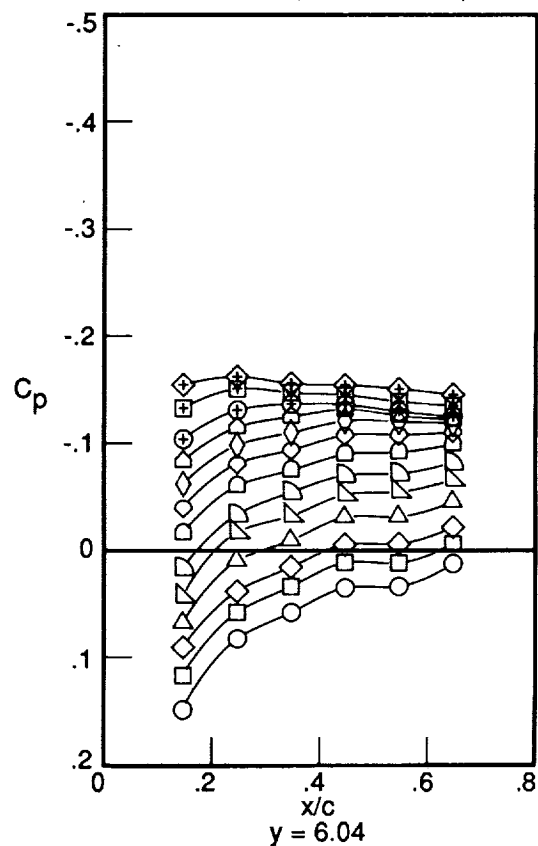
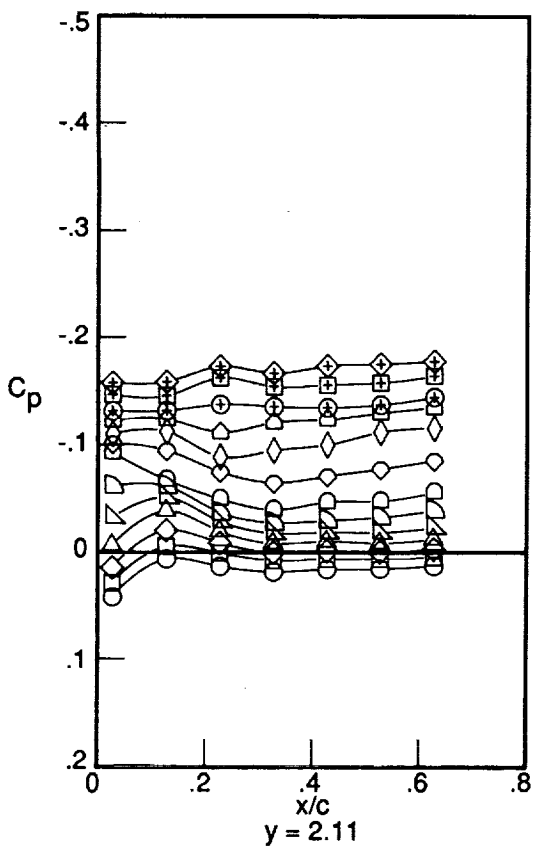
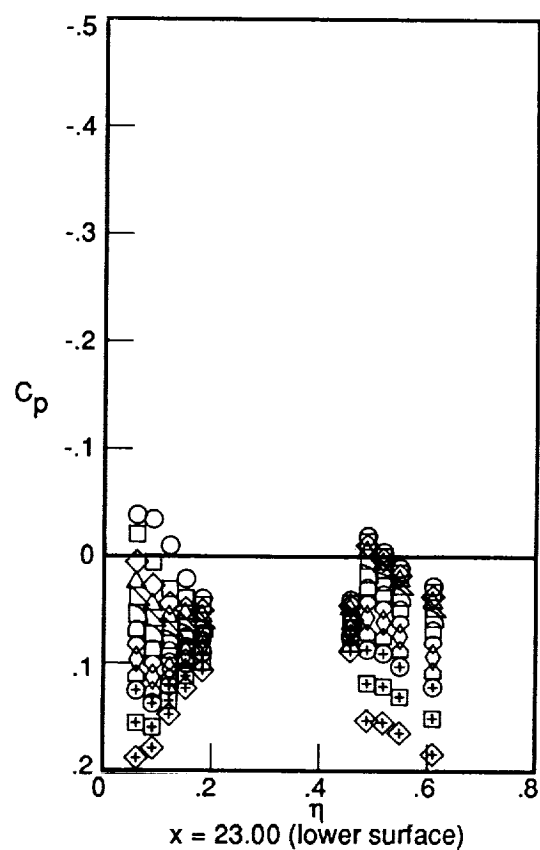
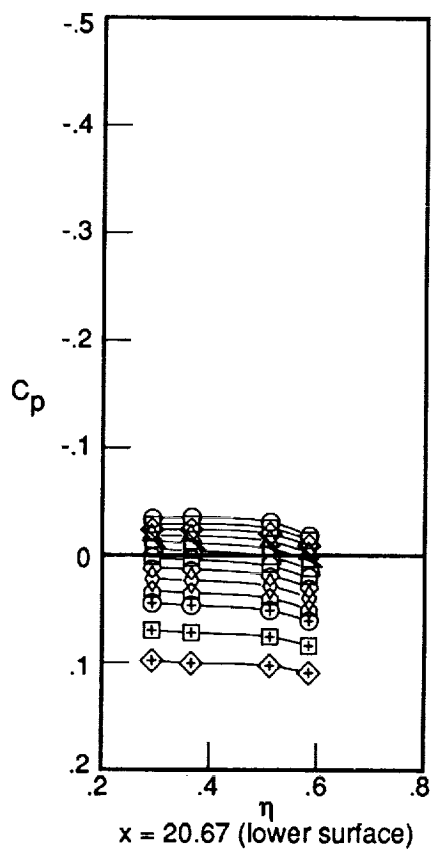


Figure D10. Concluded.

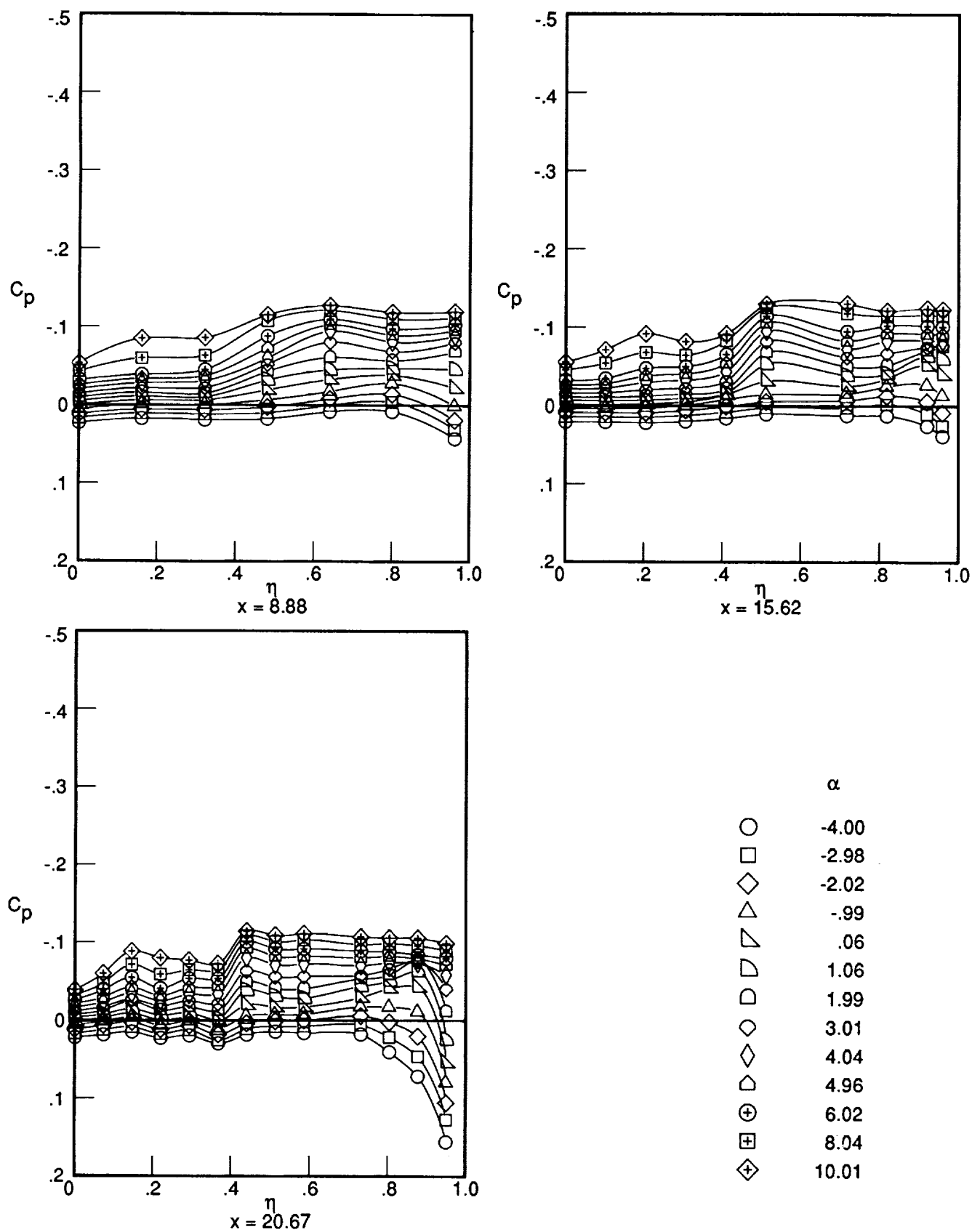


Figure D11. Surface pressure distributions. Mach 2.8; nacelles on.

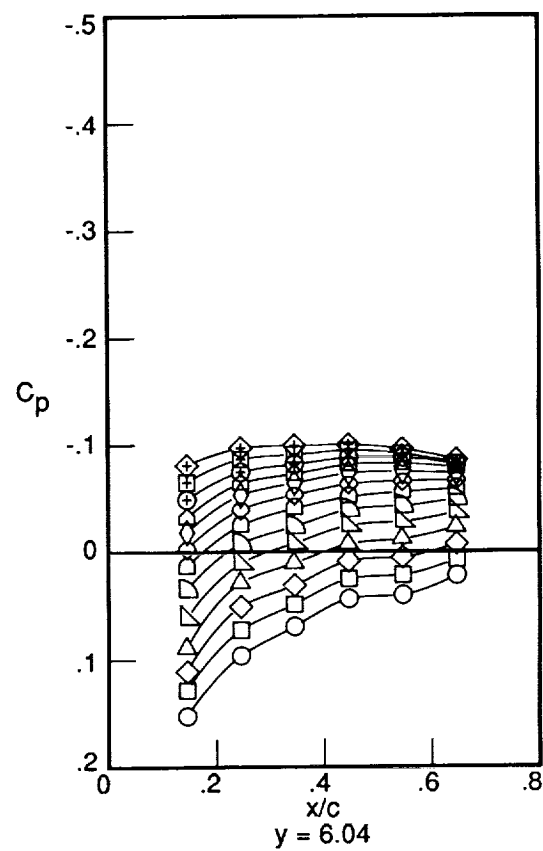
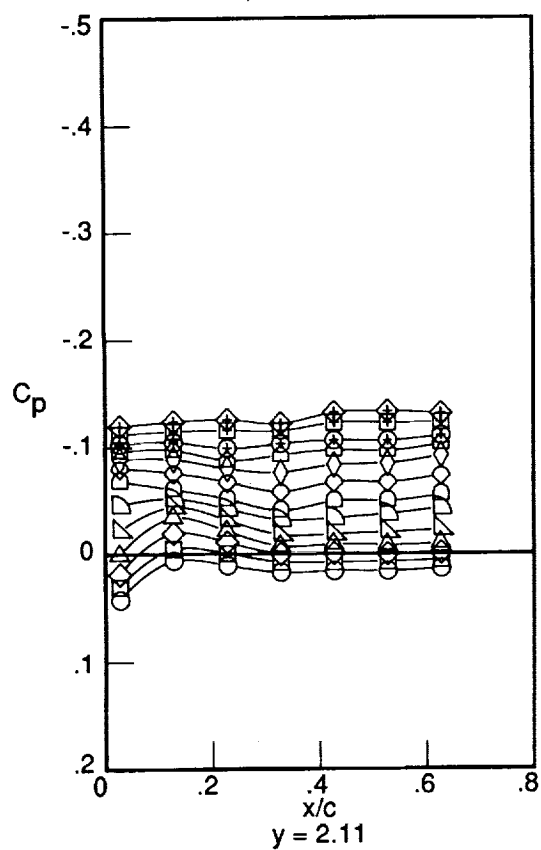
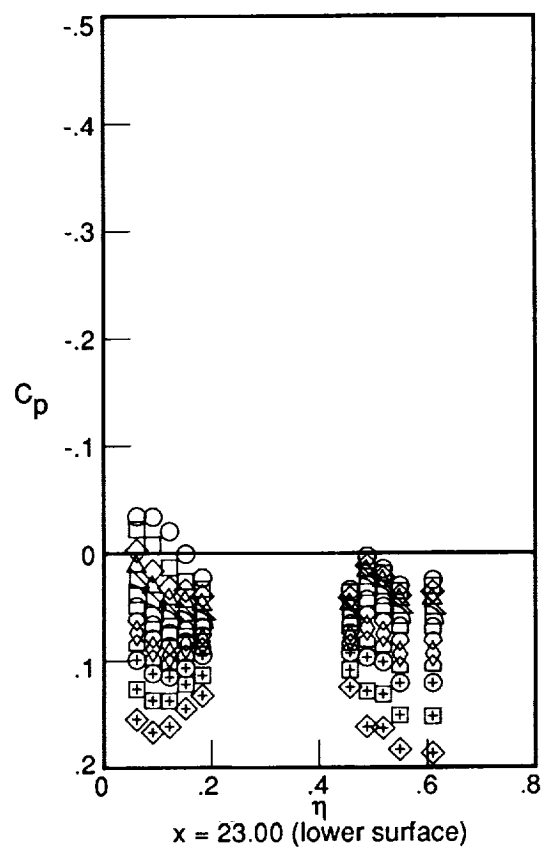
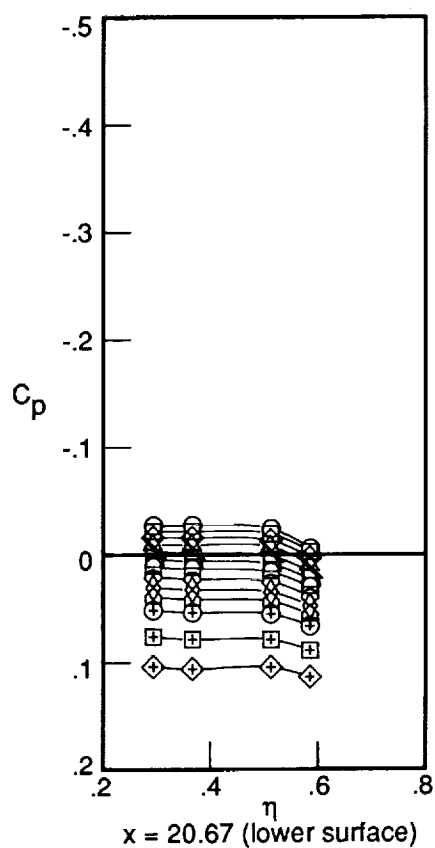
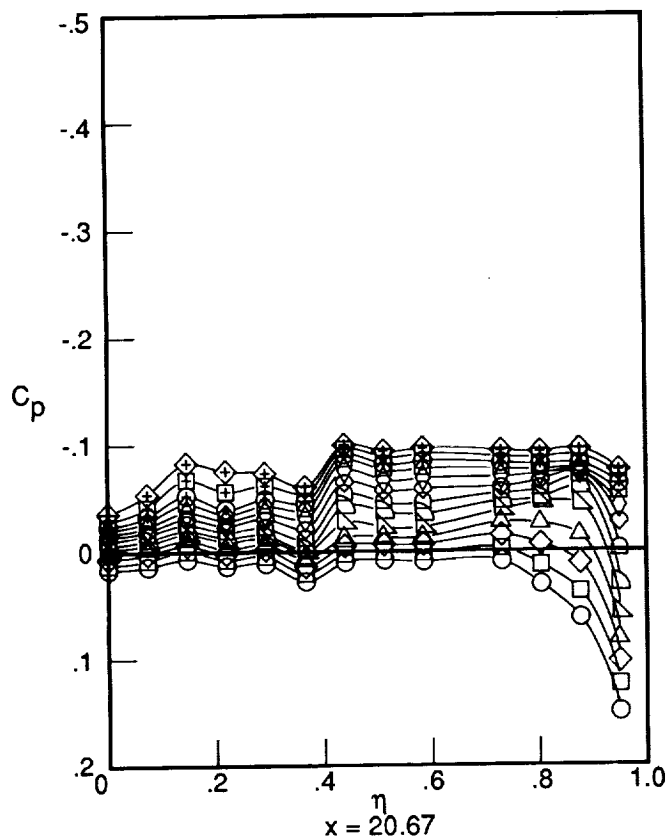
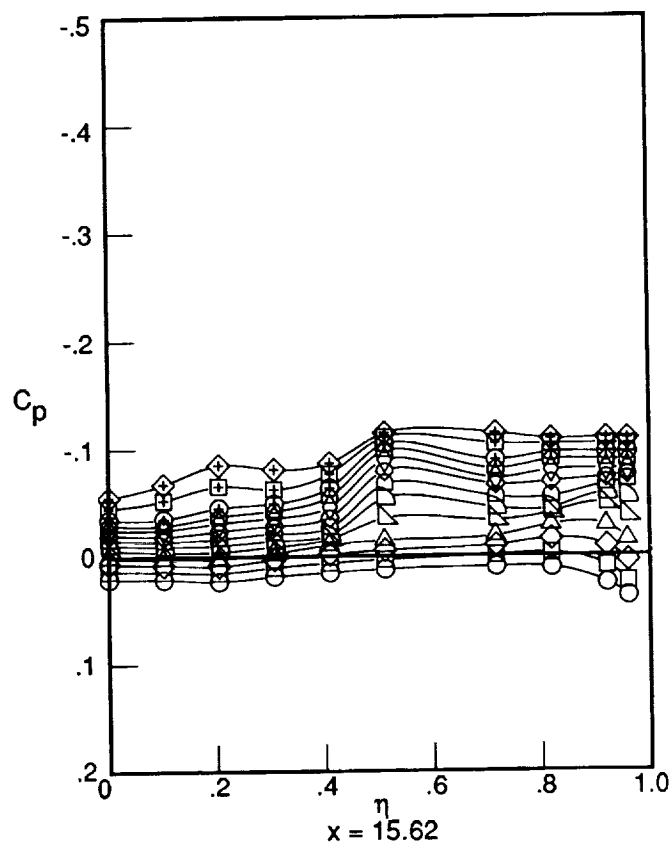
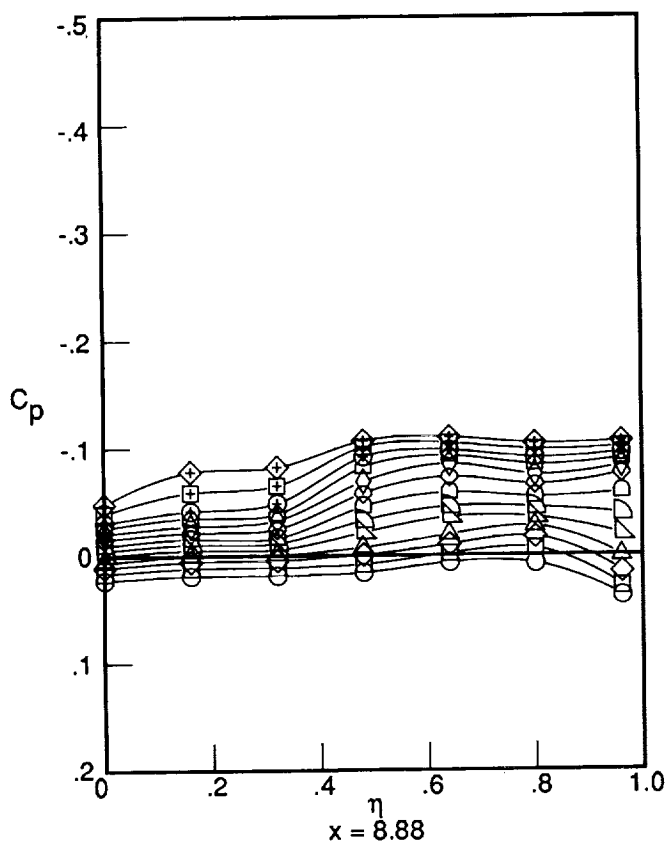


Figure D11. Concluded.



	α
○	-4.00
□	-2.98
◇	-1.96
△	-1.03
▽	.03
◐	1.01
◑	1.97
◒	2.99
◓	3.98
◔	4.99
⊕	5.94
⊞	8.07
⊠	10.00

Figure D12. Surface pressure distributions. Mach 3.0; nacelles on.

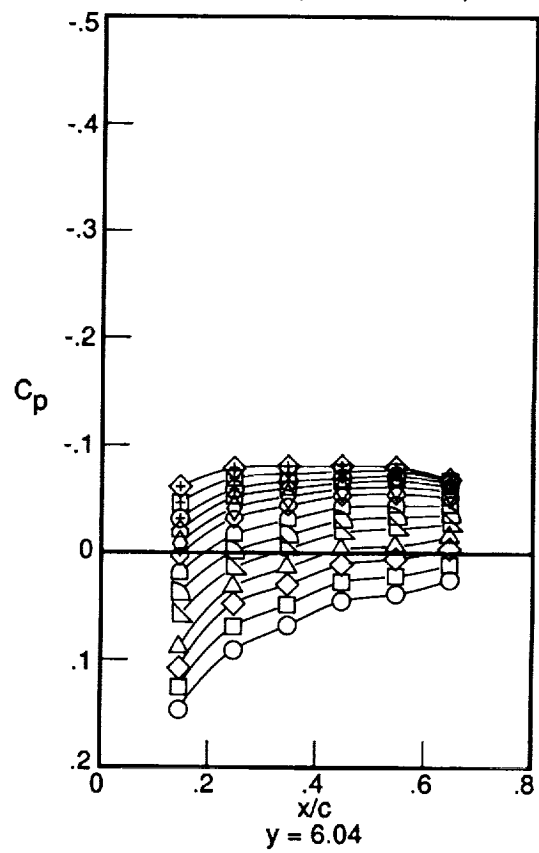
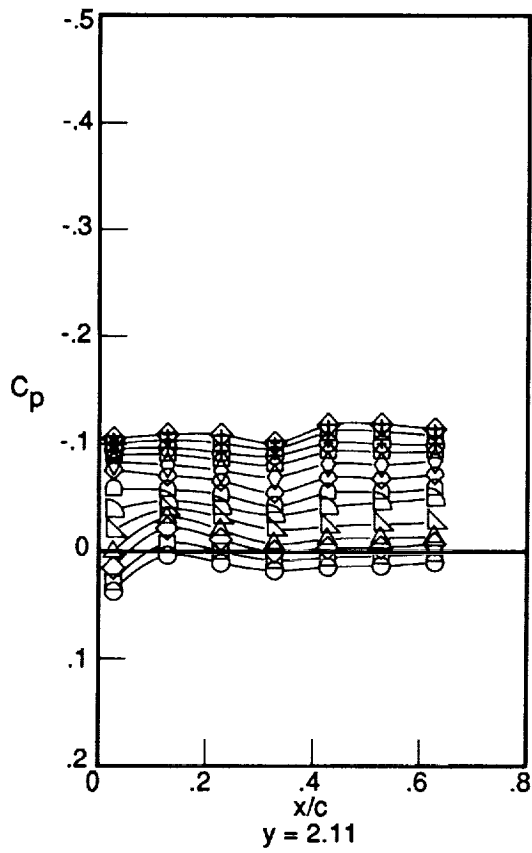
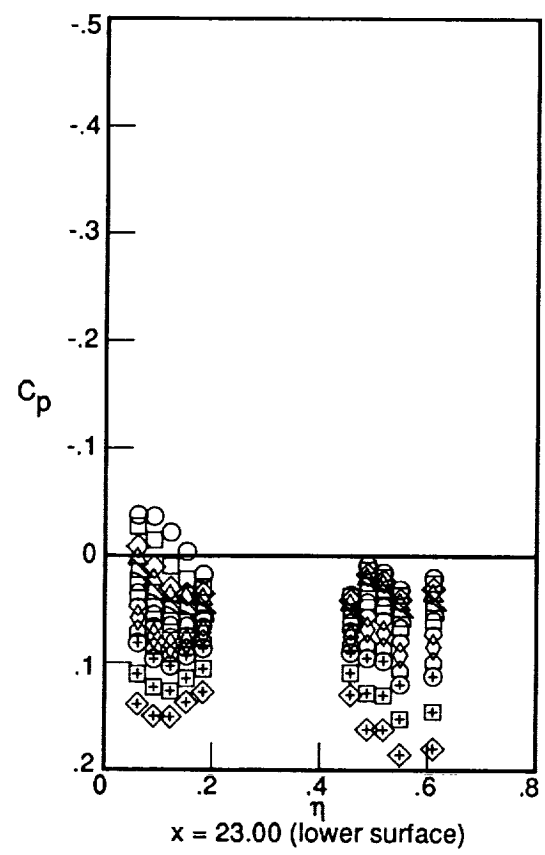
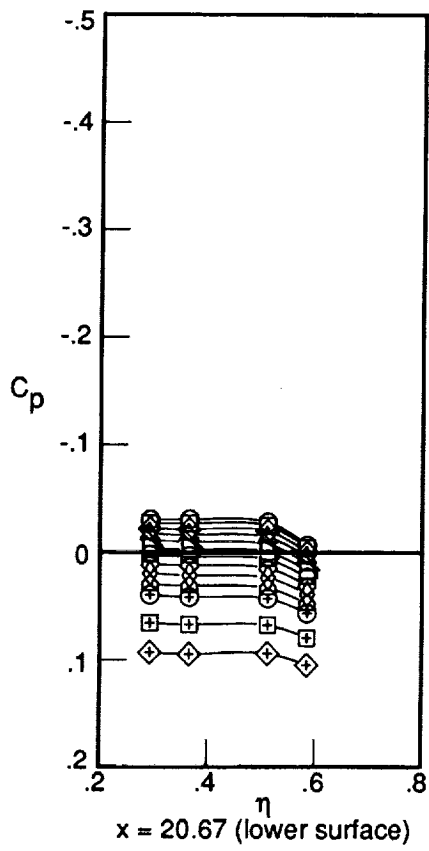
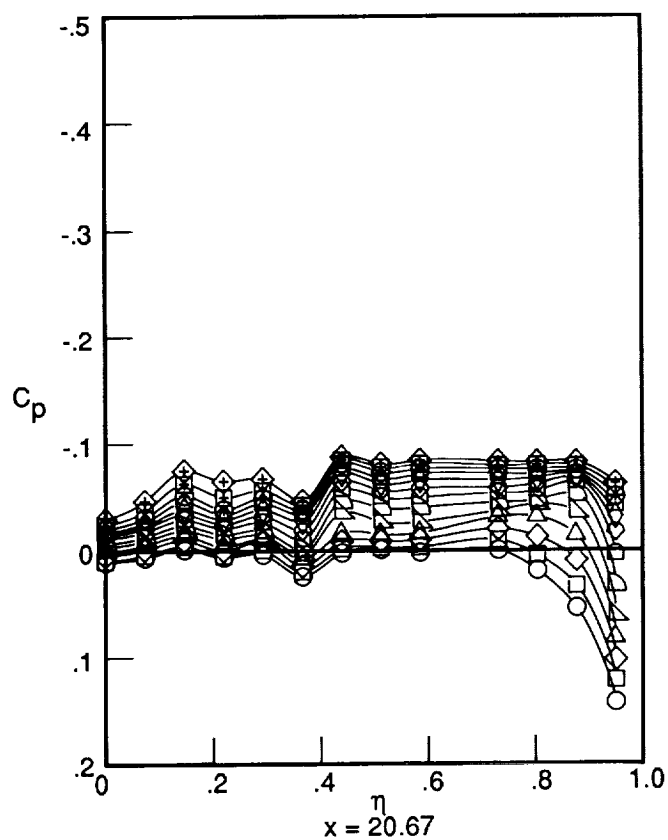
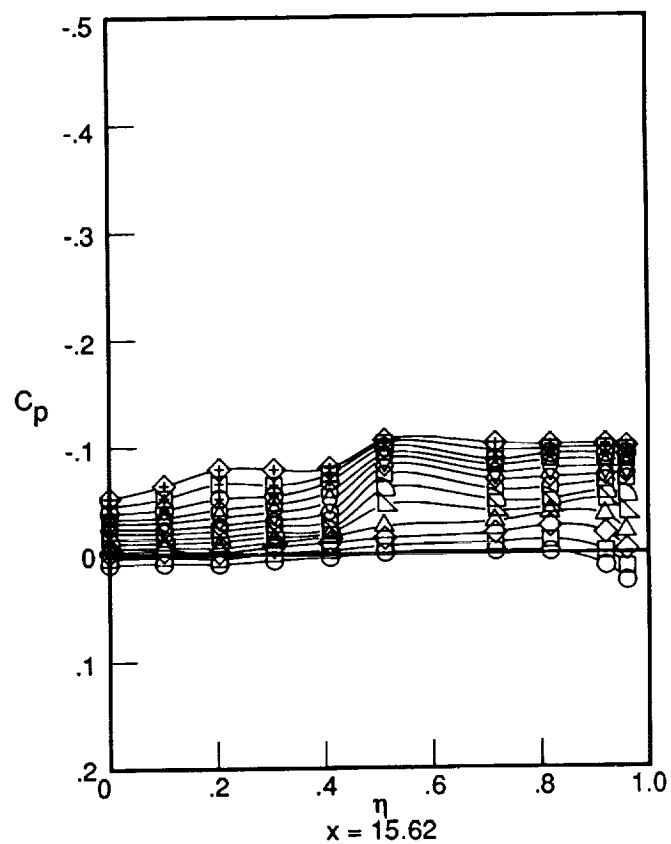
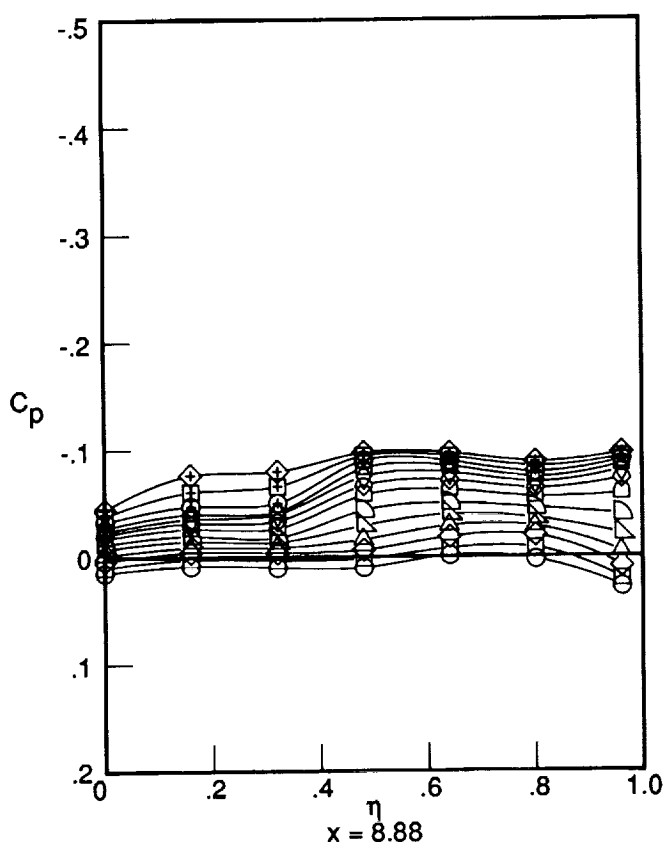


Figure D12. Concluded.



	α
○	-4.00
□	-3.01
◇	-2.03
△	-1.00
▽	0.00
◐	1.00
◑	2.01
◒	2.99
◓	4.06
◔	4.97
⊕	6.04
⊞	7.98
⊠	10.01

Figure D13. Surface pressure distributions. Mach 3.2; nacelles on.

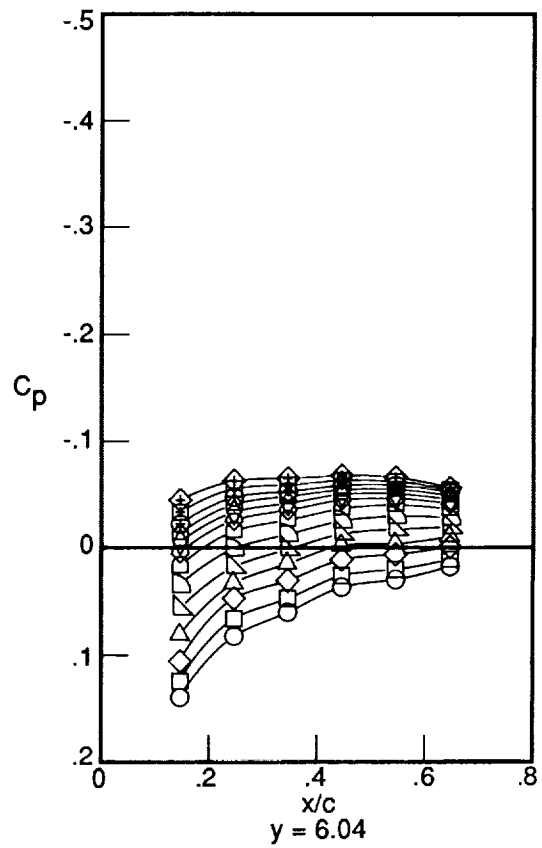
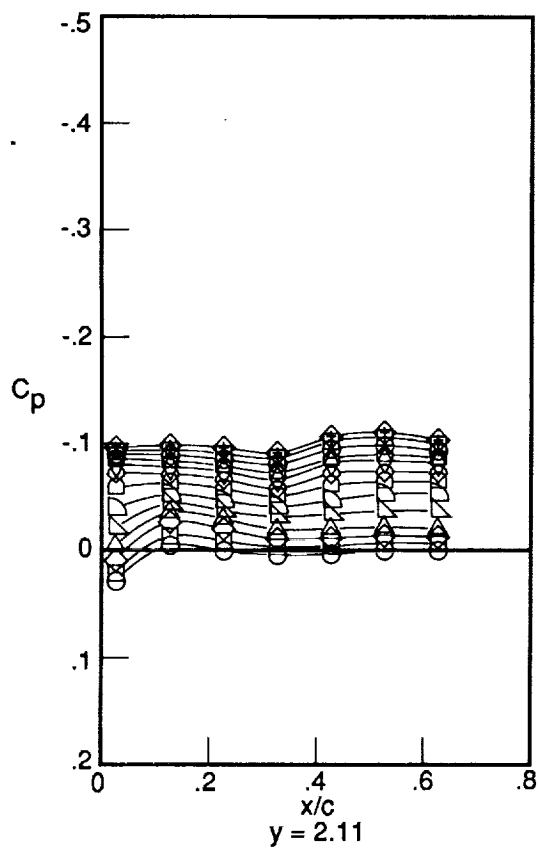
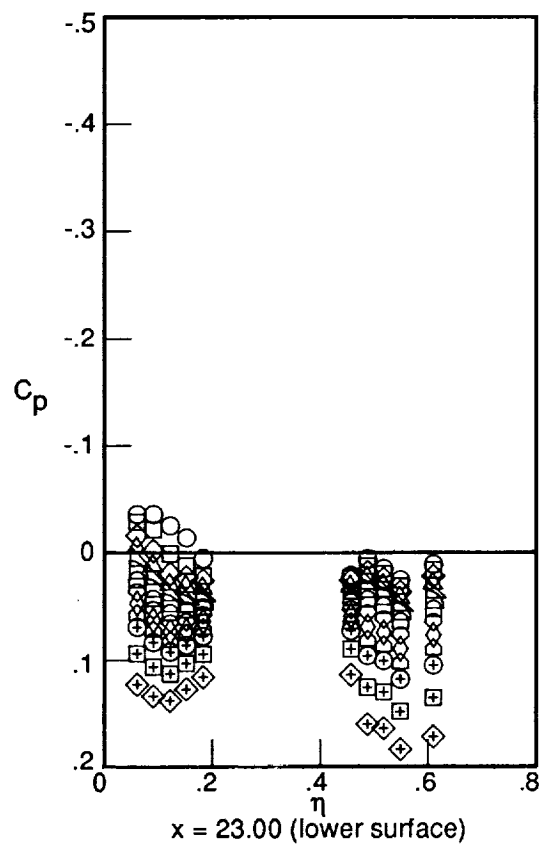
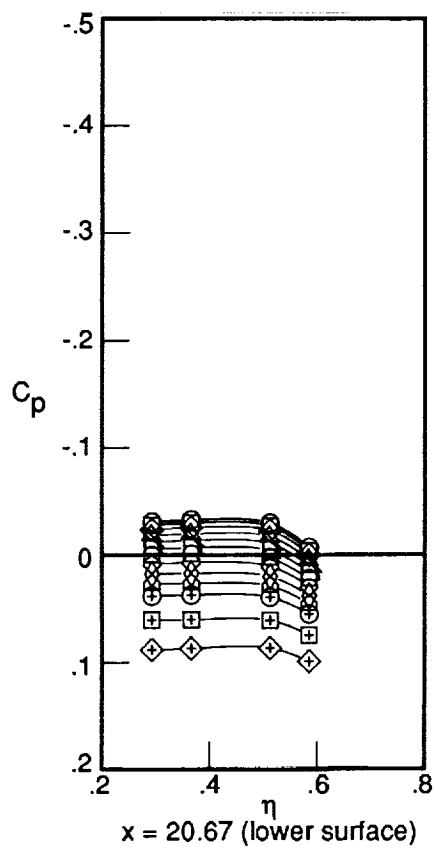
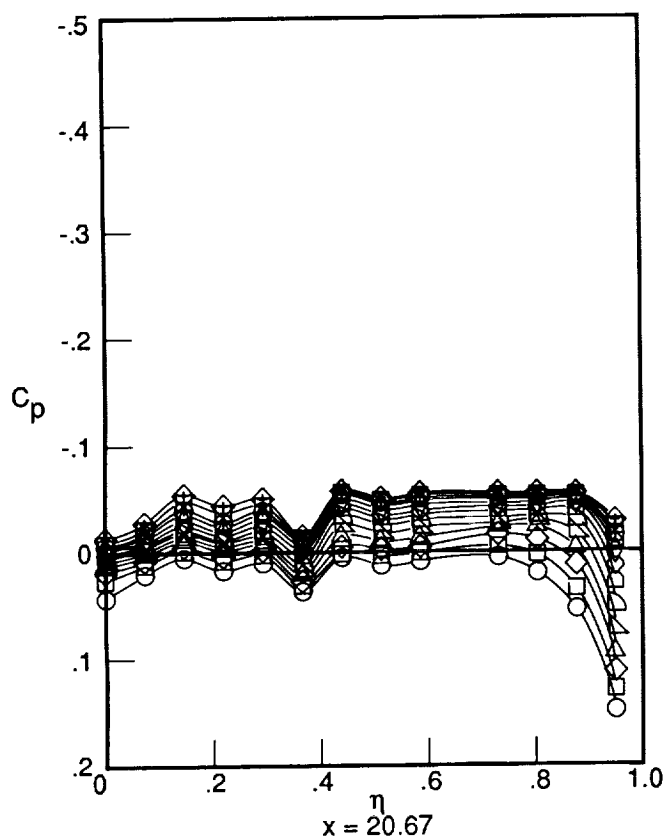
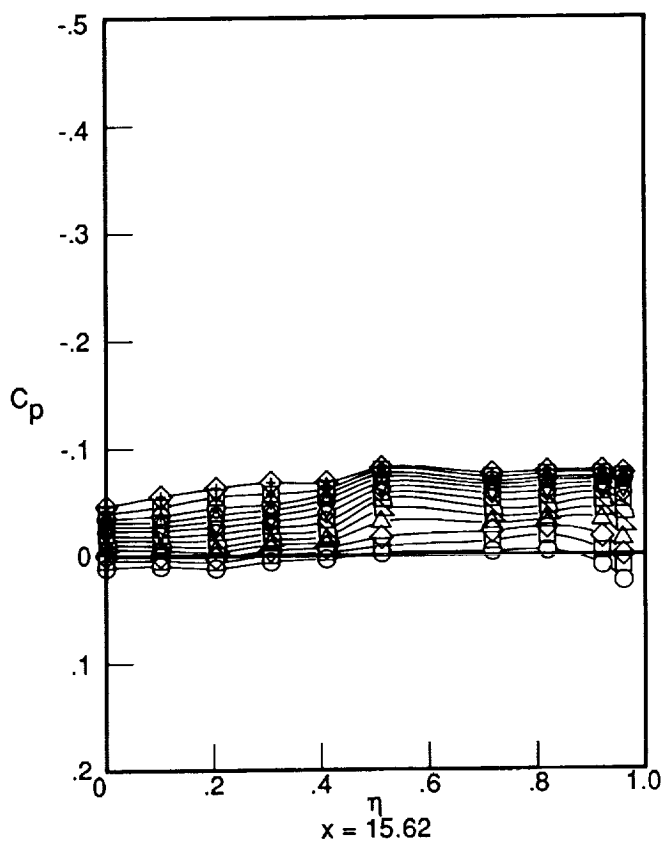
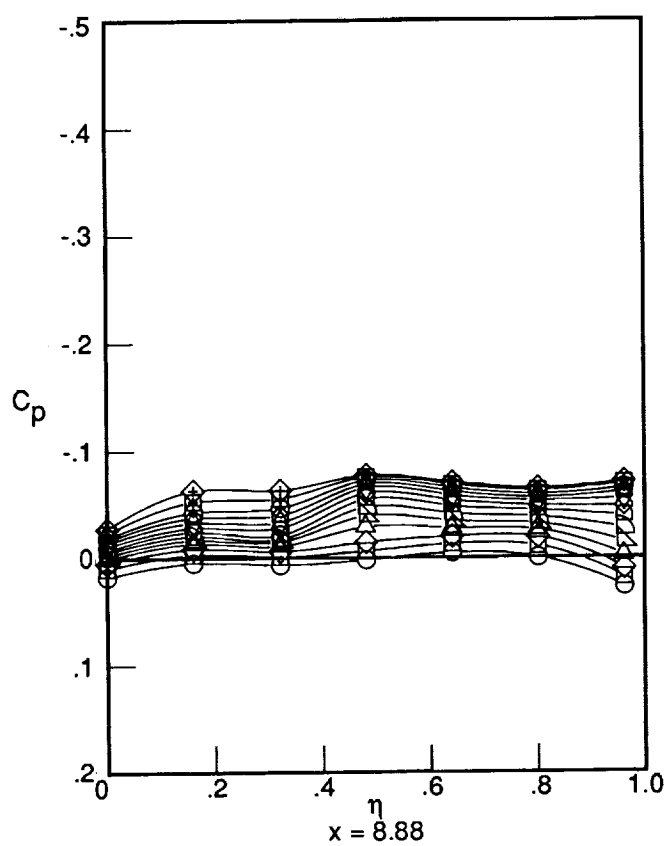


Figure D13. Concluded.



α	
-4.02	○
-2.98	□
-2.03	◇
-.98	△
.05	▽
1.01	◐
2.04	◑
3.03	◊
4.04	◈
4.99	◉
6.04	⊕
7.98	⊞
10.03	⊠

Figure D14. Surface pressure distributions. Mach 3.6; nacelles on.

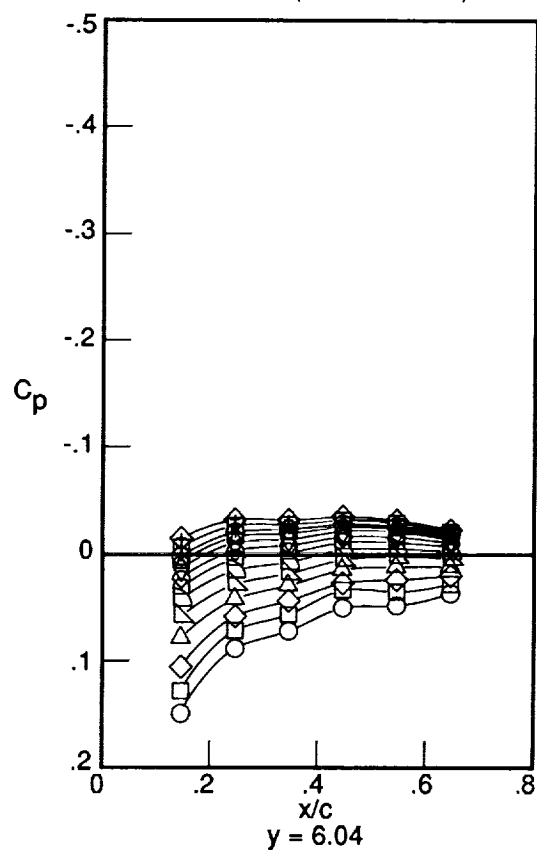
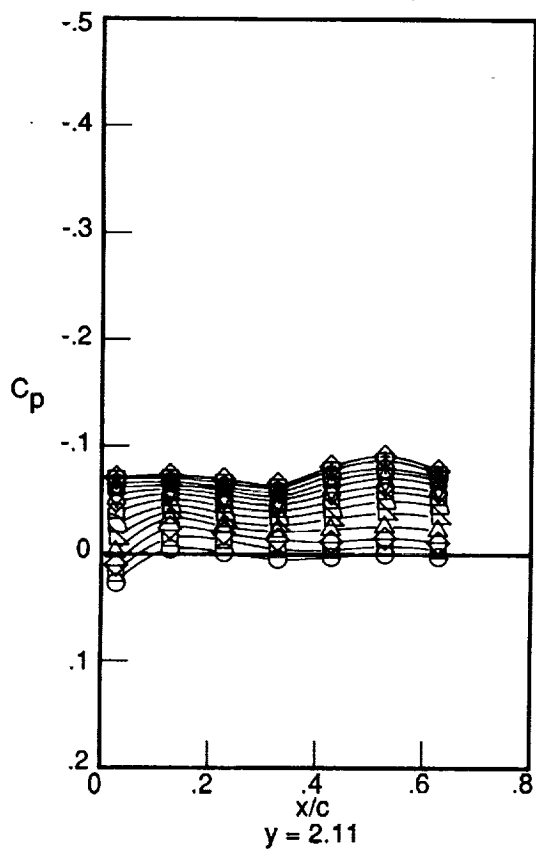
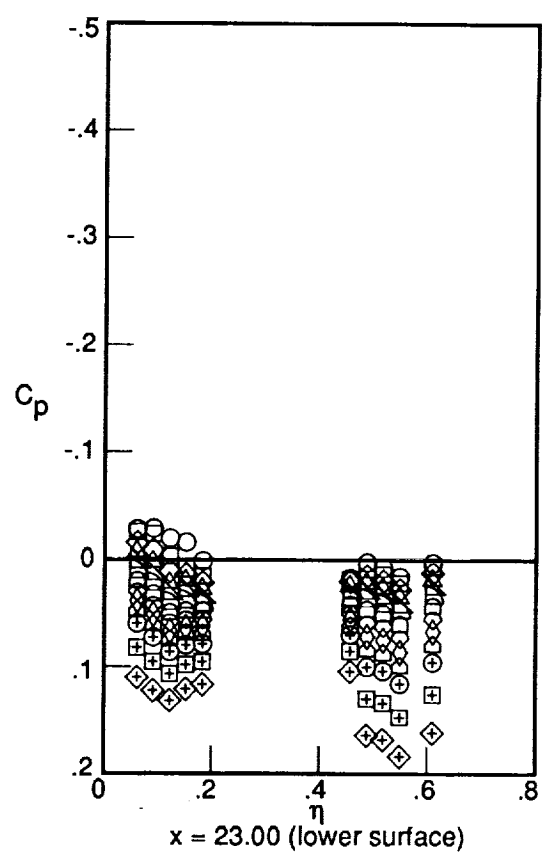
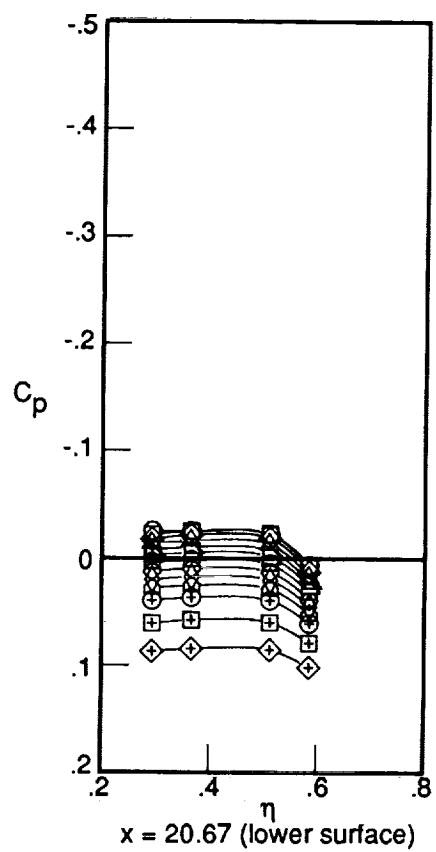


Figure D14. Concluded.

Appendix E

Tabulated Surface Pressures

The surface pressures are tabulated in the microfiche supplement for the following conditions —

$M = 1.6, 2.0, 2.4, 2.8, 3.0, 3.2,$ and 3.6

$\alpha = -4^\circ$ – 10°

$x = 8.88, 15.62, 20.67, 20.67$ (lower surface), and 23.00

$y = 2.11$ and 6.04

With and without nacelles

References

1. Driver, C.; Robins, A. W.; and Spearman, M. L.: *Aerodynamic Characteristics at Mach Numbers of 2.30, 2.96, and 3.50 of a Supersonic Transport Model With a Blended Wing-Body, Variable-Sweep Auxiliary Wing Panels, and Outboard Tail Surfaces*. NASA TM X-803, 1963.
2. Robins, A. Warner; Spearman, M. Leroy; and Harris, Roy V., Jr.: *Aerodynamic Characteristics at Mach Numbers of 2.30, 2.60, and 2.96 of a Supersonic Transport Model With a Blended Wing-Body, Variable-Sweep Auxiliary Wing Panels, Outboard Tail Surfaces, and a Design Mach Number of 2.6*. NASA TM X-815, 1963.
3. Morris, Odell A.; and Fuller, Dennis E.: *Aerodynamic Characteristics of a Three-Engine Supersonic Transport Model Having a Low-Aspect-Ratio Variable-Sweep Warped Wing*. NASA TM X-1011, 1964.
4. Morris, Odell A.; and Fournier, Roger H.: *Aerodynamic Characteristics at Mach Numbers 2.30, 2.60, and 2.96 of a Supersonic Transport Model Having a Fixed, Warped Wing*. NASA TM X-1115, 1965.
5. Hoffman, Sherwood: *Bibliography of Supersonic Cruise Aircraft Research (SCAR) Program From 1972 to Mid-1977*. NASA RP-1003, 1977.
6. Hoffman, Sherwood: *Bibliography of Supersonic Cruise Research (SCR) Program From 1977 to Mid-1980*. NASA RP-1063, 1980.
7. *National Aeronautical R & D Goals—Agenda for Achievement*. Executive Off. of the President, Off. of Science and Technology Policy, Feb. 1987.
8. Robins, A. Warner; Dollyhigh, Samuel M.; Beissner, Fred L., Jr.; Geiselhart, Karl; Martin, Glenn L.; Shields, E. W.; Swanson, E. E.; Coen, Peter G.; and Morris, Shelby J., Jr.: *Concept Development of a Mach 3.0 High-Speed Civil Transport*. NASA TM-4058, 1988.
9. Van Dam, C. P.: Swept Wing-Tip Shapes for Low-Speed Airplanes. *SAE Trans.*, Section 6, vol. 94, 1985, pp. 6.355-6.364.
10. Van Dam, C. P.: Induced-Drag Characteristics of Crescent-Moon-Shaped Wings. *J. Aircr.*, vol. 24, no. 2, Feb. 1987, pp. 115-119.
11. Naik, D. A.; and Ostowari, C.: An Experimental Study of the Aerodynamic Characteristics of Planar and Non-Planar Outboard Wing Planforms. AIAA-87-0588, Jan. 1987.
12. Belton, Pamela S.; and Campbell, Richard L.: *Experimental Study of a Generic High-Speed Civil Transport*. NASA TM-4382, 1992.
13. Jackson, Charlie M., Jr.; Corlett, William A.; and Monta, William J.: *Description and Calibration of the Langley Unitary Plan Wind Tunnel*. NASA TP-1905, 1981.
14. Braslow, Albert L.; Hicks, Raymond M.; and Harris, Roy V., Jr.: *Use of Grit-Type Boundary-Layer-Transition Trips on Wind-Tunnel Models*. NASA TN D-3579, 1966.
15. Stallings, Robert L., Jr.; and Lamb, Milton: *Effects of Roughness Size on the Position of Boundary-Layer Transition and on the Aerodynamic Characteristics of a 55° Swept Delta Wing at Supersonic Speeds*. NASA TP-1027, 1977.
16. Wassum, Donald L.; and Hyman, Curtis E., Jr.: *Procedures and Requirements for Testing in the Langley Research Center Unitary Plan Wind Tunnel*. NASA TM-100529, 1988.
17. Sommer, Simon C.; and Short, Barbara J.: *Free-Flight Measurements of Turbulent-Boundary-Layer Skin Friction in the Presence of Severe Aerodynamic Heating at Mach Numbers From 2.8 to 7.0*. NACA TN 3391, 1955.
18. Shrout, Barrett L.; and Talcott, Noel A., Jr.: *Effects of Wing Sweep and Camber on Aerodynamic Characteristics of a Fighter Configuration at Supersonic Speeds*. NASA TM-86427, 1985.
19. Middleton, W. D.; and Lundry, J. L.: *A System for Aerodynamic Design and Analysis of Supersonic Aircraft. Part 1—General Description and Theoretical Development*. NASA CR-3351, 1980.
20. Siclari, M. J.; and Del Guidice, P.: A Hybrid Finite Volume Approach to Euler Solutions for Supersonic Flows. AIAA-88-0225, Jan. 1988.
21. Vatsa, Veer N.; Turkel, Eli; and Abolhassani, J. S.: *Extension of Multigrid Methodology to Supersonic/Hypersonic 3-D Viscous Flows*. NASA CR-187612, ICASE Rep. No. 91-66, 1991.
22. Pittman, James L.; Bonhaus, Daryl L.; Siclari, Michael J.; and Dollyhigh, Samuel M.: Euler Analysis of a High-Speed Civil Transport Concept at Mach 3. *J. Aircr.*, vol. 28, no. 4, Apr. 1991, pp. 239-245.
23. Covell, Peter F.; Hernandez, Gloria; Flamm, Jeffrey D.; and Rose, Ollie J.: Supersonic Aerodynamic Characteristics of a Mach 3 High-Speed Civil Transport Configuration. AIAA-90-3210, Sept. 1990.
24. Dollyhigh, Samuel M.: *Theoretical Evaluation of High-Speed Aerodynamics for Arrow-Wing Configurations*. NASA TP-1358, 1979.
25. Harris, Roy V., Jr.: *An Analysis and Correlation of Aircraft Wave Drag*. NASA TM X-947, 1964.
26. Carlson, Harry W.; and Darden, Christine M.: *Validation of a Pair of Computer Codes for Estimation and Optimization of Subsonic Aerodynamic Performance of Simple Hinged-Flap Systems for Thin Swept Wings*. NASA TP-2828, 1988.
27. Carlson, Harry W.; and Mann, Michael J.: *Survey and Analysis of Research on Supersonic Drag-Due-to-Lift Minimization With Recommendations for Wing Design*. NASA TP-3202, 1992.
28. Holman, J. P.: *Experimental Methods for Engineers*, Third ed. McGraw-Hill Book Co., c.1978.

REPORT DOCUMENTATION PAGE			Form Approved OMB No. 0704-0188	
Public reporting burden for this collection of information is estimated to average 1 hour per response, including the time for reviewing instructions, searching existing data sources, gathering and maintaining the data needed, and completing and reviewing the collection of information. Send comments regarding this burden estimate or any other aspect of this collection of information, including suggestions for reducing this burden, to Washington Headquarters Services, Directorate for Information Operations and Reports, 1215 Jefferson Davis Highway, Suite 1204, Arlington, VA 22202-4302, and to the Office of Management and Budget, Paperwork Reduction Project (0704-0188), Washington, DC 20503.				
1. AGENCY USE ONLY(Leave blank)	2. REPORT DATE November 1993	3. REPORT TYPE AND DATES COVERED Technical Paper		
4. TITLE AND SUBTITLE An Experimental Investigation of a Mach 3.0 High-Speed Civil Transport at Supersonic Speeds		5. FUNDING NUMBERS WU 505-59-20-01		
6. AUTHOR(S) Gloria Hernandez, Peter F. Covell, and Marvin E. McGraw, Jr.				
7. PERFORMING ORGANIZATION NAME(S) AND ADDRESS(ES) NASA Langley Research Center Hampton, VA 23681-0001		8. PERFORMING ORGANIZATION REPORT NUMBER L-17171		
9. SPONSORING/MONITORING AGENCY NAME(S) AND ADDRESS(ES) National Aeronautics and Space Administration Washington, DC 20546-0001		10. SPONSORING/MONITORING AGENCY REPORT NUMBER NASA TP-3365		
11. SUPPLEMENTARY NOTES Hernandez and Covell: Langley Research Center, Hampton, VA; McGraw: Lockheed Engineering & Sciences Company, Hampton, VA.				
12a. DISTRIBUTION/AVAILABILITY STATEMENT Unclassified -Unlimited Subject Category 02		12b. DISTRIBUTION CODE		
13. ABSTRACT (Maximum 200 words) An experimental study has been conducted to determine the aerodynamic characteristics of a proposed high-speed civil transport. This configuration was designed to cruise at Mach 3.0 and sized to carry 250 passengers for 6500 n.mi. The configuration consists of a highly blended wing body and features a blunt parabolic nose planform, a highly swept inboard wing panel, a moderately swept outboard wing panel, and a curved wingtip. Wind tunnel tests were conducted in the Langley Unitary Plan Wind Tunnel on a 0.0098-scale model. Force, moment, and pressure data were obtained for Mach numbers ranging from 1.6 to 3.6 and at angles of attack ranging from -4° to 10°. Extensive flow visualization studies (vapor screen and oil flow) were obtained in the experimental program. Both linear and advanced computational fluid dynamics (CFD) theoretical comparisons are shown to assess the ability to predict forces, moments, and pressures on configurations of this type. In addition, an extrapolation of the wind tunnel data, based on empirical principles, to full-scale conditions is compared with the theoretical aerodynamic predictions.				
14. SUBJECT TERMS High-speed civil transport; Supersonic aerodynamics; Longitudinal aerodynamic characteristics; Surface pressures; Nacelle effects; Linear theory			15. NUMBER OF PAGES 93	
			16. PRICE CODE A05	
17. SECURITY CLASSIFICATION OF REPORT Unclassified	18. SECURITY CLASSIFICATION OF THIS PAGE Unclassified	19. SECURITY CLASSIFICATION OF ABSTRACT	20. LIMITATION OF ABSTRACT	